11-11-2017

Nanopatterns of Zinc Phthalocyanines, Gold Nanoparticles, and Porphyrins Prepared Using Particle Lithography: Characterization of Patterning Steps with Scanning Probe Microscopy

Ashley Marie Taylor
Louisiana State University and Agricultural and Mechanical College, atayl93@lsu.edu

NANOPATTERNS OF ZINC PHTHALOCYANINES, GOLD NANOPARTICLES, AND PORPHYRINS PREPARED USING PARTICLE LITHOGRAPHY: CHARACTERIZATION OF PATTERNING STEPS WITH SCANNING PROBE MICROSCOPY

A Dissertation

Submitted to the Graduate Faculty of the
Louisiana State University and
Agricultural and Mechanical College
in partial fulfillment of the
requirement for the degree of
Doctor of Philosophy

in

The Department of Chemistry

by
Ashley Marie Taylor
M.S., Louisiana State University, 2015
B.S., Winston-Salem State University, 2012
December 2017

This dissertation is dedicated to my mother, father, brother, and Michael.

Thank you for allowing me to leave New Jersey!

God has kept me covered while I have been on this adventure.

I love all of you!

ACKNOWLEDGEMENTS

I would like to express my gratitude to my advisor, Professor Jayne C. Garno, for accepting me into her group during a time when I was trying to determine my next steps in my career and believing in my research goals. I have been fortunate to have an advisor that has allowed me to critically think about my research interests within the field of nanoscience. I also want to thank my committee members Professor Kermit Murray, Professor Revati Kumar, and Professor Carol Lammi-Keefe for reviewing my dissertation and providing valuable feedback. I want to thank Professor Sayo O. Fakayode, Mr. Clifton Bell, Professor Isiah M. Warner, Dr. Gloria Thomas, and Dr. Zakiya Wilson-Kennedy for their continuous love and support during my undergraduate and graduate careers. Dr. Fakay, if you never took me under your wing, I am not sure if this would have been a reality for me in STEM. You believed in me the very first day you asked, "Why don't you come visit my lab?" You never let me give up no matter how many things were against me. Mr. Bell has always been an advocate for me! He always made sure I was networking, developing myself, and mentoring on life. I cannot thank you enough. I am appreciative of both past and present members of the Garno research group for all of the discussions and good times we have had. Lastly, and most importantly, I want to express my deepest appreciation to my parents (Maxwell Anthony Taylor and Natalie Diaz-Taylor), my brother (Maxwell Cory Taylor), and soon to be husband (Michael Nequan Jackson) for all of their moral support, advice, love and encouragement. Michael has been there by my side throughout the whole journey. If I could give him an honorary doctorate it would be well deserving. This is for all of the late nights we had in the lab, late nights at home studying, him listening to me practice my presentations and actually asking me questions. I definitely could not have made it to this point without you Mr. Jackson.

TABLE OF CONTENTS

LIST OF FIGURES

LIST OF ABBREVIATIONS

AC	Alternating Current
AFM	Atomic Force Microscopy
APTES	3-Aminopropyltriethoxysilane
CP-AFM	Conductive Prove Atomic Force Microscopy
DC	Direct Current
DPN	Dip-Pen Nanolithography
LSPR	Localized Surface Plasmon Resonance
MPTMS	3-mercaptopropyl-trimethoxysilane
MSM	Magnetic Sample Modulation
OTS	Octadecyltrichlorosilane
OTMS	Octadecyltrimethoxysilane
PEG	2-[methoxy(polyethyleneoxy)propyl] trichlorosilane
SAMs	Self assembled monolayers
SERS	Surface-Enhanced Raman Scattering
SPL	Scanning Probe Lithography
SPM	Scanning Probe Microscopy
STM	Scanning Tunneling Microscopy
TPP	5,10,15,20-tetraphenyl-21*H*,23*H*-porphyrin
TPN	5,10,15,20-tetraphenyl-21H,23H-porphine nickle(II)
UHV	Ultra-High Vacuum
ZnPc	Zinc Phthalocyanine

ABSTRACT

The growth and self-assembly of molecules on surfaces can be directly visualized at the molecular level using studies which combine nanoscale lithography and high-resolution imaging. Nanopatterning provides a unique and practical approach for direct views of surface changes after the key chemical steps of nanopatterning, providing landmarks and baselines for measuring growth in vertical and lateral dimensions. Controlling the arrangement of materials on surfaces at the nanoscale can be achieved using particle lithography. Arrays of well-defined nanostructures can be prepared with reproducible geometries and arrangement. Results for the preparation of nanopatterns produced with particle lithography are presented using high resolution images acquired with scanning probe microscopy (SPM). Samples were prepared using steps for depositing nanoparticles, porphyrins, and phthalocyanines on patterned surfaces to generate multicomponent nanopatterns. Studies of surface chemistry at the molecular level have practical applications for emerging technologies with photovoltaic and photoelectronic devices. Atomic force microscopy (AFM) was used to characterize samples to gain insight on the changes in surface chemistry after patterning organosilanes, organothiols and nanoparticles. For studies of surface chemistry at the nanoscale, AFM has unique capabilities for molecular visualization and ultrasensitive measurements of surface properties.

The history of SPM, instrument set-up, and results for particle lithography with porphyrins, zinc phthalocyanines and gold nanoparticles are described in this dissertation. Protocols for patterning porphyrin nanostructures on Au(111) were developed based on steps with immersion combined with particle lithography. Porphyrins with a central metal ion, 5,10,15,20-tetraphenyl-21H,23H-porphine (TPP) and free-base 5,10,15,20-tetraphenyl-21H,23H-porphine nickel(II) (TPN) were studied. Samples of zinc phthalocyanines were prepared using particle lithography

with surfaces that were patterned with organosilanes. The dimensions and spacing can be selectively tuned by using selected sizes of latex ad silica spheres as a surface mask. The metallated phthalocyanines bound selectively to the spatially confined sites of nanopatterns, and did not bind to areas of the organosilane resist. Bare gold nanoparticles and organosilane coated nanoparticles were synthesized for characterizations with AFM. At the nanoscale, variations in the sizes of patterns provide a surface test platform for evaluating size dependent physical properties.

CHAPTER 1. INTRODUCTION

Nanostructures have applications in sensors,[1-2,] catalysis,[3] molecular separation[4] and electronic devices.[5] In this dissertation, the investigations presented in this dissertation describe nanofabrication protocols based on particle lithography which has been developed for generating nanostructures of organosilanes to produce well-defined surface platforms of complex, multicomponent architectures. Using atomic force microscopy (AFM), characterizations were successfully accomplished for molecular-level studies of morphology, self-assembly processes, and the properties of designed nanostructures.

1.1 Patterning Surfaces at the Nanoscale with Particle Lithography

Particle lithography is a versatile, high throughput approach for fabrication that has been used to generate periodic arrays of organic thin films, proteins and nanomaterials on surfaces.[6-9] Particle lithography is used to pattern a substrate by placing a spherical mask of latex or silica beads to direct the deposition of inorganic and organic materials. Preparation of exquisitely small, regular nanostructures have been accomplished with a few basic chemistry steps. The samples reveal relatively few defects at the nanoscale and are highly reproducible for patterning over relatively large areas of tens of microns.[10] Particle lithography has been used for patterning metals,[11-12,] nanoparticles,[8,13-15] proteins,[16-18] polymers,[19-22] and self-assembled monolayers (SAMs).[23-27] By immersing substrates in dilute solutions of organosilanes, SAMs are formed through surface self-assembly.[28-29]

The capability of AFM for achieving nanoscale resolution enables characterization of material properties as well as fundamental investigations of chemical or biochemical reactions on surfaces at the nanoscale. Fundamental studies of surface reactions and material properties at the molecular-level can provide essential information for the development of new and advanced technologies in

fields such as materials engineering [30-31] and molecular electronics.[32-33] A comprehensive literature review of contemporary approaches with particle lithography applied for patterning SAMs is presented in Chapter 2. The background, history, and basic operating principles of AFM are summarized for the methods used for studies of nanostructures. The AFM modes that were used for the studies described below include contact mode, tapping-mode, and magnetic sample modulation.

1.2 Preparations of Porphyrin Nanostructures using Immersion Particle Lithography

The steps for binding porphyrins to sites exposed inside nanoholes fabricated within dodecanethiol on Au(111) were characterized *ex situ* using AFM. Experiments are described in Chapter 3 for the basic steps of the patterning process using immersion particle lithography, disclosing AFM images of the nanostructures of porphyrins. Arrays of nanoholes were prepared using particle lithography combined with immersion in solutions of dodecanethiol. Self-assembled monolayers (SAMs) provide advantages for selecting the chemistry of surfaces with desired carbon chain lengths and functional groups. Wettability, adhesion, and acidity can be controlled by choosing functional head groups. In our study, methyl-terminated SAMs such as dodecanethiol were chosen as a resist layer to direct the adsorption of porphyrins onto gold substrates. For potential applications in molecular electronics and photovoltaics, porphyrins have become a focus in engineering nanostructures on surfaces. Porphyrins can be synthesized with substituents and metal ions to tune electrical and photoelectrical properties. However, preparing nanostructures of porphyrins on surfaces can be challenging. Porphyrins tend to stack through π-π interactions and form columnar structures throughout the surface, rather than forming a continuous thin film. To accomplish immersion particle lithography with porphyrins, silica spheres were used as a surface mask to control the deposition of dodecanethiol to produce nanoholes. Selected porphyrins were introduced to selectively bind within nanoholes by a second immersion step in dilute solutions.

Scanning probe microscopy was used to characterize morphological and physical properties of nanomaterials deposited on surfaces. The nanopatterned surfaces exhibit millions of reproducible test structures arranged in a periodic array according to the dimensions and spacing of the surface masks. Spatial selectivity was accomplished for directing the attachment of zinc-coordinated porphyrins within exposed sites of gold inside nanoholes with exposed sites of the gold substrate The test structures are ideal for further characterizations of conductive surface properties at the molecular level.

1.3 Nanopatterns of Zinc Phthalocyanines Prepared using Particle Lithography: Characterization of Patterning Steps with Scanning Probe Microscopy[34]

Surface characterizations of the patterning steps for preparing nanostructures of zinc phthalocyanines are presented in Chapter 4, describing the basic steps of the particle lithography. It can be challenging to prepare durable films and nanostructures of phthalocyanines because the molecules tend to bind in a coplanar orientation through physisorption to the surface and can stack together through π-π interactions between adjacent macrocycles. Spatial selectivity was achieved for directing the attachment of Zn-Pc to the surface using a resist film of 2-methoxy(polyethyleneoxy)propyl]trichlorosilane (PEG-silane) or with octadecyltrimethoxysilane (OTMS). The molecule chosen as a linker was (3-aminopropyl)triethoxysilane (APTES) which presents an amine group at the interface. Patterned arrays of nanoholes and nanorings were prepared using particle lithography combined with steps of solution immersion and vapor deposition of organosilanes. Heterostructures of APTES and zinc phthalocyanines were constructed using nanopatterns as sites for binding. Samples prepared with particle lithography exhibit millions of reproducible test structures in a periodic arrangement throughout areas of the surface according to the dimensions and spacing of the particle mask. A surface mask of latex or silica spheres protects discrete areas of the substrate from deposition of organosilanes. When the

mask was removed, the uncovered areas of the surface provide sites for further chemical reactions. The changes in size and morphology of the nanostructures were visualized with tapping-mode atomic force microscopy.

Two Zn-phthalocyanine compounds with designed functional groups were synthesized for deposition using particle lithography. Photodynamic therapy has been used to treat pathogenic infections with light-triggered treatments in the presence of phthalocyanines as a photosensitizer.[35] With fluorescent hues of green and blue, phthalocyanines have been used in molecular electronics, textiles, inks, and paint.[36-39] The steps for binding phthalocyanines to amine organosilanes backfilled into nanoholes patterned on silicon and glass substrates were characterized using AFM. Patterned arrays of nanoholes were prepared using steps of particle lithography combined with immersion in organosilane solutions. Organosilanes provide advantages for selecting the chemistry of surfaces with desired carbon chain lengths and functional groups. Methyl-terminated SAMs such as OTMS and PEG-silane were chosen as a resist layer to direct the deposition of the ZnPc compounds. Spatial selectivity was accomplished for directing the attachment of ZnPc to the surface using amine linker chemistry with an amine terminated organosilane, 3-aminopropyltriethoxysilane. Preparing nanostructures of phthalocyanines on surfaces can be challenging. Phthalocyanines tend to stack together through pi-pi interactions, solubility is poor, and aggregation can occur in concentrated solutions. To accomplish immersion particle lithography with phthalocyanines, silica spheres were used as a surface mask to produce nanoholes using protocols with immersion. Latex spheres were used to prepare nanorings with vapor deposition of PEG-silane. Linker molecules of 3-aminopropyltriethoxysilane were successfully backfilled into the nanoholes to form sites for selected deposition of the ZnPcs with a second immersion step. Scanning probe microscopy can be used to probe morphological and physical

properties of nanomaterials deposited on surfaces at the molecular-level. The nanopatterned surfaces exhibit millions of reproducible test structures arranged in a periodic array according to the dimensions and spacing of the surface masks. Examples are shown in Chapter 4.

1.4 Protocols Developed with Particle Lithography using Organosilanes for Patterning Gold Nanoparticles

Studies of nanostructures of silane-functionalized nanoparticles prepared within resists of organosilane nanopatterns produced with particle lithography are described in Chapter 5. Periodic arrays of organosilane nanostructures were prepared with particle lithography to provide a foundation to define sites for attachment of nanoparticles. Wettability, adhesion, and acidity can be controlled by choosing the desired functional head groups of SAMs to provide model surfaces for fundamental studies of interfacial chemistry, solvent-molecule interactions and self-organization.[40] Using octadecyltrimethoxysilane (OTMS) and 2-[methoxy(polyethyleneoxy)-propyl]trichlorosilane (PEG-silane) as a resist, nanopatterns were prepared on a glass surface using particle lithography concurrently with steps of vapor deposition and immersion in solutions. Nanorings and nanoholes were produced using basic steps of particle lithography. The morphology and selectivity of designed surfaces of SAMs formed with OTMS and PEG-silane using steps of particle lithography were evaluated using high resolution atomic force microscopy (AFM). Thickness measurements from AFM cursor profiles were used to evaluate the orientation and density of the OTMS and PEG-silane nanostructures. The direction planned for the designed experiments will apply particle lithography with organosilanes to develop spatially selective surfaces for patterning nanoparticles. Arrays of nanoparticles will provide practical test structures for applications based on localized surface plasmon resonance (LSPR), surface-enhanced Raman scattering (SERS) as well as advanced measurement modes of scanning probe microscopy.

1.5 Synopsis

Chapter 6 provides an overview of the future directions for the research presented in this dissertation. The fundamental studies that were conducted are multidisciplinary, encompassing applications in molecular electronics, photonic studies, materials design and biomedicine. The use of nanopatterns of metalloporphyrins on metal surfaces enables further studies using conductive probe-AFM for probing metal-molecule-metal heterojunctions. Studying the surfaces that have been patterned with metal nanomaterials have impact for understanding energy conversion processes for photovoltaics at the nanoscale. Comparisons of samples with different transition metals as well as diverse metal surfaces can be used to evaluate the best patterning strategy for preparing devices. Studies using linkers with selected functional groups were completed to successfully pattern zinc-coordinated phthalocyanines. With the nanopatterning protocols developed with particle lithography, conductive probe-AFM can be applied to measure charge transport properties of zinc-phthalocyanines at the molecular level. Procedures were also investigated for nanopatterning gold nanoparticles incorporating functional groups to direct the growth of nanoparticles within the nanopatterns of surface test platforms. Nanoscale research will continue to progress in areas such as materials chemistry and nanotechnology to give further insight on fundamental structure and size-dependent properties of nanomaterials.

CHAPTER 2. EXPERIMENTAL APPROACHES USING PARTICLE LITHOGRAPHY AND ATOMIC FORCE MICROSCOPY CHARACTERIZATIONS

2.1 Introduction

Particle lithography is a high throughput surface patterning approach that provides control of the deposition of thin films and nanomaterial using the chemistry of surface self-assembly. Materials that have been patterned include polymers,[41-42] metals,[43-47] organic thin films,[10,24, 26-27, 48-50] nanoparticles,[8,14, 51] and proteins.[9, 52-53] For the research presented in this dissertation, particle lithography was used to pattern surfaces of glass, silicon wafers, and Au(111). An overview of the patterning of nanomaterials using particle lithography to prepare nanostructured surfaces with well-defined selectivity, morphology and reactivity is presented in this chapter. The operating principles of the modes of atomic force microscopy (AFM) that were used for sample measurements are also described.

The AFM was invented in 1986 by Binnig, Quate, and Gerber with the capability of achieving unprecedented resolution at the atomic and molecular level.[54] The advantages for using AFM for surface characterizations include operation in nearly any environment, such as in liquid, vacuum, or in ambient air, with capabilities for dynamic studies to monitor changes in surface morphology that evolve over time using time-lapse AFM. Both conductive and insulating samples can be characterized by AFM without the need for sample pretreatment. Lateral resolution of less than 1 nm and a vertical resolution of 0.1 nm have been achieved with AFM.[55]

2.2 Development of Nanolithography Using Surface Masks of Spherical Particles

A method for preparing organosiloxane monolayers that are homogenous and compact using adsorption to a solid surface was reported by Jacob Sagiv in 1980.[56] An approach which used latex spheres for patterning nanoparticles was described as “Natural Lithography” by Deckman and Dunsmuir.[57] Latex spheres were used to prepare arrays of nanostructures of Ag, Au,

Cr, CaF_2, and CoPc.[58] By depositing spherical particles onto substrate to form surface masks, the subsequent growth of organic thin films and nanomaterials can form well-defined nanoscale patterns. The spheres are removed using selected solvents, only the nanopatterns of the materials that were deposited persist on the surface. Particle lithography has also been referred to as colloidal lithography,[59] nanosphere lithography,[58, 60] evaporative lithography,[8] or natural lithography.[57]

To accomplish particle lithography, solutions of size-sorted, monodisperse spheres of latex or colloidal silica are used to prepare a surface mask through natural self-assembly to form hexagonal lattices on atomically flat surfaces. An example mask of close-packed spheres with hexagonal symmetry is shown with an AFM image in Figure 2.1. The heights of the spheres on the glass surface is shown by the color scale in the topography frame of Figures 2.1A and 2.1C. The bright areas of the spheres indicates a height change and the lighter colored areas represent taller nanostructures. A map of the viscoelastic properties present on the surface is presented in the phase images (Figures 2.1 and 2.1D) revealing a uniform composition for the latex spheres.

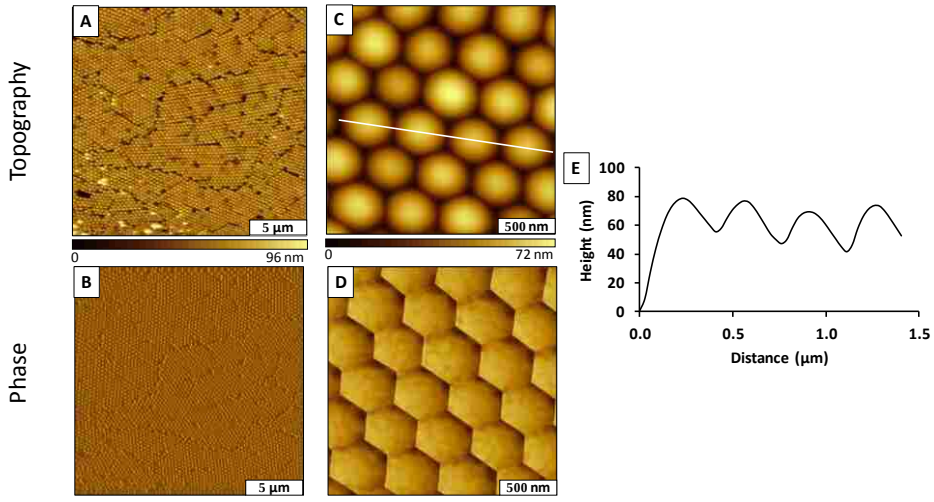

Figure 2.1 Spherical mask prepared with 300 nm latex spheres on glass (A) Tapping-mode AFM topograph (20 × 20 μm^2); (B) corresponding phase image; (C) magnified image (2 × 2 μm^2); (D) corresponding phase image (E) cursor profile for the line in C.

The images of the topography of 300 nm polystyrene latex discloses the arrangement of spheres prepared by drying an aqueous drop of monodisperse spheres on glass in ambient conditions. The interstitial areas in between the spheres provides sites for deposition of evaporated metals, organic vapors or other nanomaterials. Areas where the spherical particles are in contact with the substrate remain protected during deposition processes. The mask of spheres can be removed by rinsing steps, sonication, or dissolution. Periodic structures of spheres with regular geometries and interparticle spacing spontaneously self-assemble on the surface. Spin-coating,[11, 58, 61-62] solvent evaporation,[8, 14, 63] and colloidal self-assembly occurring at an air-liquid interface or in an electric field are approaches that were used to prepare arrays of colloidal spheres.[64-65]

2.3 Surface Assembly of Alkanethiols and Alkylsilanes

Self-assembled monolayers (SAMs) of alkanethiols and alkylsilanes have been practical for surface modification,[9, 66-68] corrosion inhibition,[69-71] biosensor design,[72-75] and molecular device fabrication.[76-77] A requirement for defining surface chemistry at the nanoscale is the ability to create geometrically well-defined architectures with designed chemical functionality. The patterns of SAMs are customizable which provides advantages for designing the chemistry of surfaces with desired functional groups and spacer lengths (Figure 2.2).[56]

By choosing the functional headgroups of SAMs, properties such as wettability, acidity and adhesion can be controlled. Designing surface chemistries to resist or adsorb nanomaterials in further reaction steps can be achieved with SAMSs of organosilanes.[28, 78-79] Organosilane nanostructures of organosilanes can be prepared by depositing molecules through the surface masks of spheres driven by steps of hydrolysis and condensation reactions. The stability and durability of the nanostructures deposited on the surface is derived from the nature of covalent siloxane bonds within silane SAMs.

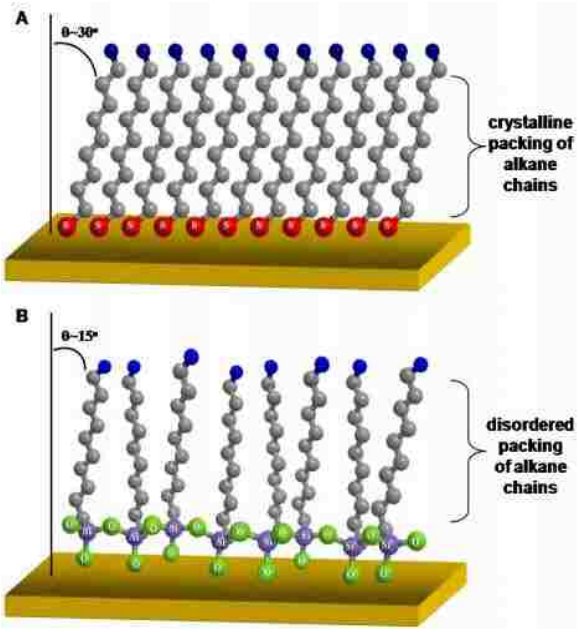

Figure 2.2 General model of the surface structure of (A) organosilanes and (B) alkylthiol SAMs.

Silane SAMs form siloxane bonds that bind to the surface and cross-link to form interconnections with adjacent molecules. Production of silanols, formation of Si−O bridges to adjacent molecules, and connections to the substrate or production of silanols, Si−OH happens simultaneously. The amount of cross-linking depends on various conditions of sample preparation such as the nature of the substrate and immersion solvent and temperature.[40] To bind to the surfaces, organosilanes need nanoscopic amounts of water to initiate the hydrolysis reaction. The interstitial sites of the spheres retain nanoscopic amounts of water which leads to organosilane binding of organosilanes surrounding the base of the sphere. Drying intervals of the masks can be used to regulate the nanoscopic amounts of water present on the surfaces.[26]

The geometry, surface coverage and surface functionalities of the nanopatterns were evaluated using AFM. After the mask of spheres were removed by steps of sonication in ethanol and water, nanoholes within a film of octadecyltrimethoxysiloxane (OTMS) are formed. Examples

are shown in topography and phase images in Figure 2.3. The circular dark areas are the nanoholes of uncovered Si(111) substrate and the brighter areas are the OTMS resist film.

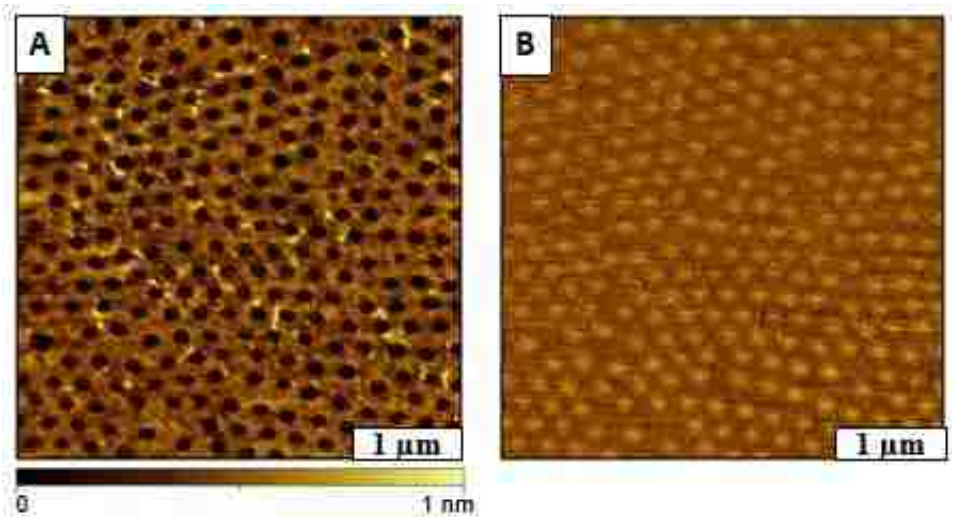

Figure 2.3 Nanoholes within OTMS on Si(111)prepared with particle lithography using a surface mask of 250 nm silica spheres. (A) Tapping-mode topography frame (4 × 4 μm^2) acquired in ambient air; (B) simultaneously acquired phase image.

Densely packed, well ordered monolayers on coinage metal surfaces such as gold have been used to produce SAMs of *n*-alkanethiols.[80-81] Depending on the length of the alkane chain or terminal chemistry of the molecule, the packing density of the SAM can be chosen to specify the film thickness. The basic structure of an *n*-alkanethiol SAM consists of three parts: the tail, the carbon backbone, and the head group. The surface attachment is determined by the tail being composed of thiol molecules for chemisorption. The thiol is bonded directly to the alkane chain that serves as a spacer for tuning the vertical thickness of SAM nanopatterns. Selected functional groups can be used to determine the chemical properties of a surface such as esters, alkyls, hydroxyls, carboxylates, amides, and other functional groups.[28, 82-85] Many alkylthiol compounds are commercially available, depending on the desired application.

The preparation of *n*-alkanethiol SAMs involves immersion of Au(111) substrates in dilute solutions of dissolved thiols in solvents such as ethanol for selected time intervals. Achieving a

monolayer of the *n*-alkanethiol can be accomplished by controlling the solubility of the molecule, concentration of the solution, and the time of immersion it can be accomplished as summarized in Table 2.1.[86] To prevent oxidation of thiols, the exposure to light should be minimized.[87-88] The thiol atoms of *n*-alkanethiol SAMS bind to the triple hollow sites of a Au(111) lattice by chemisorption. [83, 87, 89-91] On bare gold surfaces, the solution self-assembly of *n*-alkanethiol SAMs occurs in a stripe phase and a crystalline phase. In the stripe phase, thiol molecules make contact with the surface and the backbone of the molecules orient themselves parallel to the substrate.[92]

Table 2.1 Examples of the parameters used to prepare *n*-alkanethiols on Au(111).

SAM	Substrate	Concentration (mM)	Time (h)	Temp (°C)	Solvent	Ref.
n-dodecanethiol	Au(111)	0.001	24	25	ETOH	169
1,1,1-tris(mercaptomethyl)heptadecane	Au(111)	0.01	3	25	ETOH	90
16-[3,5-bis(mercaptomethyl)phenoxy]hexadecanoic acid	Au(111)	5	30	25	ETOH	85

Molecules of *n*-alkanethiols eventually rearrange into a standing position with a tilt angle of approximately 30°.[92] The tilt angle has been characterized using grazing incidence X-ray diffraction, IR, near-edge X-ray absorption fine structure spectroscopy, and IR spectroscopy.[93-97] The close-packed commensurate $(\sqrt{3}\times\sqrt{3})R30^{\circ}$ configuration with respect to the plane of the Au(111) lattice is formed by the mature crystalline phase.[98-101] Long range ordering of *n*-alkanethiols and the surface structure have been revealed by STM and AFM to enable views of defect sites such as steps, dislocations, and etch pits.[28, 84, 98] Molecular island vacancies of etch pits are caused by reconstruction of thiols during the binding between the thiols and Au(111) substrate.[83] Etch pits are

viewed as small depressions observed in high resolution images that result from the displacement of atoms of the Au(111) substrate.

A representative AFM topographic image of nanoholes prepared with dodecanethiol on Au(111) is presented in Figure 2.4A that was acquired by tapping-mode in ambient air. The dark areas of the nanoholes reveal sites of exposed gold substrate, whereas the brighter areas are the matrix film of organothiol. The corresponding phase image reveals the differences in tip-surface interactions for a map of elastic properties (Figure 2.4B). Atomic resolution is achieved when images disclose substrates that contain missing atoms, scars, or pinholes which lead to surface roughness. During imaging, the surface looks as though it is rough but from the atomic perspective it is considered flat. During observation of AFM images, the surface may appear rather rough and irregular. However, the surface is quite flat from an atomic perspective. The overall surface roughness for a gold substrate is considered less than 1 nm because the height of gold steps is only 0.25 nm.

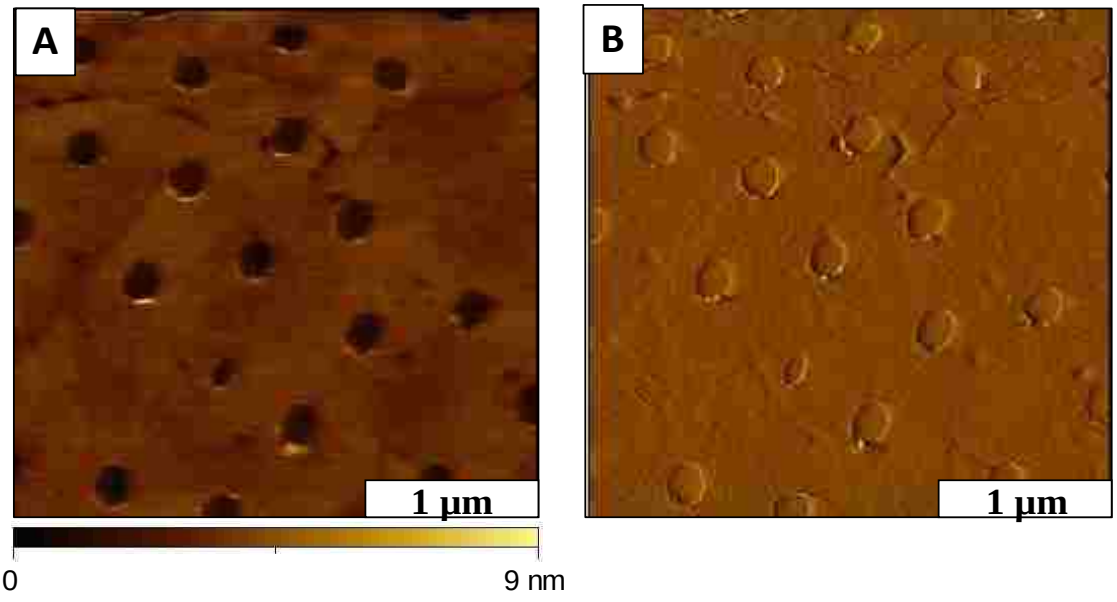

Figure 2.4 Nanoholes of Au(111) formed within a thin-film of dodecanethiol. (A) Topography image (2×2 µm^2); (B) corresponding phase image.

Nanoholes within dodecanethiol are shown in the topography image of Figure 2.5, which displays height changes according to color contrast from dark to light, as a map of the heights of the surface terrain. The gold steps of the underlying gold surface are visible among the nanoholes. The step edges are uneven which reflects the true surface morphology of gold thin films. The dark colors indicate the areas of the nanoholes which are shallower regions within the dodecanethiol monolayer.

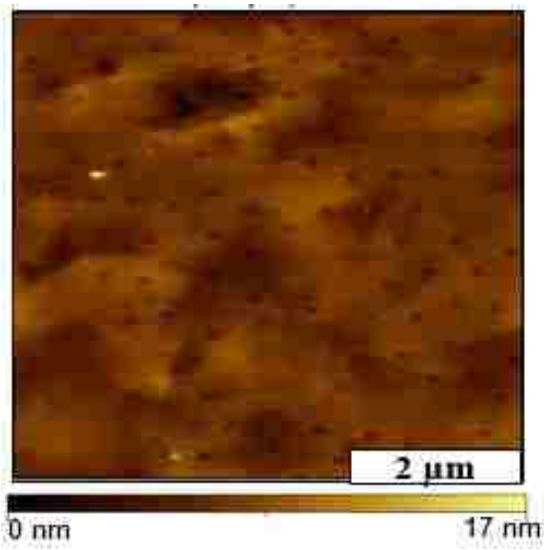

Figure 2.5 Gold steps within a self-assembled monolayer of dodecanethiol nanoholes prepared on Au(111), topography frame, $6 \times 6\ \mu m^2$.

2.4 Approaches for Scanning Probe Lithography

Nanostructures of organic thin films have been produced by x-ray and e-beam lithographies,[102-108] nanosphere lithography,[53, 109-111] and scanning probe-based lithography.[30, 89, 112-114] The highest spatial precision at the level of single molecule resolution has been achieved with scanning probe lithography (SPL). Approaches have been advanced for regulating local tip-material interactions with biological and organic thin film materials by using SPL. Approaches using nanoscale lithography with AFM have been used for nanofabrication with SAMs.[89]

Examples include tip-directed material deposition,[115-116] dip-pen nanolithography (DPN),[117-120] local oxidation nanolithography,[121-124] local chemical or electrochemical lithography,[30, 125] tip-induced catalysis,[126] thermal-mechanical based writing,[127-129] nanoshaving[130-132] and nanografting.[133-134] Nanografting and nanoshaving, enable *in situ* studies with high spatial resolution for features as small as 2 nm.[135]

2.5 Imaging Principle of Atomic Force Microscopy

Characterizations using an AFM requires a sharp probe affixed to the end of a cantilever that is scanned across the surface to collect information about sample morphology. Information about tip-surface adhesion, magnetic forces, frictional forces, elastic compliance and sample conductance can be obtained depending on the configuration of the instrument. The piezoceramic scanner controls the movement of the tip over the sample surface. By applying voltages the cantilever can be moved in the x, y, and z directions. The most common AFM tips are ultra-sharp silicon (Si) or silicon nitride (Si_3N_4) probes which are attached to either a V-shaped or rectangular cantilever. The cantilevers typically have lengths ranging from 10-200 μm and widths of 20-40 μm. The shapes of the apex of the tips are normally square-shaped pyramids or cylindrical cones with a reflective coating on the back of the cantilever. A diode laser is focused on the back of the cantilever while the tip is scanned in a line-by-line raster pattern across the sample. Changes in the deflection or oscillation amplitude of the tip are monitored and detected using a position sensitive photodetector. The setpoint value is used to maintain the tip position through the electronic feedback loop. Images of the sample are digitally constructed by mapping the changes in cantilever deflection caused tip-surface interactions as a function of the tip position. The three primary operating approaches are based on how the AFM tip is operated in proximity with the sample surface: contact, non-contact and intermittent-contact mode. In contact mode, the AFM tip remains

in direct contact with the sample continuously during imaging, whereas in non-contact mode, the tip is maintained at a discrete distance from the sample. When using intermittent-contact mode, also known as tapping-mode, the tip is driven to oscillate at or near its resonance frequency and "taps" the sample during scanning.

2.6 Contact Mode and Lateral Force Imaging

During contact mode imaging, the AFM tip is maintained in direct physical contact with the surface during imaging. Contact mode and lateral force imaging are accomplished simultaneously. A sharp probe at the end of a cantilever is raster-scanned across a surface using a piezoelectric tube scanner. A voltage is applied to the piezoelectric material which causes it to contract or expand for accurate positioning of the tip during a scan. A diode laser is reflected off the back of the cantilever onto a photodetector as shown in Figure 2.6. The bending of the tip during contact mode will produce changes in position, deflection, depending on the sample. Deflection is related to the force applied to the sample and is maintained at a constant setpoint. The feedback loop of the computer controller incrementally adjusts the voltage applied to the piezoscanner to maintain the initial deflection setpoint values for the force applied between the tip and sample. Changes of the surface topography induce bending of the cantilever which affects the vertical displacement of the laser position in the top and bottom quadrants of the photodetector. Lateral displacement of the position of the laser spot is caused by torsional twisting of the cantilever. The lateral force mode of imaging is sensitive to differences in chemical composition and mechanical (friction) properties of the sample.[136-137] Torsional twisting is caused by frictional forces between the tip and the sample as the tip is in direct contact with the surface. Torsional twisting of the tip induces changes in the position of laser spot in the left and right quadrants of the detector, constructing digital lateral force images.[66] Changes in the frictional force between the

tip and sample are mapped by lateral force images as the probe is scanned in contact with the surface. Frictional force images are derived by subtracting the trace and retrace lateral force frames. Lateral force images often show edge features of the surface because tip-surface adhesive interactions are quite different at the sides of nanostructures. For contact mode AFM, topography and lateral force images are acquired simultaneously.

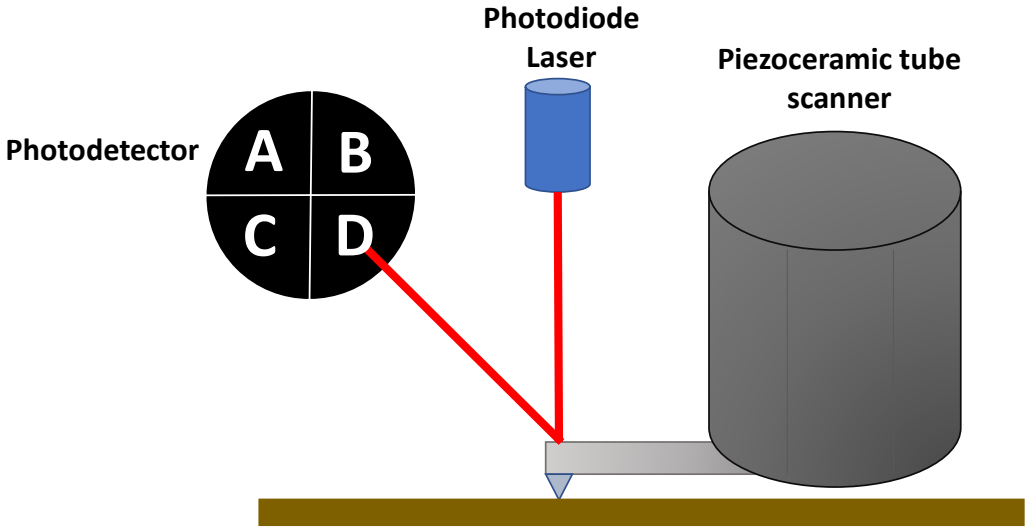

Figure 2.6 Operating principle of contact mode AFM.

There are a few disadvantages to using contact mode caused by shear forces caused by the scanning tip which can damage fragile samples such as biomaterials. To alleviate such problems soft cantilevers with small spring constants can be used to reduce the amount of force exerted on the sample. Depending on the imaging environment, force settings for operating in air can range from 1 to 10 nN, whereas settings less than 1 nN can be applied for imaging in liquid. To successfully image polymers, delicate compounds, or spheres, it is often practical to use tapping-mode to minimize perturbation of the surface.

2.6.1 Force Distance Measurements with AFM

Using AFM force spectroscopy, measurements of tip-sample interaction forces can be accomplished at the nanoscale. The force between the AFM tip and sample can be measured by collecting a force curve during imaging which produces a plot of cantilever deflection as a function of the sample position along the z-axis. The Hooke's law relation used to calculate forces is $F = -kz$, where F is the force, k is the stiffness of the lever, and z is the distance the lever has bent.[138] The force is calculated by measuring the deflection of the lever with knowledge of the stiffness of the cantilever material. Studying force-distance curves while imaging provides knowledge of the physics of contact acquired with pico-newton sensitivity.[139-140]

For an individual approach-retreat cycle in air, force-distance curves display the tip displacement versus the deflection of the cantilever. An example force-distance curve acquired in ambient air for a sample of Zn phthalocyanine is presented in Figure 2.7. The deflection of the cantilever is absent in the region of Label A, where the force between the tip and sample are negligible when the tip is far away from the sample. The interaction with the sample and tip increases as the tip approaches the sample causing the cantilever to bend upward until it locks into contact due to repulsive forces shown in the region of Label B. Label B is used to measure The combined forces of van der Waals interactions and electrostatic attraction between the tip and sample are represented in Region B. The deflection increases as more force is applied to the tip giving the maximum deflection of the cantilever in the area of Label C. The tip will overcome the adhesion forces and detach from the surface during the retraction period Labeled D. The surface energy and binding forces of the materials are estimated in this area of the curve. Acquiring multiple force-distance curves at the beginning and conclusion of sample analyses during an AFM

experiment is standard protocol for calculating the total imaging forces applied to samples for each experiment.

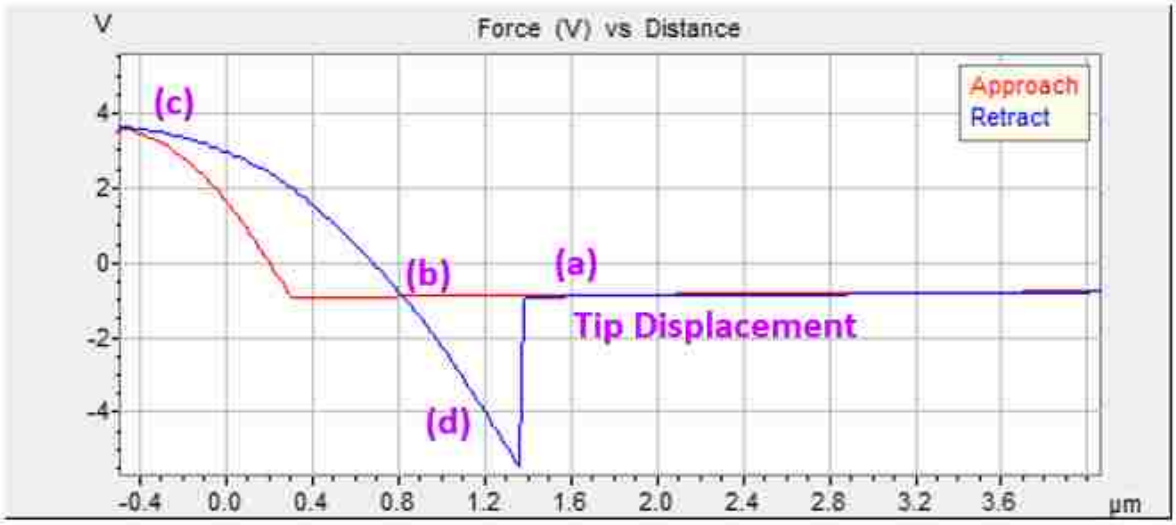

Figure 2.7 A typical force curve acquired in air for a sample of Zn-phthalocyanines patterned on Si (111).

2.7 Tapping-Mode and Phase Imaging

Tapping-mode AFM is used when trying to avoid the challenges faced with contact mode AFM for characterizing loosely bound or easily damaged materials, such as proteins,[70, 72] polymers,[73-74] and nanoparticles.[75] The intermittent contact mode for "tapping" the surface was developed as a method to achieve high resolution without destructive frictional and shear forces. Damage to the tip or sample is minimized with tapping-mode by driving the oscillation of the cantilever near its natural resonance frequency as illustrated in Figure 2.8.

Typical resonance frequencies for tapping-mode tips range from 150 to 300 kHz. With spring constants, around 20-50 N/m, tapping-mode tips are stiffer than for contact mode. The amplitude of the cantilever oscillation ranges from 50 to 100 nm to provide the cantilever with enough energy to overcome adhesion forces between the tip and surface.[141-142] An AC voltage is applied to the piezoactuator within the AFM nosecone to induce tip oscillation. The tip is driven

to intermittently touch the surface caused by the cantilever oscillation during scans. The amplitude of the oscillating cantilever is controlled by the feedback loop to maintain a constant amplitude. The feedback loop uses the error signal to determine the voltage needed to maintain a constant amplitude.[143] The error signal is produced by the difference between the output and driving signals. The measured amplitude is the output signal whereas the setpoint is the driving AC input signal. Images of the surface topography are formed by changes in voltage that are required to maintain a constant amplitude signal.

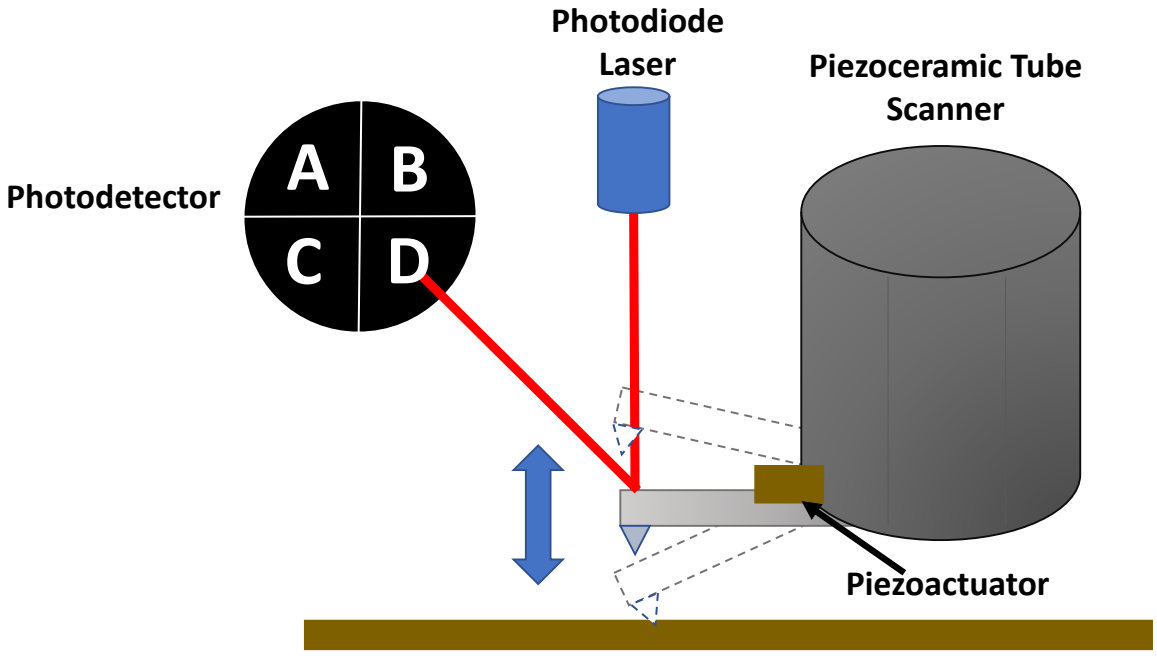

Figure 2.8 Operating principle of tapping-mode AFM.

Phase images are acquired concurrently with topography frames with tapping-mode. The phase lag is sensitive to variations in material properties. Phase images are acquired simultaneously with surface topography with tapping-mode operation and to provide information of surface composition, adhesion, stiffness, and viscoelasticity.[144-146] A lock-in amplifier is used to

measure the phase lag of tip oscillation relative to the driving AC input signal for generating phase images.

2.8 Current Sensing AFM and I-V Measurements

Conductive probe (CP-AFM) is used to measure and map conductive properties of samples at the nanoscale.[147-148] For materials which are conductive or semiconductive, topography and current frames are simultaneously acquired by applying a DC bias voltage to the sample as illustrated in Figure 2.9. To generate the flow of current, a voltage is applied between the substrate and conducting cantilever which is sensitively measured at the AFM tip using a preamp within the nosecone assembly.

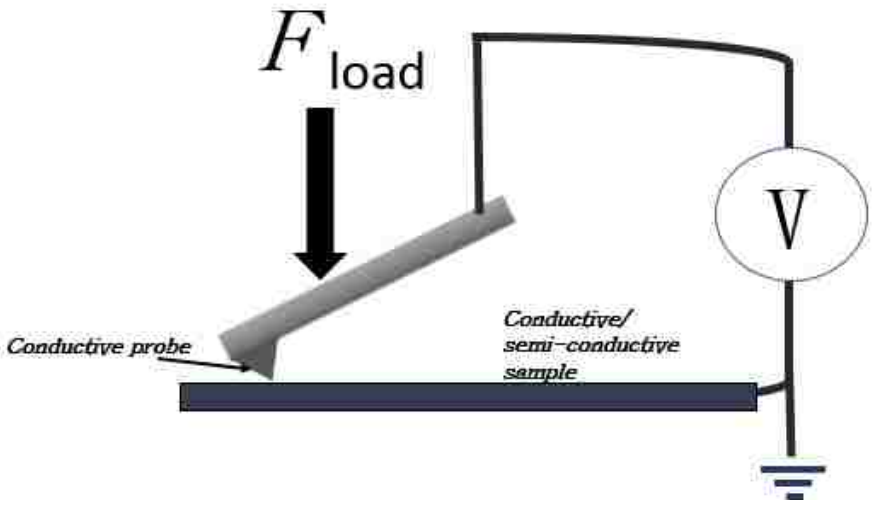

Figure 2.9 Instrument set-up for conductive probe AFM.

The measured change in current is used to construct a spatially resolved conductivity image. Changes in the polarity and magnitude of the bias voltage are measured to produce the contrast for current images. Point measurements of current-voltage (*IV*) characteristics can be measured to obtain a set of measurement points with a selected area of the sample. The CP-AFM mode has been used to characterize organic thin films,[147] nanoparticles[149] and metals.[150]

Measurements of current in the range of hundreds of femto to nearly micro amperes can be acquired by changing the size of the preamp assembly.

2.9 Magnetic Sample Modulation AFM

Magnetic sample modulation is a combination of force-modulation AFM with selective modulation of magnetic domains.[151-152] Using contact mode, a non-magnetic tip is operated using a MAC-mode sample plate to drive the selective modulation of magnetic or paramagnetic samples. An alternating electromagnetic field is applied. An overview of the instrument set-up for MSM-AFM is presented in Figure 2.10.

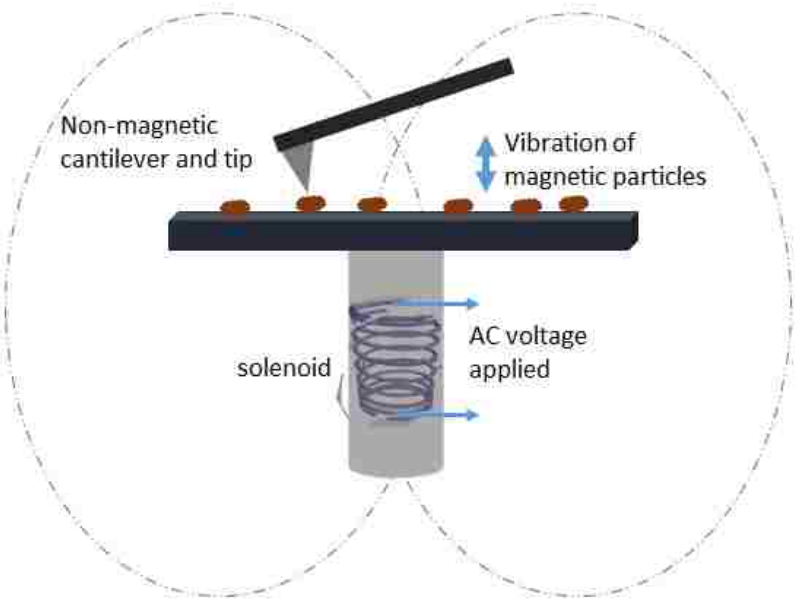

Figure 2.10 Instrument configuration for AFM imaging with magnetic sample modulation.

Magnetic nanomaterials are caused to vibrate when an electromagnetic field is applied. The vibrational motion of the samples are detected with a non-magnetic AFM tip operated in contact mode. The oscillation, flux and strength of the magnetic field are controlled by selecting the parameters for the AC current applied to a wire coil solenoid which is located underneath the sample stage. The periodic motion of the sample vibration is tracked by changes in the deflection

of the AFM tip. Changes in the phase angle and the amplitude of motion as the tip interacts with the sample are plotted as a function of the tip position. Using the AC waveform as a reference signal, digital channels for the amplitude and phase components of the tip motion are obtained by directing an auxiliary output channel from the photodiode to the input of a lock-in amplifier.

Differences in contrast will be produced by the mechanical motion of the sample from the domains vibrating in response to the flux of the AC electromagnetic field. When imaging in MSM mode, it is important to select a nose cone and a nonmagnetic tip without any magnetic material to prevent vibration from external parts other than the sample. Control spectra are acquired while imaging in MSM mode for monitoring the tip trajectory as the AC field is ramped when the tip is lifted from the surface or when the tip is placed at non-magnetic locations of the sample. For magnetic nanomaterials present on the surface, the flux of the alternating magnetic field selectively induces mechanical vibration. The sample must be free to vibrate on the surface and cannot be embedded within the sample.

2.10 Conclusion

Particle lithography has been a successful method for the deposition of nanomaterials such as metals, polymers, organic thin films and inorganic samples. Particle lithography serves as an excellent method that is a highly reproducible and robust for patterning nanoparticles, porphyrins, and phthalocyanines which will be described within this dissertation. Depending on the diameters of the latex or silica spheres that were used, the periodicity and arrangement of nanostructures can be controlled to dimensions as small as 100 nm. Organosilane and alkylthiol chemistry was implemented for the linking materials to the surface with further steps of nanofabrication. The samples were characterized using tapping-mode, contact mode, and MSM-AFM. Characterizations with SPM enable *ex situ* studies of the changes of surface after key steps of

nanofabrication. Future investigations will address the suitability of particle lithography for preparing nanostructures for applications in photoelectronics and sensing.

CHAPTER 3. SURFACE ASSEMBLY OF ORGANOTHIOLS AND PORPHYRINS ON Au(111) INVESTIGATED USING SCANNING PROBE LITHOGRAPHY

3.1 Introduction

In nature, porphyrins are used in oxygen transport and storage, electron transport, and harvesting of light energy.[153] From a biological point of view, during photosynthesis the porphyrin derivative chlorophyll A absorbs photons from sunlight for conversion into chemical energy through charge-transfer processes. Processes for molecular electronics can use the same energy transfer processes when porphyrin molecules are used for device designs. Applications such as photovoltaics cells generate electricity directly from the sun by an electronic process that occurs in semiconductors.[154] Electrons solar energy can be induced to travel through electronic circuits. The surface assembly of porphyrins has been of interest for molecular electronics and are influenced by the binding interactions between the surface and peripheral groups. Metalloporphyrins have been proposed as constituents because of the intermolecular interactions between macrocycles for molecule-based information-storage devices,[155-158] photovoltaic cells,[159-161] and organic light emitting diodes.[162-163] With the diverse structural motifs associated with porphyrins the thermal stability, electrical, optical and chemical properties of metalloporphyrins furnish exceptional materials for molecular electronics.[164] The organization of porphyrins on a surface can be attributed to the function and efficiency of the samples.[165] A challenge for producing monolayer films of porphyrins on surfaces is the π-π interactions between the macrocycles at high concentrations. The porphyrins can aggregate in solution in the form of nanocrystals or stacked arrangements. Previously, porphyrins have been reported to adapt a coplanar arrangement on surfaces showing incomplete surface coverage and low-density.[166]

Preparation of *n*-alkanethiol SAMs with functional groups designed for binding porphyrins to the substrate consists of immersion of Au(111) in dilute solutions of the thiol dissolved in ethanol for selected time intervals. The steps for particle lithography with immersion steps are shown in Figure 3.1. To produce a hydrophilic surface, pre-treatment of the gold substrates were treated using UV-irradiation to render the surface to be sufficiently hydrophilic for particle lithography. Studies with single molecules of porphryins have been done using STM, along with investigations of the conductivity of porphyrins.[167-168] The conductive properties of metalloporphyrins have also been studied using conductive probe AFM.[169-172]

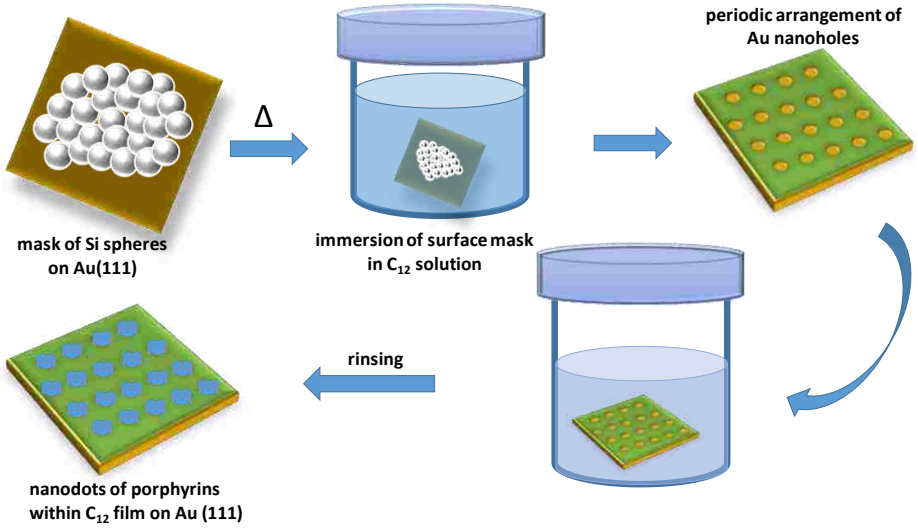

Figure. 3.1 Procedure for preparing nanopatterns of porphyrins using particle lithography with successive immersion steps.

3.2 Experimental Details

3.2.1 Materials

Gold pellets (99.99% purity) were purchased from Ted Pella (Redding, CA). Ruby muscovite mica was acquired from S&J Trading Inc., (Glen Oaks, NY). Size-sorted monodisperse silicon spheres (1 wt% solution) with a particle diameters of 200, 300 and 500 nm were obtained from Thermo Scientific (Fremont, CA) and used as surface masks during the immersion steps with

organothiols. The reagents 5,10,15,20-tetraphenyl-21H,23H-porphine (TPP), 1-dodecanethiol, and dichloromethane were purchased from Sigma Aldrich (St. Louis, MO) and used without further purification. The compound 5,10,15,20-tetraphenyl-21H,23H-porphine nickel(II) (TPN) was synthesized by Professor Vicente's group. Ethanol was purchased from Deacon Labs (Prussia, PA) and was used a received.

3.2.2 Preparation of Template-Stripped Au(111)

The process for preparing template-stripped gold (TSG) was reported previously.[85, 173] Using a high-vacuum thermal evaporator (Angstrom Engineering Inc., Kitchener, OR) a thin layer, approximately 150 nm of gold was thermally deposited onto mica at 10^{-7} Torr. Freshly cleaved Ruby muscovite mica was preheated to 350°C prior to gold deposition using quartz lamps. The gold pellets were thermally evaporated and deposited onto mica at 10^{-7} Torr at a deposition rate of 3 Å/s. The gold films were annealed at 365°C in vacuum for 30 min and then cooled to room temperature before removing samples from the deposition chamber. The gold substrates and glass slides were cleaned with deionized water and placed into a UV-ozone generator for 30 min to further clean and hydrolyze the surface. Epoxy (EPO-TEK, Billerica, MA) was applied to the cleaned glass slides and then attached onto the gold to make films on gold slides. The sample was then heated in oven at 150°C for 2 h to anneal the epoxy. After annealing, the glass pieces were carefully peeled from the mica to produce TSG with atomically flat surfaces.

3.2.3 Preparation of a Dodecanethiol Resist using Immersion Particle Lithography

Surface masks for immersion particle lithography were made by depositing monodisperse silica spheres onto freshly stripped TSG. The spheres were cleaned before using by taking 400 μL of a suspension of silica spheres and transferring them into a plastic microcentrifuge tube. The spheres were centrifuged for 10 min at 20,000 rpm. The supernatant was decanted and then

deionized water was added to the centrifuge tube for rinsing. The spheres were resuspended into deionized water by vortex mixing. Centrifuging steps were repeated four times. A volume of 15 μL of the mesosphere suspension was deposited onto TSG and dried in ambient conditions. Before immersing into thiol solutions, the surface masks were placed into an oven at 150°C for 12 h to anneal the spheres to the substrate.

3.2.4 Preparation of Porphyrin Nanostructures using Immersion Particle Lithography

The samples with a surface mask of silica spheres were cooled to room temperature (25°C), then immersed in a dodecanethiol/ethanol solution (10^{-3} M) for 24 h. Dodecanethiol formed on the exposed areas of the TSG surfaces surroundmg the areas protected by the spheres. The spheres were removed in a subsequent step by sonication in ethanol. Nanoholes were fabricated within a matrix film of dodecanethiol, $CH_3(CH_2)_{11}SH$. The center-to-center spacing between the nanoholes matches the diameter of the mesospheres. The samples with nanoholes were immersed into a 10^{-7} M solution of TPP or TPN in dichloromethane/ethanol (1:10000 vol.) for 30 h to produce porphyrin nanostructures. Samples were rinsed with ethanol and dried under argon for AFM studies.

3.2.5 Characterization of Nanopatterns using Scanning Probe Microscopy

Scanning probe characterizations of samples were obtained in ambient conditions with a model 5500 scanning probe microscope (Keysight Technologies, Santa Rosa, CA). Ultrasharp non-contact silicone cantilevers NSC15/CR-Au (MikroMasch) with a resonance frequency of 325 kHz and a force constant of 40 N m^{-1} and silicon probes with aluminum reflex coating with an average resonant frequency of 300 kHz and a force constant of 40 N m^{-1} (Budget Sensors) were used for AFM imaging with tapping-mode. Digital images were processed with *Gwyddion* open source software (version 2.47).[174]

3.3 Results and Discussion

3.3.1 Nanoholes within a Dodecanethiol Film Prepared by Immersion Particle Lithography

Self-assembled monolayers of alkanethiols have been used for development of nanodevices for electronics, prevention of corrosion, and modification of wetting and wear properties for solid surfaces.[91, 175-177] The reliability and durability of organic thin films is limited because of the stability of organosulfur-based SAMs on noble metal surfaces.[178] Studies have shown that *n*-alkanethiol molecules are well-ordered to form a commensurate $(\sqrt{3}\times\sqrt{3})R30^{o}$ lattice on Au(111) with backbones tilted approximately 30º from the surface.[28, 84, 179] Studies have shown that thiol SAMs formed with longer alkane chains are more thermally stable than those formed with shorter chain lengths.[83, 100, 180] In an alkanethiol-gold system, the exchange of sulfur atoms on a gold surface is a dynamic process during surface assembly.[181]

Immersion particle lithography was used to produce nanoholes within dodecanethiol. The organothiol molecules deposit between the interstitial sites of the spheres. After removal of the spheres through steps of rinsing and sonication, the arrangement of exquisitely small nanoholes is apparent with a periodicity of 500 nm, matching the diameters of the silica mesospheres that were used as a surface mask. An example of the nanoholes is shown in Figure 3.3. The areas of the dodecanethiol resist layer are shown with brighter contrast in the topography frame of Figure 3.2A. The darker areas are the bare gold substrate that were protected by the Si spheres. The differences in surface chemistry between the nanoholes and surrounding matrix are mapped with the simultaneously acquired phase image (Figure 3.2B). A magnified view of 14 nanoholes is shown in the topography frame of Figure 3.2C, revealing the characteristic features of dodecanethiol/Au such as etch pits and step edges. The sizes of the nanoholes depend on the actual area of contact between the sphere and the planar surface. The shapes and sizes of the nanoholes are apparent in

the corresponding phase image of Figure 3.2D. Phase images reveal fine details of the edges of surface features and are not distorted by changes in height.

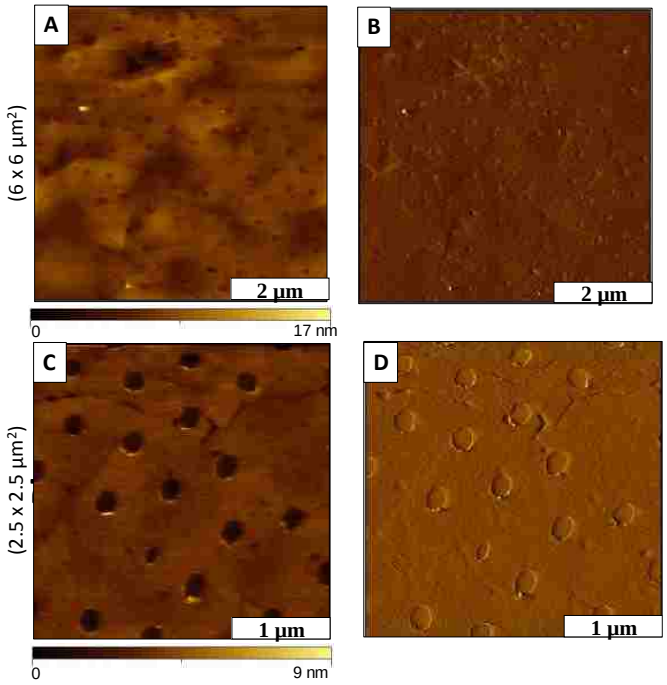

Figure 3.2 Nanoholes with decanethiol prepared on Au(111). (A) Nanoholes of dodecanethiol shown with an AFM topograph (6×6 µm^2) acquired with tapping-mode AFM in ambient air; (B) corresponding phase image; (C) magnified image (2.5×2.5 µm^2); (D) corresponding phase image.

A close up view of a single nanohole is shown in Figure 3.3. A circular area of the substrate is exposed which is approximately 200 nm in width (Figure 3.3A). The shape of the nanoholes indicates that actual area of physical contact between the spheres and the substrate. The area of the nanohole is brighter than the surrounding matrix of dodecanethiol in the corresponding phase image (Figure 3.3B) indicating the differences in surface chemistry presented at the interface. The local morphology of the film is apparent for the sample at the nanoscale. The depth of the nanoholes measured 2.0 ±0.3 nm as shown with a representative cursor profile (Figure 3.3C). The value matches the expected thickness of a single layer of a densely packed dodecanethiol film.

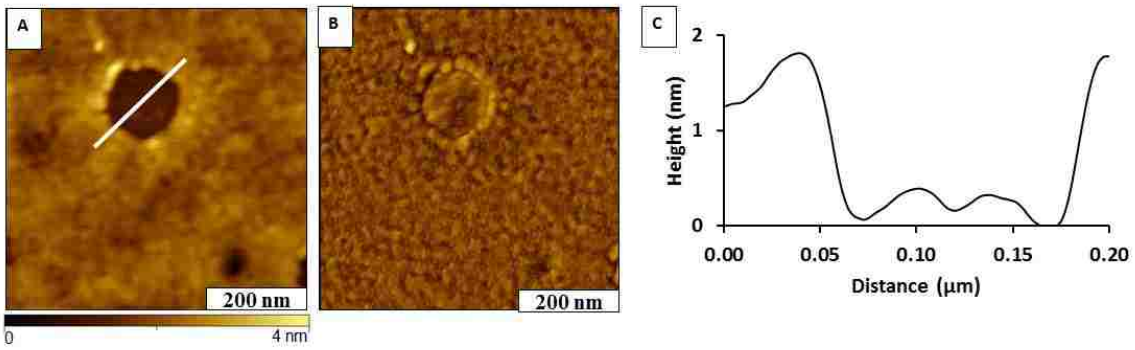

Figure 3.3 Single gold nanhole within a dodecanethiol thin-film. (A) Magnified fiew of a single nanohole ($0.6 \times 0.6\ \mu m^2$) acquired with tapping-mode AFM in air; (B) corresponding phase image; (C) cursor profile for the line in B.

3.3.2 Nanopatterns of TPP and TPN Prepared using Immersion Particle Lithography

The nanoholes within dodecanethiol were immersed into dilute solutions of TPP and TPN to produce nanodots. Chemical models of the compounds that were patterned are shown in Figure 3.4. Dilute solutions were prepared to prevent aggregation and π-π stacking of the porphyrin structures. The designed porphyrins bind within the nanoholes because the methyl-terminated dodecanethiol layer should resist adsorption of new molecules. Porphyrins with a coordinated metal were tested to prepare well-defined test structures for measuring conductive properties. In Figure 3.4A, the structure contains macrocyclic rings with metal-free center and the R groups are benzene rings. Figure 3.4B representats a metalloporphyrin because it contains a nickel bridged within the macrocyles by nitrogen groups. The R groups present on Figure 3.4B also represent benzene rings.

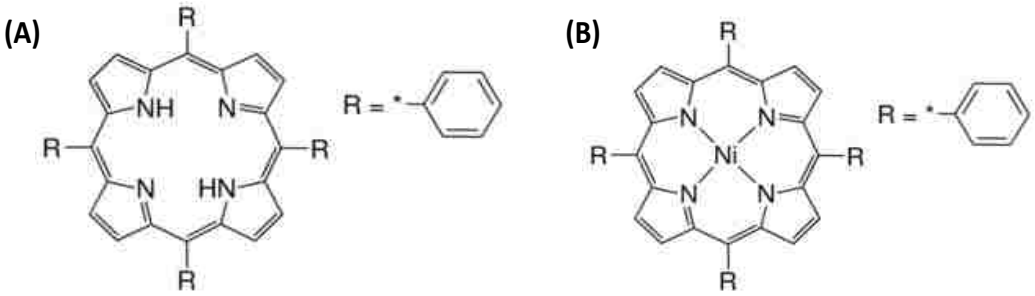

Figure 3.4 Chemical model of (A) 5,10,15,20-tetraphenyl-21*H*,23*H*-porphyrin (TPP) and (B) 5,10,15,20-tetraphenyl-21H,23H-porphine nickel (II) (TPN).

After 30 h immersion in a soluton of TPP, clusters were grown within the nanoholes and also on the resist, as evident in the topography frames of Figure 3.5. Successive zoom-in views reveal that the dodecanethiol matrix did not prevent the onspecific adsorption of TPP and is not a suitable resist. The pendant R groups present on the compound are benzene rings which do not have a strong affinity for the bare gold substrate within the nanoholes. An area without nanoholes provides a frame of reference for the magnified images. The random arrangement of bright dots of TPP throughout the surface are more clearly viewed in Figures 3.5B and 3.5C. There are 12 nanoholes within the topography frame of Figure 3.5C. Interestingly, TPP adsorbed in the center of the nanoholes and is not attached at the edges of the circles.

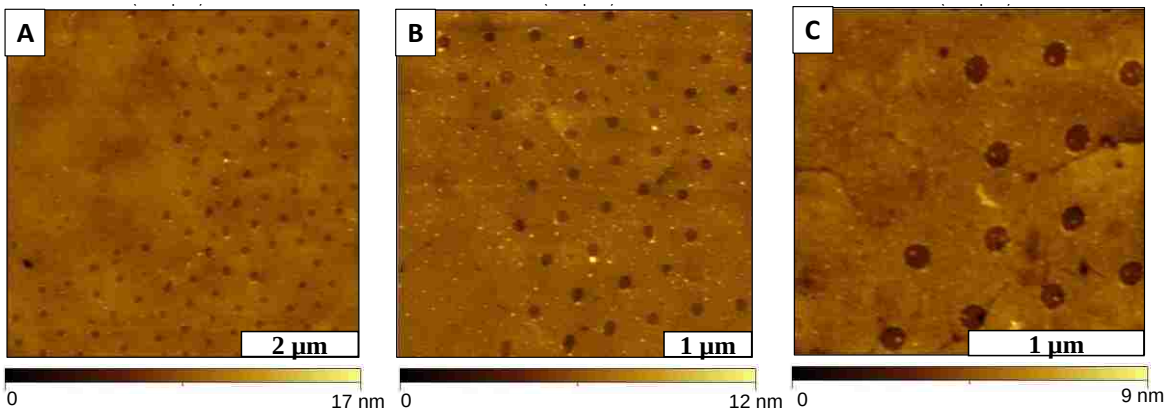

Figure 3.5 TPP Nanodots prepared within dodecanethiol on Au(111) imaged with tapping-mode AFM in air. (A) Nanodots of TPP shown with an AFM topograph (6×6 µm^2); (B) magnified view (4×4 µm^2) (C) close-up view of a single nanostructure (2×2 µm^2).

The TPP nanodots are indicated by the bright nanoclusters present on the dodecanethiol resist and within the nanoholes, as shown in Figure 3.6A. Isolated clusters of TPP adsorbates can be discerned within and surrounding the nanoholes in the simultaneously acquired phase image of Figure 3.6B. The circular small dots are molecules of TPP, Details for a single nanohole is presented in Figure 3.6C along with the corresponding phase image in Figure 3.6D. The cursor profile (Figure 3.6E) was derived from the line in Figure 3.6C indicating the height of the adsorbate within the nanohole to be approximately 1.2 nm. This is roughly the dimension of a single TPP molecule. The lateral dimensions are larger than the surface feature, due to the broadening of the measurement by convolution of the tip size and geometry.

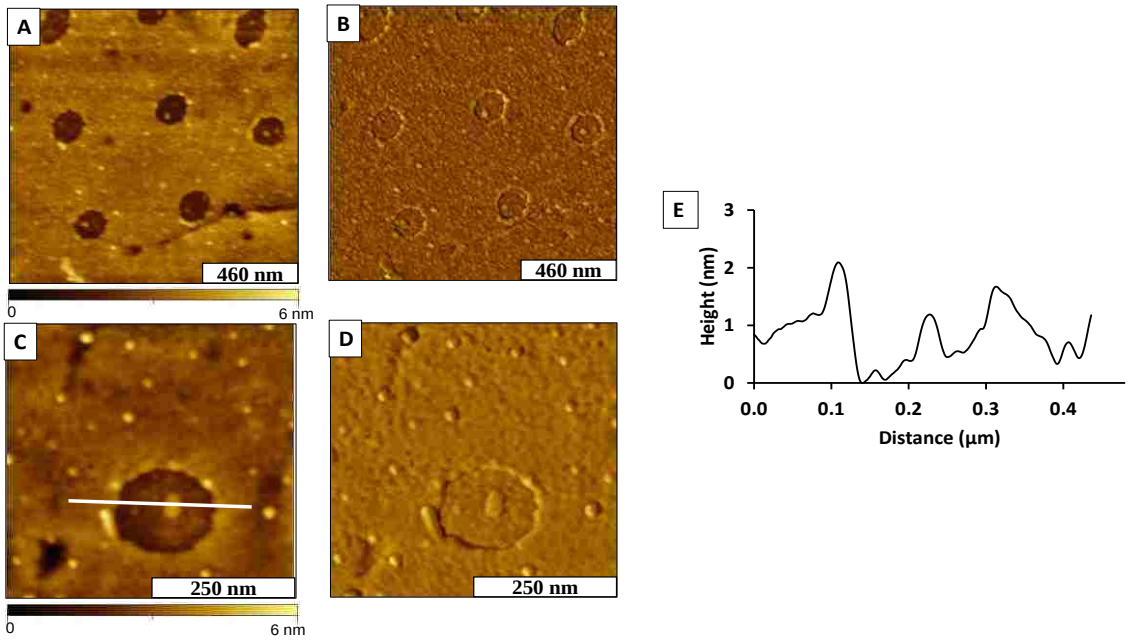

Figure 3.6 Clusters of TPP that formed within nanoholes and on the surrounding dodecanethiol thin-film. (A) Topography image of TPP nanodots (1.4 ×1.4 µm^2); (B) corresponding phase image; (C) Magnified view of an isolatedTPP nanocluster within a nanohole (0.5×0.5 µm^2); (D) Corresponding phase image; (E) Cursor profile for the line in C.

Parameters of immersion time and concentration were evalutated for binding the TPP into nanoholes within a dodecanethiol resist (Figure 3.7). After 48 h of immersion the TPP did not successfully bind within the nanoholes as revealed in Figure 3.7A. There are a few sparse

adsorbates of TPP for the sample, as evident in the corresponding phase image is of Figure 3.7B. The depth of the nanoholes measured 2.0 ± 0.3 nm as indicated with a representative cursor profile in Figure 3.7CImmersion at higher concentration of TPP was investigated for the experiment in Figures 3.7B and 3.7C. Greater surface coverage of TPP clusters are present throughout the surface. A triangular facet of the TSG is visible in the top of the image of Figure 3.7C.

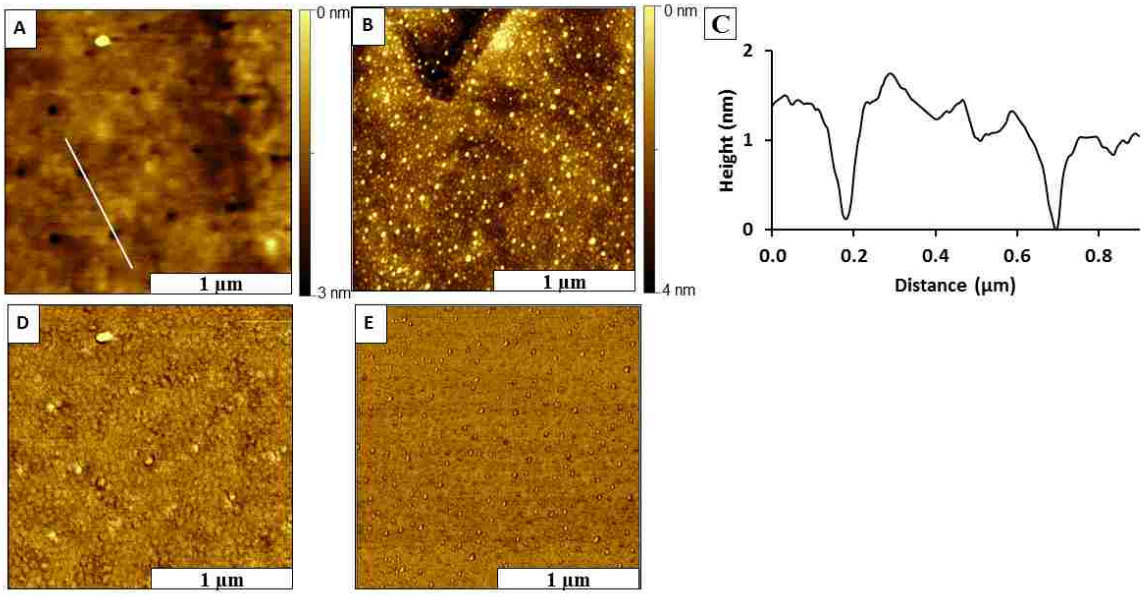

Figure 3.7 Binding of TPP using selected parameters. (A) Topograph (2×2 µm^2) of TPP clusters after 48 h immersion; (B) corresponding phase image; (C) Cursor profile for the line in A. (D) Topograph of TPP clusters prepared at higher concentration 10^{-5} M (2×2 µm^2) (E) Corresponding phase image.

The samples with nanoholes within dodecanethiol were immersed into dilute TPN solution for 30 h in ambient conditions and the results are shown in Figure 3.8. In this example, successful patterning within the nanoholes was achieved, with the localization of TPN within areas of the nanoholes. The attachment occurs near the edges of the nanoholes, rather than in the very center areas, as revealed in the topography frame of Figure 3.8A. The height measures approximately 3.5 nm for the clusteres of TPN, shown with a repreentative cursor profile in Figure 3.8B. The value

corresponds to the dimensions of either a bilayer stack of TPN, or an upright configuration for the molecule.

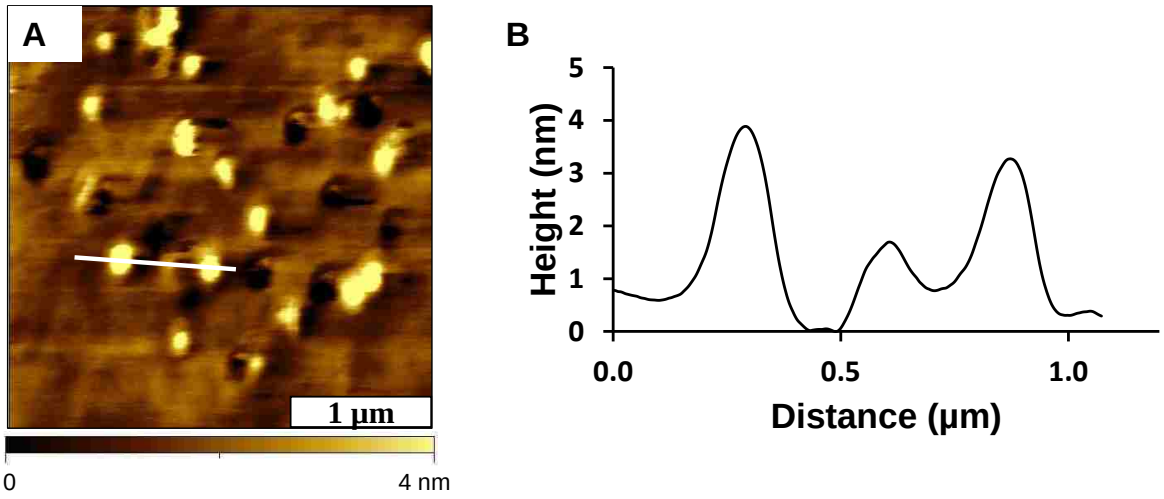

Figure 3.8 TPN Nanodots on Au(111) prepared using particle lithography with dodecanethiol imaged with tapping-mode AFM in ambient air. (A) Clusters of TPP shown with an AFM topograph (3×3 µm^2); (B) cursor profile for the line in A.

The resist layer of dodecanethiol surrounding the clusters of TPN is methyl-terminated which for the most part prevented the nonspecific adsorption of TPN for this experiment. Porphyrins tend to bind to a flat surface in a stacked arrangement, with the macrocycle of the molecules oriented parallel to the substrate due to strong π-π interactions between the planar molecules and the gold surface. However when nickel was coordinated to the center of the macrocyle, the nature of surface binding was changed.

3.4 Conclusions

A platform prepared with immersion particle lithography was evaluated for making preparing nanostructures of porphyrins on gold substrates. Nanodot structures of porphyrins with and without a metal center were selected for studies of surface self-assembly within nanoholes in a matrix film of dodecanethiol. Future directions will be to measure the conductive properties of the TPN and TPP porphyrins at the molecular level using conductive probe AFM.

CHAPTER 4. NANOPATTERNS OF ZINC PHTHALOCYANINES PREPARED USING PARTICLE LITHOGRAPHY: CHARACTERIZATION OF PATTERNING STEPS WITH SCANNING PROBE MICROSCOPY[34]

4.1 Introduction

Phthalocyanines are stable synthetic tetrapyrrolic compounds with interesting spectroscopic properties and architectural flexibility. Phthalocyanines (Pcs) have a macrocyclic aromatic system that produces a high degree of π-electron delocalization which means the compound can easily donate and accept electrons.[182] Phthalocyanines with metals chelated in the center can form coordination complexes to the macrocycles formed by four pyrroles. Phthalocyanines have been used as dyes and pigments in printing, painting, textile and paper industries, chemical sensors, bioimaging, and photodynamic therapeutic agents.[36-39, 183] High-tech applications of phthalocyanines include materials for electrophotography, photoconducting agents, photoelectronics, and organic solar cells.[184-186] Phthalocyanine complexes with non-transition elements such as Zn have shown photodynamic activity against tumor cells, viruses, and bacteria which can be attributed to the efficacy as a reactive oxygen species generator.[187-190]

Planar molecules of phthalocyanines (Pcs) have an extended pi-conjugated system and form several distinct crystalline structures with characteristic physical and chromophore properties.[191] Phthalocyanines containing metal complexes have been widely used because of the properties of color and chemical stability. Metal containing Pcs that have been studied include Cu^{2+}, Ni^{2+}, Co^{2+} and Zn^{2+}.[192]

The self-assembly of Pcs to form uniform thin films has been investigated.[193-194] Functional groups such as amines, hydroxyl and carboxylic acids impart specific physical characteristics to phthalocyanines such as solubility and reactivity.[195] The molecular self-assembly of thiol-derivatized Pcs onto gold substrates via chemisorption have been reported.[196-198] Nanostructures

of Pcs have been prepared on substrates with nanoimprinting lithography,[199] fabrication methods and electrophotolithography.[200-201] The structure and optical properties of thin films of ZnPc and AlPc prepared by vacuum sublimation were investigated by Kment et al.[202] The effect of temperature, film thickness and type of substrate was evaluated for samples of ZnPc prepared by vapor thermal evaporation.[203] The effects of annealing temperature on the optical and structural properties of vacuum evaporated ZnPc thin films deposited at room temperature (30 °C) on quartz glass and Si(100) substrates was investigated by Chowdhury et al.[204] The effects of substrate temperature were examined for films of zinc(II) tetra-tert-butyl-phthalocyanine and zinc(II) phthalocyanine deposited on substrates of bisphenol A polycarbonate.[205] The structure of ZnPc thin films coated on glass substrates by thermal evaporation was reported by Senthilarasu et al.[206] The structure and morphology of ZnPc films of 80 nm thickness were investigated that were prepared by evaporation on glass and Au-coated glass substrates after annealing at selected temperatures.[207]

Periodic arrays of organosilane nanostructures prepared with particle lithography provide unique test structures to use as well-defined nanocontainer sites to define the location of further surface reactions, such as with Pcs. The wettability, adhesion, and acidity of the interface can be controlled by choosing desired functional groups of organosilanes.[208] Our approach is to use protocols of particle lithography with organosilanes to provide model surfaces for fundamental studies of interfacial chemistry and molecular self-assembly. Particle lithography has been used to prepare patterns of self-assembled monolayers (SAMs),[209-214] metals,[215-216] nanorods,[217] nanoparticles,[15, 218-220] and proteins.[221-222] Substrates that were covered with a thin metal film under colloidal spheres were irradiated with polarized beams to produce nano-objects for plasmonic applications.[223]

The kinetics of surface reactions are dependent on the concentration and reactivity of the reagents. For nanolithography studies, small microliter volumes of dilute reagents are appropriate for preparing samples with particle lithography. Two resists were tested to evaluate the selectivity for patterning Pcs. The organosilanes that were selected as the resist film contained either a methyl group or a pegylated chain to minimize the nonspecific binding of APTES on areas between nanopatterns of ZnPcs. Molecules of Zn-Pcs that were functionalized with either a hydroxyl or an isothiocyanate groups were successfully patterned within matrix films of octadecyl-trimethoxysilane (OTMS) and 2-[methoxy(polyethyleneoxy)propyl]trichlorosilane (PEG-silane). An amine-terminated linker molecule, (3-aminopropyl)triethoxysilane (APTES), was deposited within nanoholes prepared with particle lithography to furnish sites to attach ZnPcs. The chemical and physical properties of the nanostructures were then characterized with scanning probe microscopy (SPM) after each step of the surface assembly reactions.

4.2 Experimental

4.2.1 Materials and Reagents

Phthalocyanine compounds were synthesized as previously reported.[224] Polished silicon wafers were used as substrates that were obtained from Ted Pella, Inc. (Redding, CA). Concentrated sulfuric acid (98.0%) (J.T. Baker Fisher, Scientific) and hydrogen peroxide (30%) (British Drug Houses, VWR) were used as received. Size-sorted monodisperse silica and latex mesospheres with diameters of 250 and 300 nm were obtained from Thermo Scientific (Fremont, CA) and used as surface masks for particle lithography. Octadecyltrimethoxysilane (OTMS), (3-aminopropyl) triethoxysilane (APTES), and 2-methoxy(polyethyleneoxy)propyl]trichlorosilane (PEG-silane) were purchased from Gelest (Morrisville, PA) and used without further purification. Ethanol was

purchased from Deacon Labs (Prussia, PA) and used as received. Anhydrous toluene was purchased from Merck Millipore (Billerica, MA).

4.2.2 Synthesis of Zinc Phthalocyanines

The synthesis and purification of ZnPcs 1 and 2 was according to the procedures reported in literature.[224-225] Briefly, ZnPc 1 was prepared from the reaction of 3-hydroxyl,6-triethyleneglycolmonomethyl-phthalonitrile with unsubstituted phthalonitrile in the dimethylaminoethanol (DMAE) using a catalytic amount of DMN and excess zinc(II) acetate [226]. Using a similar procedure, ZnPc 2 was synthesized from 3-(4-N-Boc-aminophenol)phthalonitrile and unsubstituted phthalonitrile. The resulting Pc was deprotected using trifluoroacetic acid, and the amine group converted to isothiocyanate using 1,1'-thiocarbonyldi-2,2'-pyridone in dimethylformamide.[225]

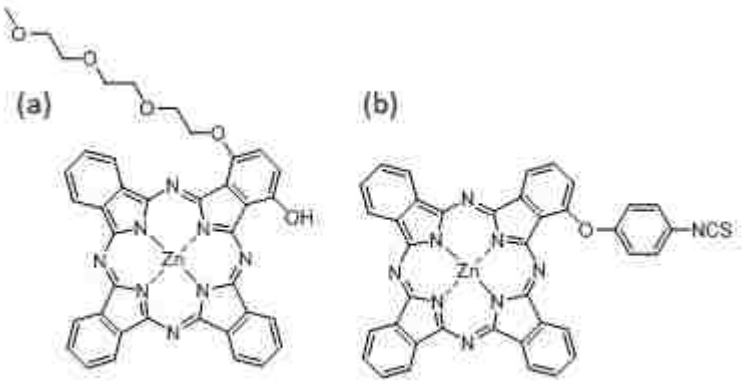

Figure 4.1 Structures of ZnPcs that were patterned with particle lithography. (a) ZnPc 1; (b) ZnPc 2.

4.2.3 Method for Cleaning Silica and Latex Spheres

Standard dry form Angstromsphere silica powder was cleaned and dispersed prior to use as template for particle lithography. First, 0.1 g of silica particles were sonicated in 10 ml of absolute ethanol for 30 min. When the powder was completely dispersed in solution, a 400 μL aliquot was transferred into a plastic centrifuge tube and diluted with deionized water to 1 mL. The mixture

was centrifuged four times (10 min each cycle) at 20,000 rpm. The solid pellet was re-suspended in 1 mL of deionized water by vortex mixing in between each centrifuge step. The solid pellet of final centrifugation step, was resuspended in 400 μL of water. Latex spheres were cleaned using the same method.

4.2.4 Overview of the Two Nanopatterning Protocols

Surfaces were designed for the selective nanopatterning of Pcs to produce multicomponent nanopatterns as shown in Figure 2. In the first step, spheres were deposited on a clean substrate and dried in ambient conditions. Nanoscopic amounts of water are formed surrounding the bottom of the spheres to provide sites for the hydrolysis and condensation reactions with the selected organosilanes. Areas of the surface with direct contact of the spheres are protected from silane binding. In the top panel, OTMS the substrate containing the mask of silica spheres was immersed in a solution of OTMS. In the lower panel of Figure 2, a mask of latex spheres was exposed to PEG-silane using a vapor deposition step to form ring nanostructures. For both procedures, the mask of latex or silica sphere were removed by sonication. In the final step, ZnPcs were attached to the sample with an immersion step.

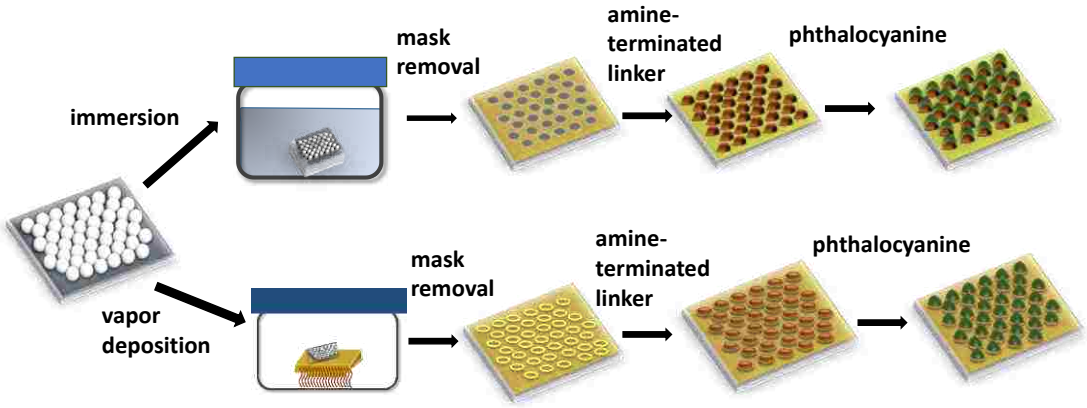

Figure 4.2 Outline of the steps for particle lithography to prepare nanopatterns of Zn-phthalocyanines using protocols with steps of solution immersion (top) or vapor deposition (bottom).

4.2.5 Preparation of Nanoholes within a Film of OTMS using Particle Lithography with Steps of Immersion

Nanoholes within an OTMS SAM was prepared by a previously reported procedure.[213, 227] A suspension (5 μL) of cleaned silica spheres (250 nm) was deposited onto piranha cleaned silica substrates and dried under ambient conditions for 4 h. The surface mask of a dried film of spheres was immersed in OTMS (5 mM) in anhydrous toluene for 1 h. During the immersion step molecules of OTMS form a surface film on areas of the silica substrate that are not protected by the mask of spheres. Samples were rinsed by sonication with ethanol for 30 min to remove the surface mask. The samples were further cleaned by sonication in deionized water and ethanol for 30 min and then dried under nitrogen.

4.2.6 Preparation of Nanorings within a Film of PEG-silane using Particle Lithography with Vapor Deposition

Particle lithography with vapor deposition was used to generate organosilane nanopatterns on surfaces, as previously reported.[213] A 10 μL suspension of clean latex spheres was deposited onto piranha cleaned silica substrates and dried under ambient conditions for 4 h. The substrate containing the dried film of latex spheres was placed into a sealed vessel for vapor deposition in an oven for 12 h. A drop (200 μL) of PEG-silane was placed into the sealed vessel. During the heating step, the silane became a vapor and deposited on the masked substrate at 70°C. After heating, the samples were rinsed with water then the latex spheres were removed by sonication in ethanol and deionized water.

4.2.7 Deposition of APTES and Zn(II)-Pcs using Steps of Immersion in Dilute Solutions

Nanoholes within a film of OTMS and nanorings of PEG-silane were fabricated as a matrix film to enable spatially selective deposition of APTES. The center-to-center spacing between the nanoholes and ring nanostructures corresponds to the diameter of the surface masks (250 nm) used

as a patterning template for particle lithography. The samples were submerged in solution of APTES (0.02%) in toluene for 3 h to fill in the areas of surface that were not covered with an organosilane matrix film. The areas with APTES present amine groups for further steps of binding Zn phthalocyanines. After removal from the solution of APTES, the samples were sonicated in ethanol and water. The samples with patterns of nanoholes and nanorings were immersed in a dilute solution (10^{-7} M) of ZnPc 1 in pyridine/methanol or in a solution (10^{-5} M) of ZnPc 2 in pyridine/anhydrous toluene to produce Pc nanostructures. Samples were rinsed with methanol and dried under argon. The concentration of ZnPc that was chosen for the immersion step depended on the reactivity of the ZnPcs. Dilute solutions were used to prevent aggregation in solution. Samples were rinsed with methanol and dried under argon. The uncovered areas of substrate that had been masked by spheres provided well-defined surface sites for directing the subsequent attachment of the APTES linker for the growth of phthalocyanine nanostructures.

4.2.8 Characterization of Samples with Scanning Probe Microscopy

Scanning probe characterizations of samples were obtained in ambient conditions with a model 5500 scanning probe microscope (Keysight Technologies, Santa Rosa, CA). Ultrasharp noncontact silicone cantilevers (MikroMasch) with a resonance frequency of 325 kHz and a force constant of 40 N m^{-1} and silicon probes with aluminum reflex coating with an average resonant frequency of 300 kHz and a force constant of 40 N m^{-1} (Budget Sensors) were used for imaging in tapping-mode AFM. Digital images were processed with *Gwyddion* open source software (version 2.47).[174]

4.3 Results and discussion

Surfaces were designed for the spatially selective patterning of zinc phthalocyanines (ZnPcs) to produce multicomponent nanopatterns. The site-selectivity of surfaces was designed

using organosilane nanopatterns for the adsorption of functionalized Zn-Pcs with either a nucleophilic hydroxyl group ZnPc 1 or an electrophilic isothiocyanate, ZnPc 2, as shown in Figure 2. The methods of sample preparation can affect the growth and surface orientation of organosilanes such as OTMS and PEG-silane.[228] The approaches for surface patterning provide new directions for studying surface chemistry at the molecular-level and have practical applications for emerging nanotechnology.

4.3.1 Nanopatterns of OTMS and PEG-silane Prepared using Particle Lithography

Patterns of nanoholes within OTMS prepared with particle lithography are shown in Figure 4.3. The arrangement of nanopatterns span the entire sample, example topography frames reveal the surface organization of the nanoholes. The dark areas indicate the locations where the silica spheres were displaced from the substrate to leave sites of uncovered substrate for depositing APTES. The interface of the OTMS areas between the nanoholes present methyl groups, which have proven to be effective for preventing nonspecific binding in further patterning steps. [218] A view of a broad area of the sample is shown in the topography frame in Figure 4.3A. The circular areas of the nanopatterns are quite uniform in dimension throughout areas of the sample. A map of the surface chemistry is revealed in the simultaneously acquired phase image of Figure 4.3B. The color scale was chosen to indicate the areas of nanoholes as bright spots, showing the locations of uncovered substrate. The high throughput capabilities of particle lithography are evident in Figure 4.3. A view of 260 nanoholes is presented in the magnified topography frame of Figure 4.3C. The surface density of nanoholes is ~10^9 patterns/cm^2 according to the packing of the silica spheres of the surface mask.

A close-up view of an individual nanohole is presented in Figure 4.3D, revealing the detailed circular shape of the patterns. The thickness of the OTMS film is homogeneous even at the edges

of the nanohole. The average depth for the nanoholes measured 1.9 ± 0.3 nm, which is slightly smaller than the theoretical value of 2.5 ± 0.3 nm. The depth and spacing were measured using 50 individual cursor profiles. The measurements indicate a relatively densely packed film, however the matrix layer does not have saturation surface coverage. The width and depth of the nanohole structure is shown with a representative cursor profile (Figure 4.2E), measuring 250 nm wide and approximately 2 nm deep. The distance matches the diameter of the silica spheres used as the surface mask.

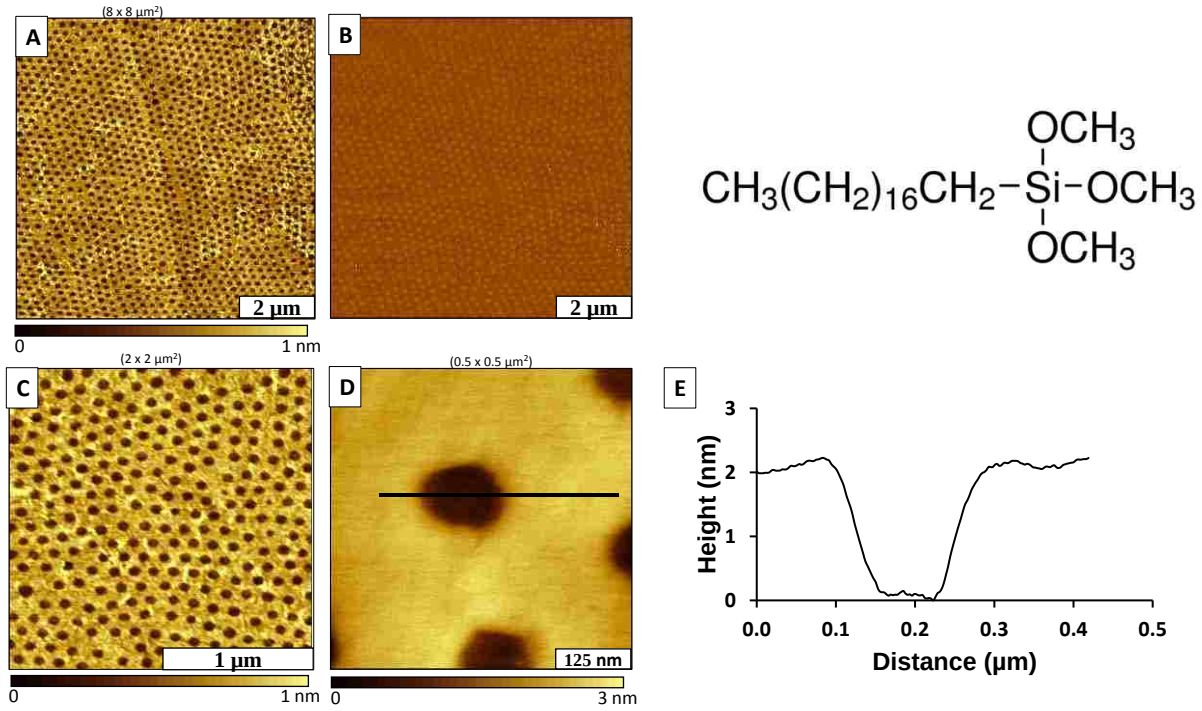

Figure 4.3 Nanoholes within OTMS prepared on Si(111) by particle lithography combined with solution immersion using a surface mask of 250 nm silica spheres. (A) Film of OTS with nanoholes of uncovered substrate shown with an AFM topograph (8 × 8 µm^2); (B) corresponding phase image of A; (C) magnified topography image of the arrangement of nanoholes (2 × 2 µm^2); (D) close-up view of a single nanohole within an OTS film (0.5 × 0.5 µm^2); (E) cursor profile for the line in D.

Particle lithography combined with vapor deposition of PEG-silane was used to produce ring-shaped nanopatterns (Figure 4.4). The ring nanopatterns consist of multilayers of PEG-silane and form at the sites of the water meniscus surrounding the latex spheres of the surface mask. The periodic arrangement and regular shapes of the rings are apparent in the representative topography

frame of Figure 4.4A. Phase images provide information of sample details that are not convoluted by the height scale. The chemistry at the edges of the nanorings have a dark outline in the phase image of Figure 4.4B. The uniformity of the ring shapes, sizes and spacing are apparent in the magnified topography image of Figure 4.4C. There are 19 nanorings that are visible within the 1 × 1 μm^2 area, which scales to ~10^9 patterns/cm^2. A further magnified view is presented in Figure 4.4D for five nanorings. Three height domains are apparent, the center of the rings which are darkest, the areas between the nanopatterns has an intermediate height, and the tallest areas are the rings which have a multilayer of PEG-silane.

The average depth of the multilayer areas of the PEG-silane nanorings measured 3.0 ± 0.3 nm. An example cursor profile is shown in Figure 4.3E. The center-to-center spacing of the nanorings measured 250 nm which matches the diameter of the latex spheres used as the surface mask. The deepest areas within the nanorings are apparent in the cursor plot, where the peaks indicate the areas where there is polymerization of the PEG-silane surrounding the exposed substrate. There is a shorter film of PEG-silane between the nanopatterns. With PEG-silane as a resist layer the further added reagents will no bind nonspecifically to areas surrounding the nanorings. The binding of APTES will be confined to the areas of the exposed substrate within the nanorings. Exquisitely small areas within the PEG-silane nanorings are sites of uncovered substrate that are available for depositing a reactive silane such as APTES as a linker for attaching ZnPcs. Both OTMS and PEG- silane provide suitable resist films for preventing the nonspecific binding in successive protocols of solution immersion to form multicomponent nanostructures.

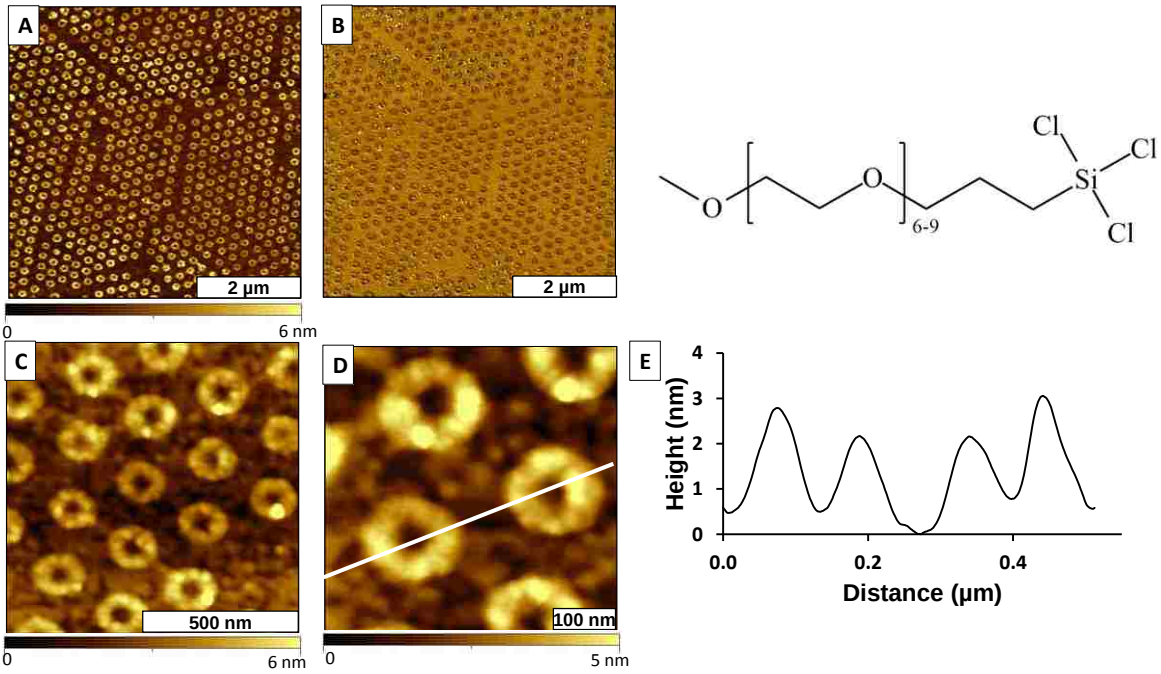

Figure 4.4 Nanorings within PEG-silane on Si(111) prepared by particle lithography combined with a vapor deposition step using 250 nm latex masks. (A) PEG-silane film with nanorings of uncovered substrate shown with an AFM topograph (6 × 6 µm^2); (B) corresponding phase image of A; (C) magnified image (1 × 1 µm^2); (D) magnified image of C (0.5 × 0.5 µm^2); (E) cursor profile for the line in D.

4.3.2 Addition of APTES within Nanopatterns for Binding Phthalocyanines

Amine-terminated APTES was used to form reactive sites to bind ZnPcs for both the OTMS and PEG-silane nanopatterns. After the immersion step for backfilling nanoholes with APTES, scanning probe images were acquired to directly view surface changes (Figure 4.5). The procedure for backfilling the nanoholes and nanorings was accomplished by immersion of the patterned substrates in a dilute solution of APTES (0.02%) in anhydrous toluene. The hexagonal arrangement of APTES nanodots is evident in the example topography frame of Figure 4.5A. The shapes and sizes of the nanodots of APTES is further revealed in the corresponding phase image (Figure 4.5B) The periodicity corresponds to the diameter (250 nm) of the silica spheres that was used as a surface mask. The selectivity for binding of APTES within nanoholes is apparent. A magnified view of 10 nanodots is presented in Figure 4.5C showing the uniformity of the round

shapes at the nanoscale. A further close-up of four nanodots is presented in Figure 4.5D. The tallest areas are located at the very center of the nanodots. The average height of APTES nanodots measured 2.0 ±0.8 nm (*n*=50) above the matrix areas of OTMS. An example line profile across two nanodots is shown in Figure 4.5E. Adding the value for the depth of the OTMS nanoholes from Figure 4.3, the overall thickness of APTES is ~3.0 nm, indicating that a double layer was formed inside the nanorings.

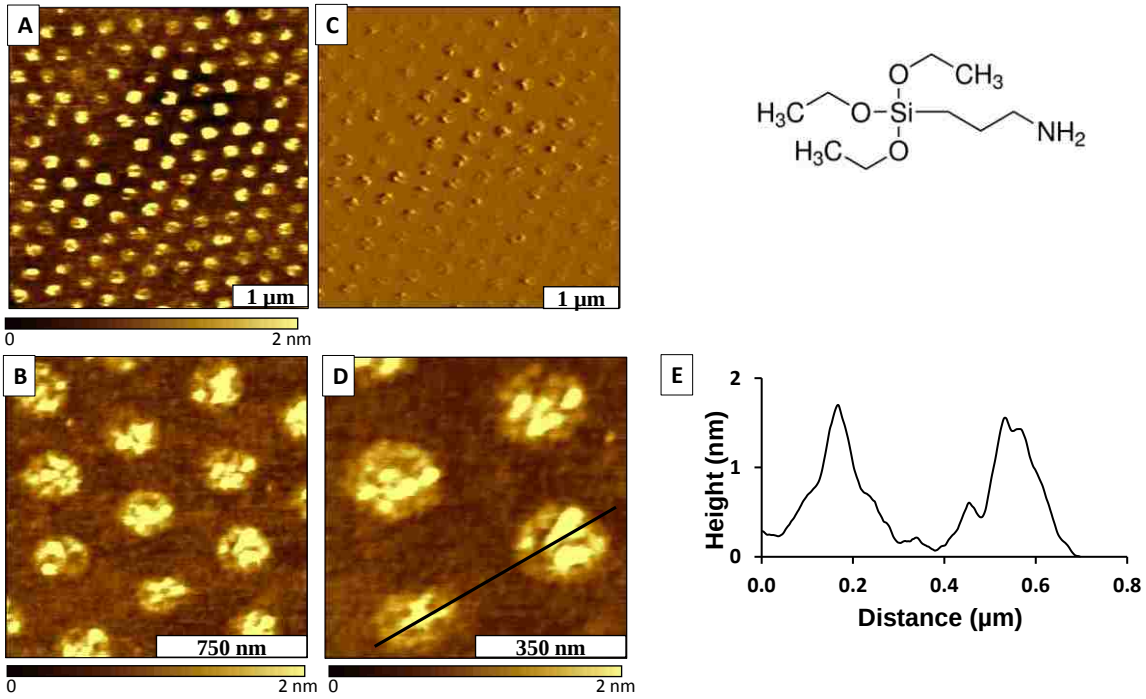

Figure 4.5 Nanoholes within OTMS were backfilled with APTES. (A) Matrix film of OTMS with a periodic arrangement of APTES nanodots viewed with an AFM topograph (4 × 4 µm^2); (B) corresponding phase image for A; (C) Zoom-in topography image (1.5 ×1.5 µm^2); (D) topography frame of four APTES nanopatterns (0.7 × 0.7 µm^2); (E) cursor profile for the line in D.

Example results for backfilling nanorings of PEG-silane with APTES are shown in Figure 4.6 with successive zoom-in views. The high-throughput arrangement of close-packed nanopatterns is revealed in Figure 4.6A. The periodicity and hexagonal packing are further visualized in the corresponding phase image (Figure 4.6B). A magnified view of the APTES filled nanorings is presented in Figure 4.6C. A few areas with bright spots indicate binding of

organosilanes or contaminants, however there is very little nonspecific binding on the PEG-silane resist. A further close-up view of four nanostructures is shown in Figure 6D. In the previous step with PEG-silane nanorings, there was a hole inside the rings (Figure 4.4). After the filling step, the rings are filled with reactive sites for attaching ZnPcs. An example cursor plot is shown for two nanostructures in Figure 4.6E. The average height of APTES nanostructures measured 3.2 ± 0.4 nm (*n*=30) above the PEG-silane matrix, indicating growth of a multilayer of APTES.

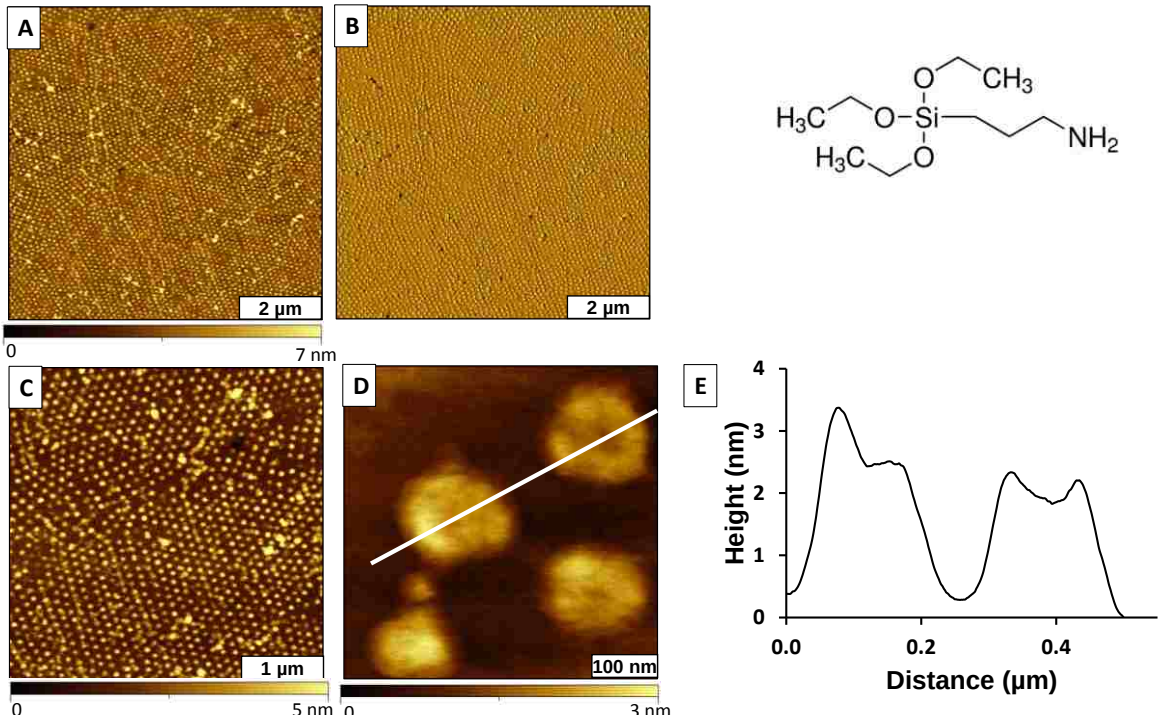

Figure 4.6 Nanopatterns of APTES backfilled into PEG-silane nanorings that were prepared on Si(111). (A) Arrangement of APTES nanopatterns shown with an AFM topograph (8 × 8 µm^2); (B) corresponding phase image; (C) zoom-in topography view (4 ×4 µm^2); (D) close-up topography frame of nanostructures (0.5 × 0.5 µm^2); (E) cursor profile for the line in D.

4.3.3 Spatially Selective Binding of ZnPcs to Sites of APTES Nanodots

The samples containing APTES nanopatterns were treated with a further immersion step to produce ZnPc nanostructures. The solvents that were used for the steps of immersion were chosen according to the solubility of the ZnPcs. The PEG-chain of ZnPc 1 was chosen to increase the solubility of the compound. Successful patterning of ZnPcs was accomplished with both resists,

results with OTMS are shown in Figure 4.7 and the PEG-silane sample is presented in Figure 4.8. A boundary area of uncovered substrate is apparent in the upper right corner of Figure 4.7A. Broad areas of densely packed nanostructures are visible for an area spanning microns. The surface chemistry of the patterns have a dark contrast compared to the surrounding matrix film of OTMS in the phase image of Figure 4.7B because the ZnPcs nanostructures have a different elastic response than the surrounding resist layer. With greater magnification the shapes of the patterns can be resolved in Figure 4.7C. The shapes of the nanostructures are less round than in the previous steps with APTES after binding ZnPc. A close-up view of 12 nanostructures is presented in Figure 4.7D.The tallest areas are located at the very center of the patterns where ZnPc 1 attached to the APTES patterns. The nanopatterns are slightly wider, however the distinct shapes of nanostructures persisted without nonspecific binding on the matrix areas of OTMS patterns.

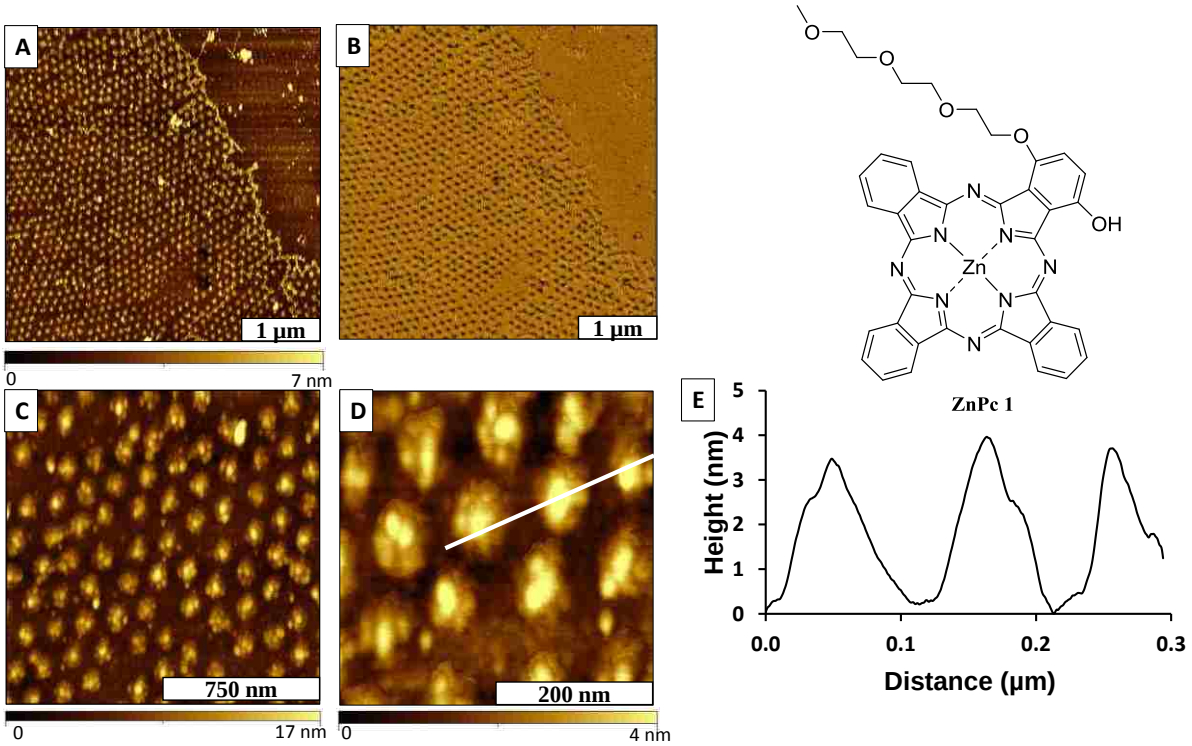

Figure 4.7 Growth of ZnPc 1 on APTES nanopatterns within an OTMS resist. (A) View of nanostructures after immersion in ZnPc 1, topograph (8 × 8 µm^2); (B) corresponding phase image; (C) magnified topography image (4 × 4 µm^2); (D) Close-up view (1 × 1 µm^2); (E) cursor profile for the line in D.

The height of the nanopatterns has increased after binding ZnPc 1 as evidenced in the cursor profile (Figure 4.7E). The average height above the OTMS matrix film for ZnPc 1 nanostructures measured 3.3 ±0.7 nm (*n*=50) which is an increase of 1.3 nm from the height of APTES nanodots. The height change corresponds to an upright configuration with a tilted orientation. The increase in thickness would be ~0.5 nm for a co-planar arrangement.

Growth of ZnPc 1 was also accomplished on APTES nanostructures prepared within PEG-silane nanorings (Figure 4.8). The arrangement of ZnPc 1 nanostructures is shown in the topography frame of Figure 4.8A. The circular shapes and heights of the nanostructures are quite uniform over broad micron-size areas. There is little nonspecific adsorption on the matrix areas of PEG-silane located in between the nanostructures, shown in the phase image of Figure 4.8B. A close-up view of 40 nanostructures is presented in the topography frame of Figure 4.8C. The shapes and heights of the ZnPc 1 nanostructures are quite uniform at the nanoscale. The regular sizes are apparent in the high magnification topography frame of Figure 4.8D. The average height measured 4.3 ± 0.5 nm (*n*=30) which corresponds to an increase of the height of APTES nanopatterns of ~1.1 nm. This matches closely with the value for adsorption within an OTMS matrix film.

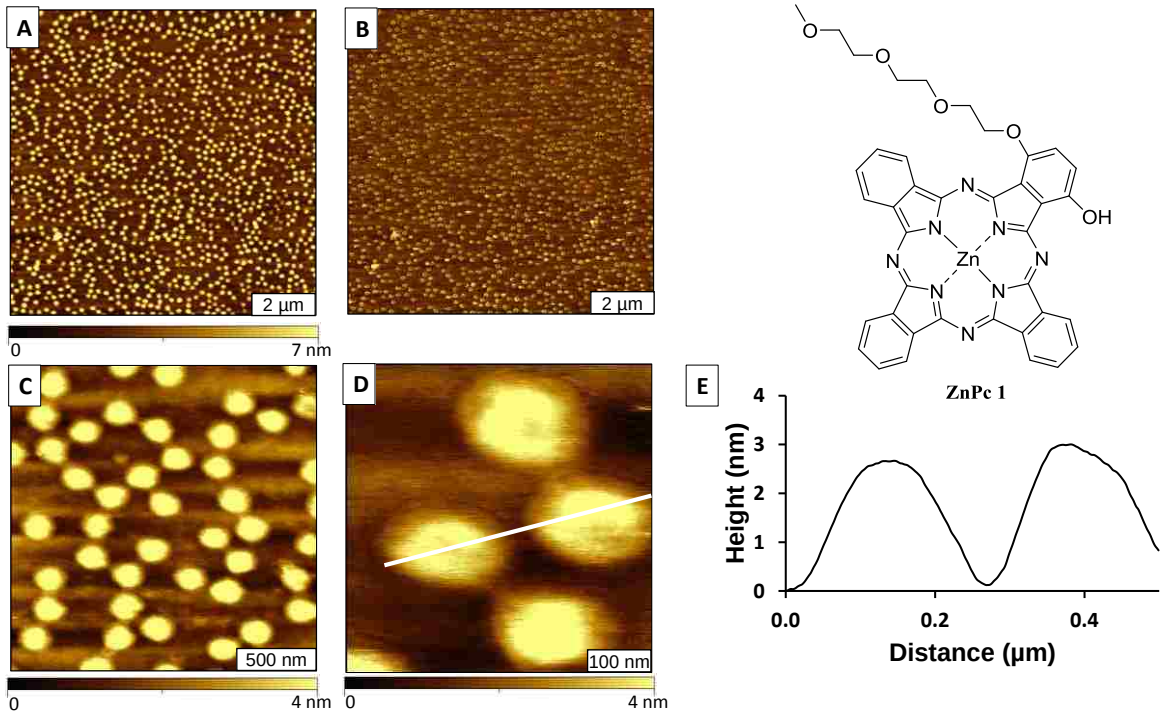

Figure 4.8 Growth of nanostructures of ZnPc 1 on APTES nanodots within a PEG-silane matrix film. (A) Wide area topography frame (10 × 10 µm^2); (B) simultaneously acquired phase image; (C) magnified topography view (2 × 2 µm^2); (D) close-up of 4 nanostructures (0.5 × 0.5 µm^2); (E) cursor profile for the line in D.

The self-assembly and growth of ZnPc 2 was evaluated for a sample prepared with APTES nanostructures within an OTMS matrix film (Figure 4.9). A view of a relatively broad area of the surface reveals the organization of ZnPc 2 nanostructures in the topography frame of Figure 4.9A.The hexagonal arrangement of nanostructures is also apparent in the phase image of Figure 4.9B, showing a map of the difference in surface chemistry between the matrix and nanostructures. A close-up view of 11 nanostructures is presented in the topography frame of Figure 4.9C. The shapes and sizes are not as uniform for the heterostructures of APTES and ZnPc 2 as viewed in the high magnification topography frame of Figure 4.9D. However, the matrix areas of OTMS are mostly free of adsorbates and contaminants. The height of the ZnPc 2 nanostructures in Figure 4.9D range in height from 15-17 nm, as shown with an example cursor profile in Figure 4.9C.

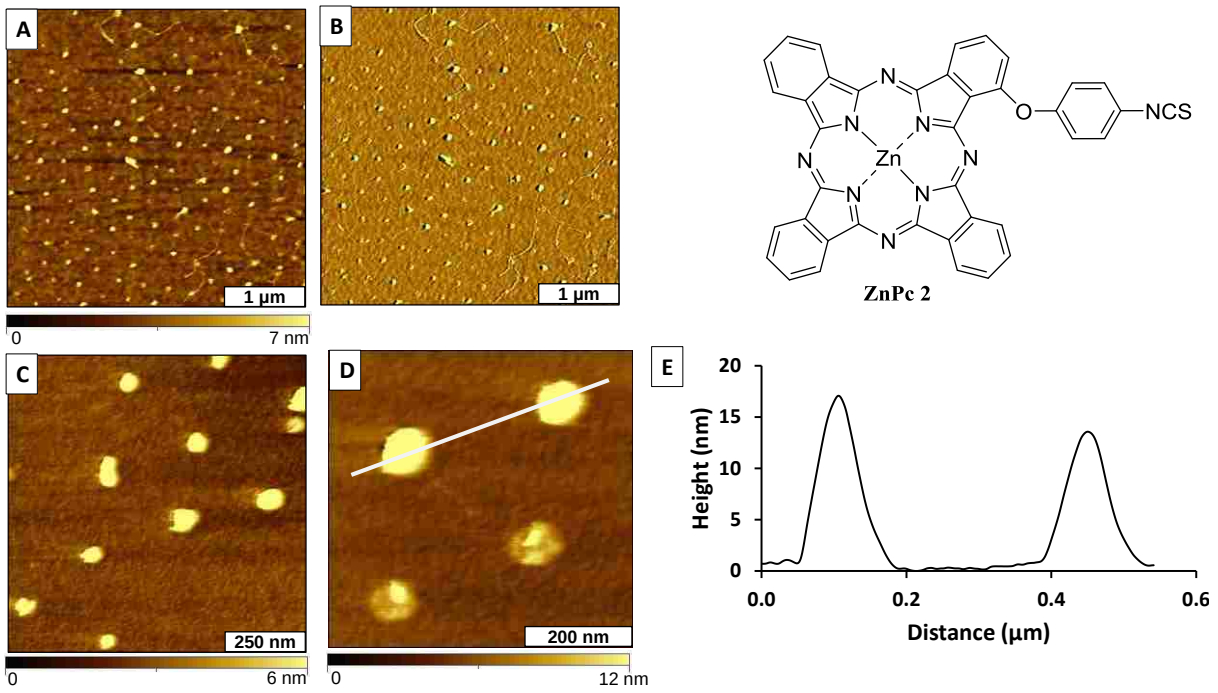

Figure 4.9 Nanoclusters of ZnPc 2 on APTES (a) ZnPc 2 shown with an AFM topograph (4 × 4 μm^2); (b) corresponding phase image; (c) magnified image (1 × 1 μm^2) ; (d) close-up view (0.6 × 0.6 μm^2) (e) cursor profile for the line in d.

A comparison of the height increases after binding ZnPcs to APTES nanopatterns is presented in Figure 4.10. The data was derived by subtracting the average value of the heights of APTES nanodots, so the values are an approximation obtained from multiple cursor measurements (n=50). The average change in height after binding ZnPc 1 was 1.3 ± 0.7 nm. The change measured for the average height after binding ZnPc 2 was 6.3 ± 4 nm.

The dimensions of ZnPc 1 and ZnPc 2 are comparable, therefore the height of the nanopatterns depends mostly on the orientation of the ZnPcs. The size differences suggest that the affinity of ZnPc 1 and ZnPc 2 for binding to the sites of APTES nanodots is not similar, attributable to the chemistry of the substituents. The increase in height indicate that a single molecular layer of ZnPc was bound to the APTES nanodots, however the orientation of the molecules is not the same depending on the structure of the substituents.

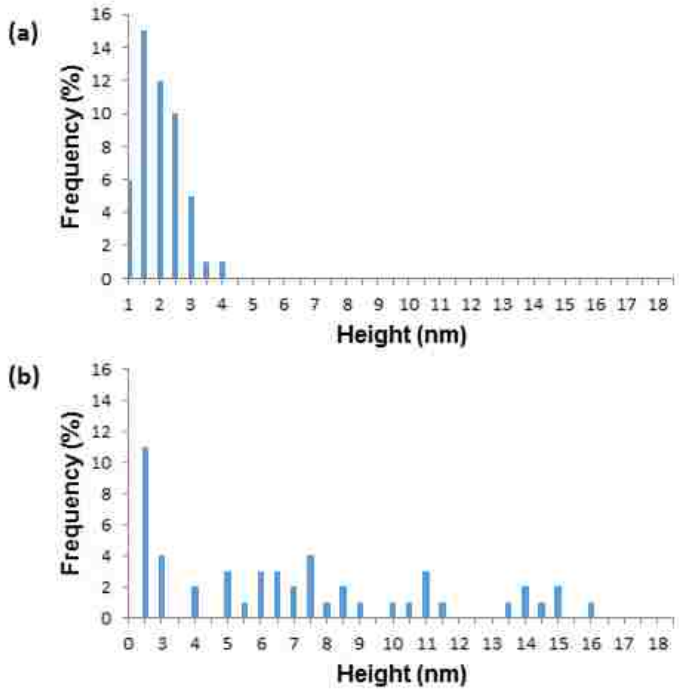

Figure 4.10 Size distribution for the measured height increase of APTES nanodots after binding (a) ZnPc 1 and (b) ZnPc 2.

The amine-terminated groups present at the interface of the APTES nanodots are available to react with the functional groups presented on the ZnPcs. The hydroxyl group of ZnPc 1 does not form a covalent bond with the APTES linker, however electrostatic interactions can lead to binding with the phthalocyanine macrocycle with a coplanar configuration. The NCS isothiocyanate group on ZnPc 2 reacts with the amine present on APTES to produce a covalent thiourea linkage. The height measured after binding ZnPc 2 to APTES nanodots corresponds roughly to an upright conformation, with a slightly tilted arrangement. Both methyl-terminated OTMS and PEG-silane proved to be effective as resist layers, without apparent areas of non-specific binding of ZnPcs or APTES on matrix areas surrounding the nanopatterns. For the selected ZnPcs, the nature of the substituents determined whether the molecules assembled in a side-on orientation or in a coplanar arrangement with the substrate.

4.4 Conclusions

Nanostructures prepared using particle lithography provide a practical approach to obtain information of chemical reactions on surfaces. Molecular-level investigations of the morphology, self-assembly processes, and properties of designed nanostructures of organosilanes and ZnPcs were accomplished using protocols of particle lithography. Both OTMS and PEG-silane proved to be effective as resists to enable site-selective binding of ZnPcs on APTES nanopatterns. Well-defined surfaces with desired functionalities can be achieved with protocols of particle lithography. Nanoholes and nanorings of organosilanes were prepared with highly reproducible sizes, shapes and periodicity for further steps of chemical reactions. Molecules of Zn-Pcs that were functionalized with either a hydroxyl or an isothiocyanate group were successfully patterned onto reactive sites of APTES without apparent nonspecific adsorption on matrix areas of OTMS and PEG-silane. The changes in surface chemistry were visualized with great detail after each key step of the nanopatterning protocols, enabling measurement of nanometer scale changes of the thickness of molecular layers.

CHAPTER 5. PATTERNS OF GOLD NANOPARTICLES PREPARED USING PARTICLE LITHOGRAPHY

5.1 Introduction

Particle lithography has enabled surface-based chemical reactions at the molecular level providing highly reproducible and practical approaches for the fabrication of nanopatterns from organosilane and organothiol SAMs.[91, 229] The nature of SAMs provide advantages for designing the chemistry of surfaces with desired carbon chain lengths and functional groups. Using OTMS and PEG-silane as a resist, nanopatterns were prepared on a glass surface using particle lithography combined with steps of either vapor deposition or immersion in solutions. Surface morphologies of nanorings and nanoholes were produced using basic steps of particle lithography. The morphology and selectivity of designed surfaces of SAMs formed with OTS, OTMS, and PEG-silane using steps of particle lithography have were evaluated using high resolution AFM. Thickness measurements from AFM cursor profiles were used to determine the orientation and density of OTS, OTMS, and PEG-silane nanostructures.

Surfaces can be designed with methyl-terminated organosilane nanopatterns to furnish a resist to create multicomponent nanostructures using further chemical steps. Uniform patterns of nanoholes prepared within a film of OTMS were prepared using particle lithography combined with a vapor deposition step. Exposed areas of the substrate that were protected by the mesosphere mask furnish sites for selectively binding gold nanoparticles, whereas areas with methyl-terminated organosilane provide an effective resist to prevent nonspecific attachment of nanomaterial. Surface changes throughout the steps of particle lithography were investigated *ex situ* using tapping-mode AFM. Particle lithography is used to pattern a substrate by placing a surface mask of monodisperse latex or silica spheres to direct the deposition of inorganic and organic materials.[26, 50, 213] Preparation of exquisitely small, regular nanostructures have been

accomplished with a few basic chemistry steps. The samples reveal relatively few defects at the nanoscale, and highly reproducible for patterning over relatively large areas of tens of microns.[10]

Periodic arrays of organosilane nanostructures prepared with particle lithography provide a foundation to spatially define sites for adsorption of nanoparticles. Advantages of particle lithography include relatively low cost, the use of basic lab equipment and experimental steps, and the capability for tuning the dimensions of surface structures according to the diameters of spheres. The nanopatterns of SAMs must provide selectivity for binding organic molecules, metals, and other nanomaterials. Solutions of monodisperse spheres spontaneously assemble into close-packed arrangements on surfaces during the evaporation of solvents. Self-assembled monolayers provide model surfaces for fundamental studies of interfacial chemistry and self-organization due to the flexible chemistry of functional head groups. Self-assembled monolayers of organosilanes attach to the interstitial sites between the spheres by covalent bonding at areas where nanoscopic residues of water are present. The film thickness and molecular density of SAMs depends on the chemical nature of the surface, the type of organosilane, adsorption time, amount of water, temperature, and choice of immersion solutions.[40]

A procedure for preparing arrays of gold nanoparticles prepared within resists of organosilane nanopatterns was developed with particle lithography for glass and quartz substrates. Surfaces can be fabricated with methyl-terminated organosilane nanopatterns to provide a resist for further chemical steps. Exposed areas of the substrate provide sites for selectively binding functionalized nanoparticles, whereas areas with methyl- or chloro- terminated organosilane provide an effective resist to prevent nonspecific adsorption. Thus far, particle lithography and organosilane chemistry were used successfully to prepare nanoholes within a thin film of OTMS. The steps of sample preparation of the surface platform were characterized with AFM. The

capability of AFM for achieving nanoscale resolution enables characterization of material properties, as well as fundamental investigations of chemical reactions.

5.2 Experimental Details

5.2.1 Materials and Reagents

Glass microscope coverslips were obtained from Fisher Scientific (Hampton, NH). Concentrated sulfuric acid (98.0%) (J.T. Baker Hampton, NH) and hydrogen peroxide (30%) (British Drug Houses, VWR) were used as received from Sigma-Aldrich. Size-sorted monodisperse silicon spheres (1 wt.% solution) with sulfate surface groups with a particle diameter 200, 300, and 500 nm were obtained from Thermo Scientific (Fremont, CA) and used as surface masks during vapor deposition of organosilanes. Octadecyltrimethoxysilane and 2-[methoxy (polyethyleneoxy)propyl]trichlorosilane (PEG-silane) were purchased from Gelest (Morrisville, PA) and used without further purification. Ethanol was purchased from Deacon Labs (Prussia, PA) and was used a received. Anhydrous toluene was purchased from Merck Millipore (Billerica, MA) and was used as received.

5.2.2 Substrate Preparation

Glass and Si (111) substrates were cleaned by soaking in piranha solution (3:1 v/v ratio of concentrated sulfuric acid and 30% hydrogen peroxide) for 1 h. Piranha solution is corrosive and should be handled with caution. After cleaning, surfaces were rinsed with copious amounts of deionized water purified by a Millipore Milli-Q purification system (18 MΩ cm, Boston, MA) and dried in air.

5.2.3 Synthesis of Gold Nanoparticles

A solution of trisodium citrate (40 mM) was freshly made by dissolving 0.113 g of the solid into 10 mL of deionized water. A 0.25 mM gold solution was made by dissolving $HAuCl_4 \cdot 3H_2O$ in 25 mL of deionized water. An aliquot of 10 mL of the gold solution was refluxed at 300°C for approximately 10 min before adding 500 µL of the trisodium citrate solution. After 10 min, the solution was removed from heat and stirred at room temp for approximately 30 min yielding gold nanoparticles with a particle size of approximately 5 nm.

5.2.4 Synthesis of MPTMS Coated Gold Nanoparticles

Nanoparticles coated with MPTMS were synthesized as previously reported.[230] A 0.35 mM solution of tetraoctylammonium bromide was freshly made by dissolving 0.547 g into 10 mL of toluene. A 15mM gold solution was made by dissolving 0.015 mL of $HAuCl_4 \cdot 3H_2O$ in 10 mL of water. After combining the solutions, the organic phase was isolate and 0.065 g of MPTMS was added to the layer. The solution was further stirred for 10 minutes in ambient conditions and the colorless phase was isolated. 10 mL of a 150mM $NaBH_4$ solution was added to the color phase slowly to yield the MPTMS coated Au nanoparticles. After stirring at room temperature for approximately 45 min, the dark layer containing the nanoparticles was removed.

5.2.5 Nanofabrication of Nanoholes with a Matrix of OTMS

A drop of latex spheres (diameter 200 nm) was deposited onto clean glass substrates and dried in ambient conditions. Next the samples were placed on a platform within a sealed reaction vial containing 400 µL of neat OTMS. To generate a vapor the reaction vessel was placed into an oven at 70ºC for approximately 12 h. After cooling samples were rinsed with water and sonicated in toluene, ethanol, and water in 30 min increments to fully remove the mask of latex spheres.

5.2.6 Preparation of Nanodots of MPTMS for Binding Gold Nanoparticles

The samples containing OTMS nanoholes were placed into a 0.1% solution of MPTMS in anhydrous toluene to enable growth of nanodots for binding Au nanoparticles. The samples were placed in solution for 5 h and then removed and sonicated in ethanol, chloroform, and water to clean the surfaces.

5.2.7 Nanofabrication of Nanoholes of MPTMS within a PEG-silane Matrix Film

The samples with a surface mask of latex spheres on glass were placed on a platform within a sealed reaction vial containing 400 µl of neat MPTMS. To generate a vapor for deposition onto the glass substrate to produce a thin film of MPTMS. The reaction vial was placed into an oven at 70°C. After 4 h, the samples were rinsed and sonicated in ethanol for approximately 30 min and dried under argon gas. An aliquot of 400 µL of an aqueous suspension of monodisperse 200 nm silica spheres (200 nm diameter) were cleaned using successive steps of rinsing and sonication. The solution of silica spheres was centrifuged four times (10 min each cycle) at 20,000 rpm. The liquid portion was carefully decanted and the solid pellet was resuspended in 1 mL of deionized water by vortex mixing. The solid pellet of the final centrifugation step was resuspended in 400 µL of deionized water. To prepare a surface mask, 10 µl of the spheres were deposited on the MPTMS/glass sample and dried at 4°C for 16 h. The samples were then treated with UV–ozone for 20 min to oxidize areas exposed in the interstitial sites of the spheres. Immediately after UV–ozone treatment, the samples were immersed in a 1% (v/v) solution of PEG-silane in anhydrous toluene for 5 h. The areas surrounding the spheres were backfilled with PEG-silane to form a resist layer to enable nanopatterning with further chemical steps. The samples were rinsed with water and sonicated in ethanol for approximately 30 min to remove the silica spheres.

5.2.8 Time Study of the Immersion of Samples in Solutions of Nanoparticles

Glass substrates prepared with MPTMS filled nanoholes within PEG-silane were immersed in gold nanoparticle solutions for selected time periods to determine the best parameters for nanopatterning. Substrates containing the OTMS nanoholes were immersed into the MPTMS coated gold nanoparticle solution. The samples were immersed for intervals ranging from 12 h to 2 weeks.

5.2.9 AFM Characterization of Nanopatterns

Scanning probe characterizations of samples were obtained in ambient conditions with a model 5500 scanning probe microscope (Keysight Technologies, Santa Rosa, CA). Non-contact tapping-mode silicone cantilevers ATEC-NC-SPL (Nanosensors) with a resonance frequency range of 210-490 kHz and a force constant range of 12-110 N m^{-1} and silicon probes with aluminum reflex coating with an average resonant frequency of 300 kHz and a force constant of 40 N m^{-1} (Budget Sensors) were used for imaging in tapping-mode AFM. Digital images were processed with *Gwyddion* open source software (version 2.47).[174]

5.3 Results and Discussion

5.3.1 Preparations of Glass Surfaces with OTMS and MPTMS Nanopatterns

Controlling the humidity in the environment is a critical step in the self-assembly process for organosilane SAMs. During the drying time of latex films, a water meniscus forms at the base of each latex sphere on the surface, which will define the reaction sites for hydrolysis and condensation of the organosilanes. The mask of spheres can be removed by rinsing with solvents and sonication after vapor deposition is complete to produce a periodic array of nanoholes within an organosilane matrix. The arrangement of nanopatterns span the entire sample, example topography frames reveal the surface organization of the nanoholes. Within the representative

topography frame in Figure 5.1, the dark areas indicate the locations where the surface mask of latex spheres were displaced from the substrate to leave sites of uncovered glass substrate. The interface of the OTMS areas between the nanoholes present methyl groups at the interface, which have proven to be effective for preventing nonspecific binding in further patterning steps. The measured distance between nanoholes matches the diameter of the latex spheres used as a surface mask. A broad area of the sample is shown in the topography frame in Figure 5.1A. The circular areas of the nanopatterns are uniform in dimension throughout the sample. A map of the surface chemistry is revealed in the simultaneously acquired phase image of Figure 5.1B. The color scale was chosen to indicate the areas of nanoholes as bright spots, showing the locations of uncovered substrate. The high throughput capabilities of particle lithography are evident, there are 152 nanoholes within the frame, which scales to ~10^9 nanopatterns μm^{-1}. The thickness of the OTMS film measures 1.2 ± 0.5 nm, referencing the bare areas of substrate within the nanoholes as a baseline.

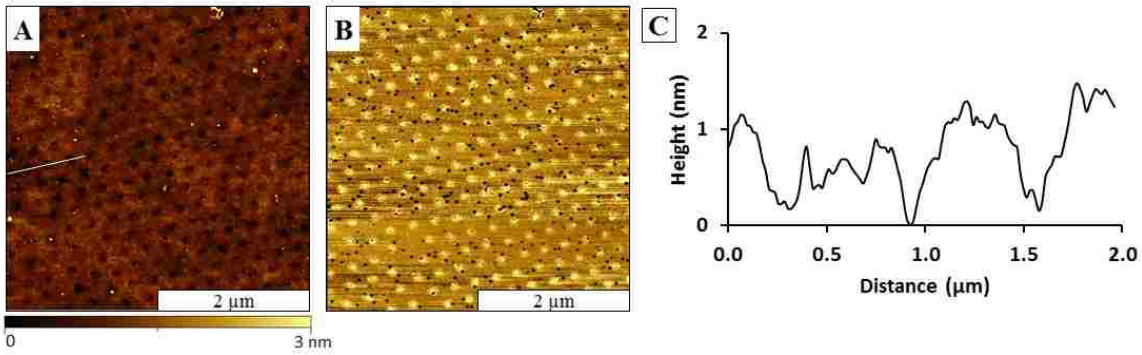

Figure 5.1 Nanoholes within OTMS prepared with vapor deposition. Images were acquired in air using tapping-mode AFM. (A) topography (8× 8 μm^2) and (B) corresponding phase image; (C) Cursor profile for the line in A.

Addition of selected organosilanes to the areas within the nanoholes (backfilling), changes the nature of the surface to impart selectivity for attaching further molecules or nanomaterials. A foundation of spatially defined sites for adsorption of nanoparticles was prepared with particle lithography to form periodic arrays of organosilane nanostructures. The procedure for backfilling the nanoholes is an immersion step. By immersing patterned substrates into a 1% solution of toluene and 3-mercaptopropyl-trimethoxysilane (MPTMS), nanodots with uniform geometry and periodic spacing were formed on surfaces of glass (Figure 5.2). Nanoholes of OTMS were successfully backfilled with MPTMS to define areas with selectivity for the next step of nanoparticle deposition. The brighter areas in the topography images indicate sites where there was growth of MPTMS, whereas the darker areas represent the surrounding areas of the OTMS resist.

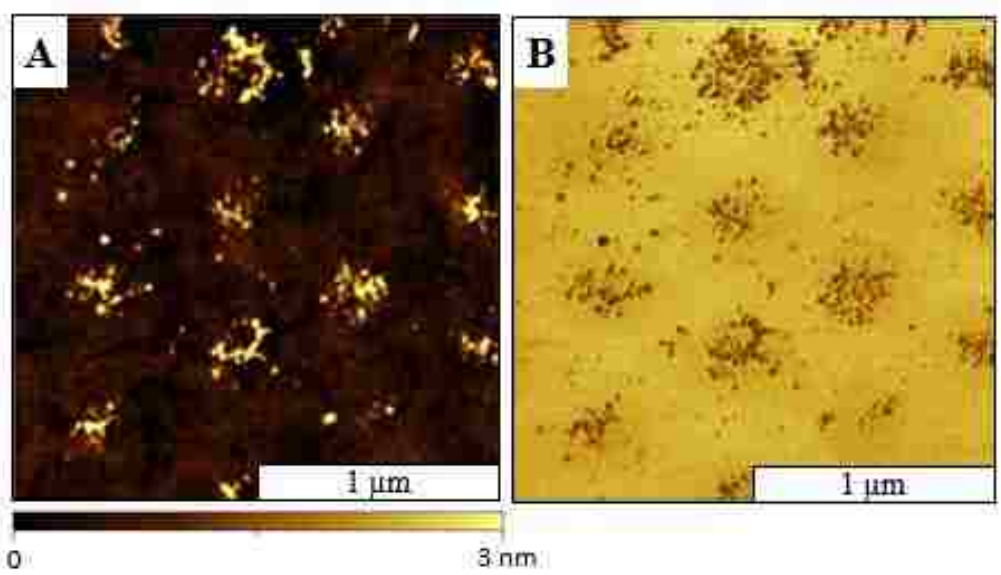

Figure 5.2 Nanoholes of OTMS backfilled with MPTMS imaged with tapping-mode AFM. (A) Topography (2× 2 μm^2) and (B) corresponding phase image.

Sulfur-terminated MPTMS was used to form reactive sites to bind the gold nanoparticles to the OTMS nanopatterns. After the immersion step for backfilling nanoholes with MPTMS,

scanning probe images were acquired to directly view surface changes (Figure 5.2). The procedure for backfilling the nanoholes and nanorings was accomplished by immersion of the patterned substrates in a dilute solution of MPTMS (0.1%) in anhydrous toluene. The glass substrate containing the nanoholes was immersed into a dilute solution of MPTMS. A hexagonal arrangement of the nanoholes backfilled with MPTMS is shown in the zoom-in frame (2×2 μm^2) of Figure 5.2A. The nanoholes were formed according to the arrangement of the packing of the surface mask of spheres. There is a small amount of nonspecific binding of MPTMS between the nanopatterns, however most of the adsorption occurred within the exposed sites of the nanoholes, as revealed in the corresponding phase image of Figure 5.2B. The spacing between the nanopatterns measured 500 ± 0.1 nm. The MPTMS was successfully patterned within the exposed sites of the substrate.

5.3.2 AFM Characterization of MPTMS Nanostructures that were Prepared using Vapor Deposition and Immersion

To determine which parameters worked best for depositing the gold nanoparticles the method shown in Figure 5.3 was done with sample prepares using protocols of particle lithography. The self-reactive properties of hydroxyl groups can be problematic due to cross reacting to form mixed surface multilayers when using PEG-silane as a resist.[229] A compositionally patterned glass surface of MPTMS nanostructures was prepared using PEG-silane as a resist to provide sites for the selective attachment of gold nanoparticles. Nanoholes of MPTMS were successfully produced using steps of vapor deposition and immersion shown in Figure 5.3. The three key steps for the deposition of gold nanoparticles with particle lithography were to prepare surface film of MPTMS with vapor deposition; depositing as mask of silica spheres on the MPTMS film; and treating the sample with UV–ozone. After rinsing away the mask of silica spheres, the areas beneath the silica spheres that were protected provide reactive sites for attaching gold nanoparticles.

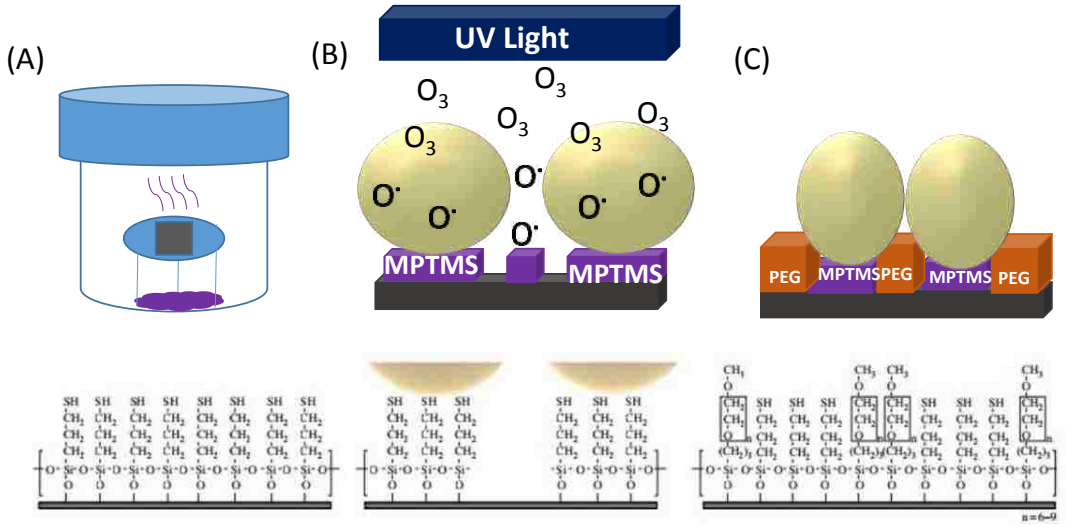

Figure 5.3 Steps for preparing the surface for the deposition of gold nanoparticles with particle lithography. (A) A surface film of MPTMS was prepared by vapor deposition on glass substrates; (B) after coating the MPTMS surface with a mask of silica spheres, the samples were treated with UV – ozone. (C) Samples were immersed in a PEG-silane solution and cleaned to eventually fill the exposed surface sites with gold nanoparticles.

Surface changes after completing the steps shown in Figure 5.3 can be characterized *ex situ* using AFM. An example experiment is shown in Figure 5.4 revealing nanopatterns of MPTMS within a PEG-silane matrix. The 8 × 8 μm^2 topography image (Figure 5.4A) was acquired with tapping-mode in ambient conditions. The dark areas indicate the sites of the nanopatterns, whereas the brighter areas indicate the surrounding matrix film of PEG-silane. The arrangement of nanopatterns is disclosed in the simultaneously acquired phase image in Figure 5.4B. The nanopatterns measure 1.2 ± 0.2 nm in depth, as shown in the example line profile of Figure 5.4C. The nanopatterns contain MPTMS as spatially selective sites for depositing nanopatterns. The matrix areas surrounding the nanopatterns present hydroxyl groups at the interface to resist the attachment of nanoparticles.

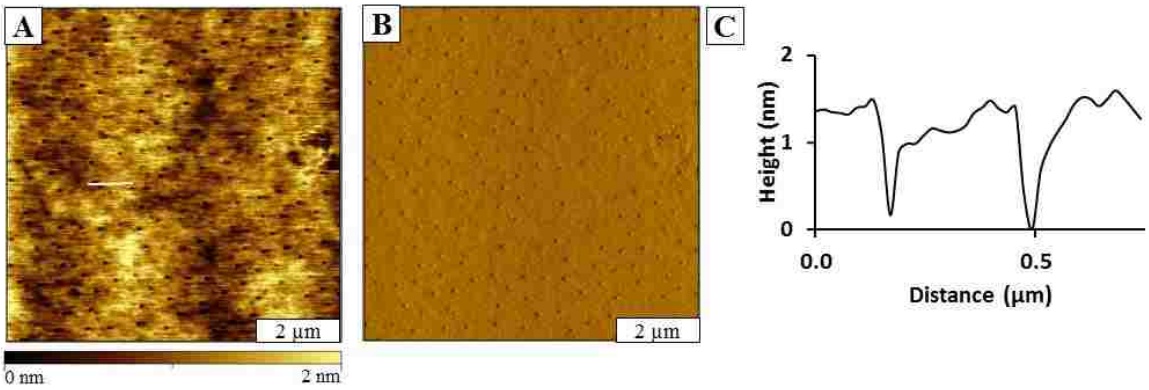

Figure 5.4 Nanoholes within a film of MPTMS produced by steps of vapor deposition and immersion imaged with tapping-mode AFM. (A) Topography (8×8 μm^2), (B) corresponding phase image, (C) height profile for the white line in A.

5.3.3 Patterning Gold Nanoparticles on MPTMS Nanopatterns

To determine the best parameters for patterning of the gold nanoparticles, experiments were conducted to evaluate selected intervals for the immersion time. The substrates containing nanoholes of MPTMS were immersed into individual vials of concentrated solutions of the gold nanoparticles for 24 h, 48 h, 72 h and 2 weeks in ambient conditions. The gold nanoparticles should bind to the thiol group of the MPTMS sites through chemisorption. The resist layer of PEG-silane should prevent nonspecific adsorption on areas surrounding the MPTMS nanopatterns. After the selected time of immersion, the samples were removed from solution, rinsed with ethanol, and dried with argon. Example experiments are shown in Figure 5.5. After 24 h of immersion in the Au nanoparticle solution the Au nanoparticles were not evident on the surface, as shown in Figure 5.5A. There are three distinct regions of contrast revealed in the corresponding phase image of Figure 5.5B. The darkest circular areas are the sites of MPTMS, the brightest areas are the rings surrounding the MPTMS nanopatterns, and the intermediate color indicates the surrounding matrix

film of PET-silane. Nanoparticles were not evident in either topography or phase images after 24 h immersion.

The sample that was immersed for 48 h is shown in Figures 5.5C and 5.5C. Gold nanoparticles are evident throughout the sample, however the arrangement of the nanopatterns does not follow the periodicity of the MPTMS nanopatterns. A rectangular shape is observed due to the blunt shape of the AFM tip. The convolution of tip geometry and sample is apparent, so that the shape observed indicates the profile of the AFM probe rather than the size and shape of the nanoparticles. The substrate that was immersed for 72 h showed no evidence of the patterning of nanoparticles, as revealed in Figures 5.5E and 5.5F.

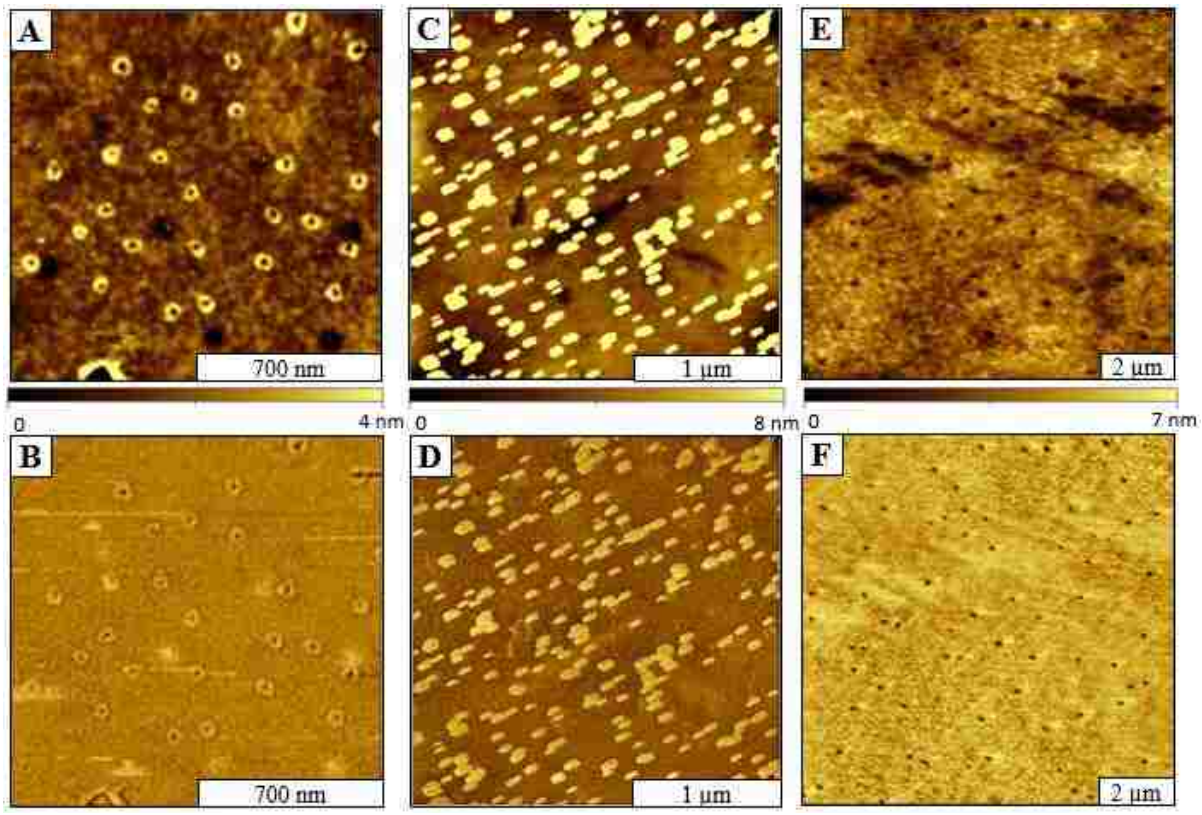

Figure 5.5 Immersion of nanopatterned samples in solutions of nanoparticles for time intervals ranging from 24- 72 h. (A) 24 h immersion topography (1.4 × 1.4 μm^2), (B) corresponding phase image of A, (C) 48 h immersion topography (2.5 × 2.5 μm^2), (D) corresponding phase image of C, (E) 72 h immersion topography (10 × 10 μm^2), (F) corresponding phase image of E.

The attachment of gold nanoparticles to the thiol groups of MPTMS nanopatterns was investigated for a sample that was immersed for two weeks as shown with an example topography image in Figure 5.6. There are approximately 30 areas of MPTMS nanopatterns with the topography frame in Figure 5.6A. The regions of the matrix film surrounding the nanopatterns contain characteristic features of a film of PEG-silane exhibiting homogeneous surface coverage. The sizes and shapes of the nanopatterns are relatively uniform at the nanoscale, with diameters measuring 500 ± 0.2 nm. The arrangement and shapes of the MPTMS nanopatterns is further disclosed in the phase image (Figure 5.6B). It is clear from the topography and phase images that nanoparticles did not bind to the sample. The depth of the nanopattern measure 3.4 ± 0.2 nm, indicated with a representative cursor profile across 3 nanopatterns in Figure 5.6C.

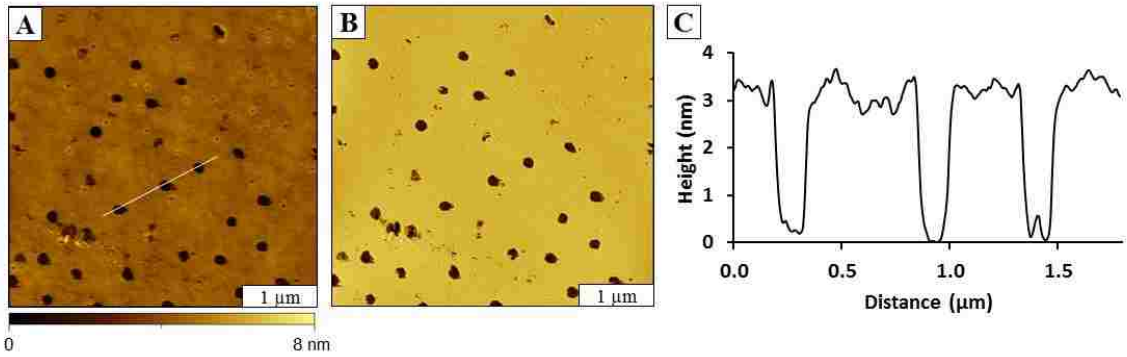

Figure 5.6 Results for a sample prepared after 2 weeks of immersion of a substrate containing MPTMS within nanoholes into a solution with gold nanoparticles. (A) Topography image (4 × 4 μm^2) acquired in air with tapping-mode AFM; (B) corresponding phase image; (C) Cursor profile for the line in A.

A sample containing MPTMS in PEG-silane nanoholes was immersed for 33 h as shown in Figure 5.7. The arrangement and spacing of MPTMS nanopatterns is apparent, and it is clear that nanoparticles are not present on the surface in the topography frame of Figure 5.7B. The circular geometry and ring shapes of the MPTMS nanopatterns are further revealed in the phase image of Figure 5.7B. Measurements of the depth of the nanopatterns are not accurate this

magnification, however the periodicity of the patterns measured 500 ± 0.3 nm, as shown with a representative cursor profile across 3 nanopatterns in Figure 5.7C.

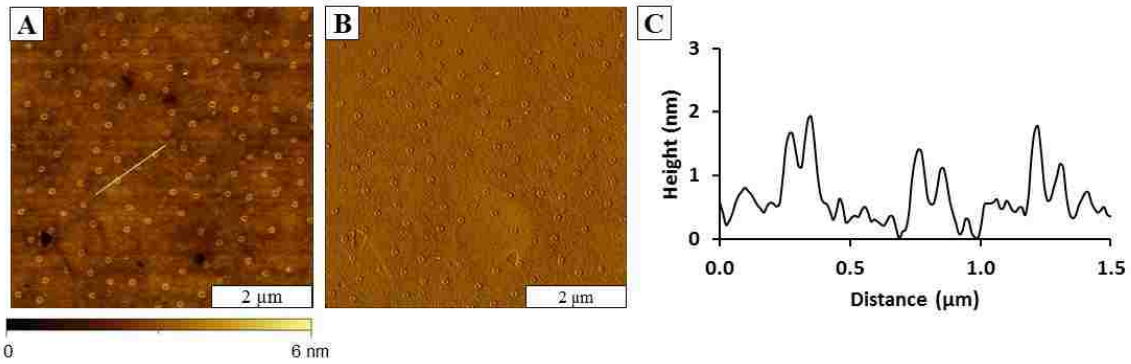

Figure 5.7 After immersion of a sample containing MPTMS in PEG-silane nanopatterns into a solution of gold nanoparticles for 33 h. (A) topography (6 × 6 μm^2) and (B) corresponding phase image; (C) Cursor profile for the line in A.

5.3.4 Deposition of MPTMS Coated Gold Nanoparticles onto Patterned Glass Substrates

To promote the binding of nanoparticles to the MPTMS functional groups, another method was evaluated using nanoparticles coated with organosilanes. In this study the nanoparticle was coated with MPTMS to bind to glass substrates.[230] The procedure for particle lithography can be done with three steps: self-assembly of a resist layer, rinsing to remove the surface mask, and patterning of the nanoparticles which is shown in Figure 5.8.

The Au nanoparticles were coated with MPTMS to direct the nanostructures to the nanopatterns. The thiol group present on MPTMS should bind to the Au nanoparticle to promote coating of the nanoparticles. The silane groups present on the terminal end of the organosilane that coats the Au nanoparticle will direct the nanoparticle to bind within the nanoholes present within the OTMS matrix.

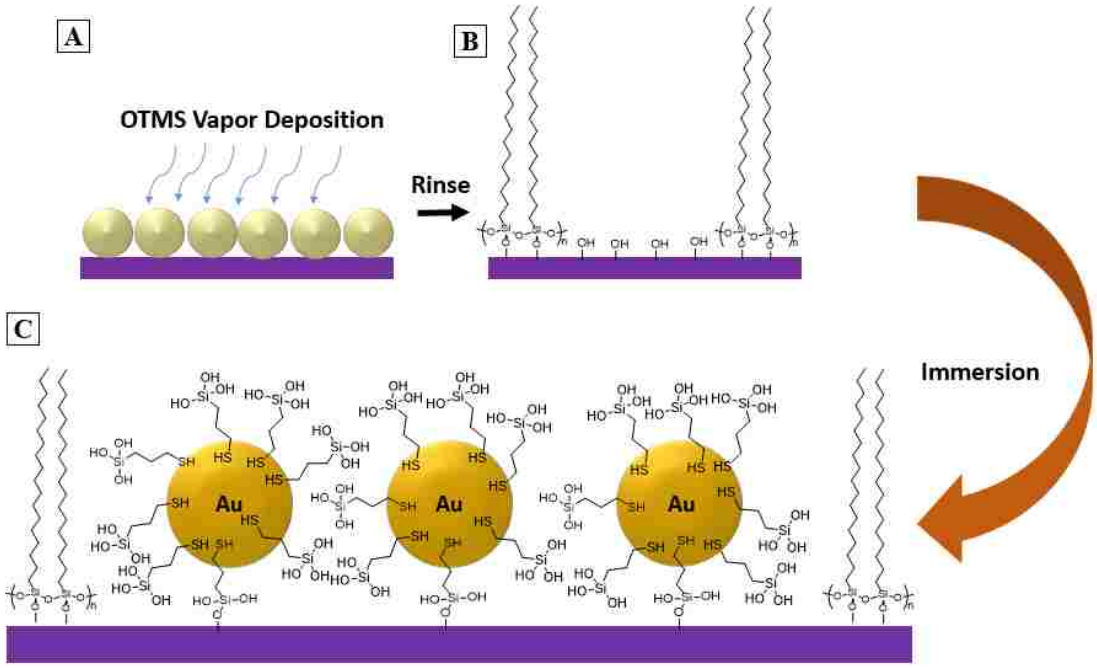

Figure 5.8 Steps for patterning the surface for the deposition of MPTMS coated Au nanoparticles. (A) A surface film of OTMS was prepared by vapor deposition on glass substrates through a mask of 500 nm silica spheres prepared on glass substrates; (B) Spheres were removed by sonication; (C) Samples containing OTMS nanoholes were immersed in a MPTMS coated Au nanoparticle solution for patterning.

The samples of nanoholes within an OTMS matrix on glass were immersed in separate vials for 12, 24 and 48 h in ambient conditions. The results after immersing a sample of nanoholes within a film of OTMS prepared on gold into a solution of MPTMS-coated nanoparticles for 12 h immersion are shown in Figure 5.9. Nanoparticles have attached to the surface, as indicated in the topography frame of Figure 5.9A and simultaneously-acquired phase image of Figure 5.9B. Results for a sample immersed for 24 h in a solution of nanoparticles are shown in Figures 5.9C and 5.9D. A sample prepared with 48 h of immersion is shown with the topography and phase images in Figures 5.9E and Figure 5.9F, respectively. Although nanoparticles are present for each experiment, there are areas where the coated nanoparticles attached to the matrix areas, as well as

nanopattern sites of exposed substrate that do not contain nanoparticles. The results are not consistent, particularly with immersion intervals of 12 and 24 h. An immersion time of 48 h shows the most successful results for nanopatterns (Figure 5.9E), however there are also relatively large aggregates of coated nanoparticles apparent in areas of the sample.

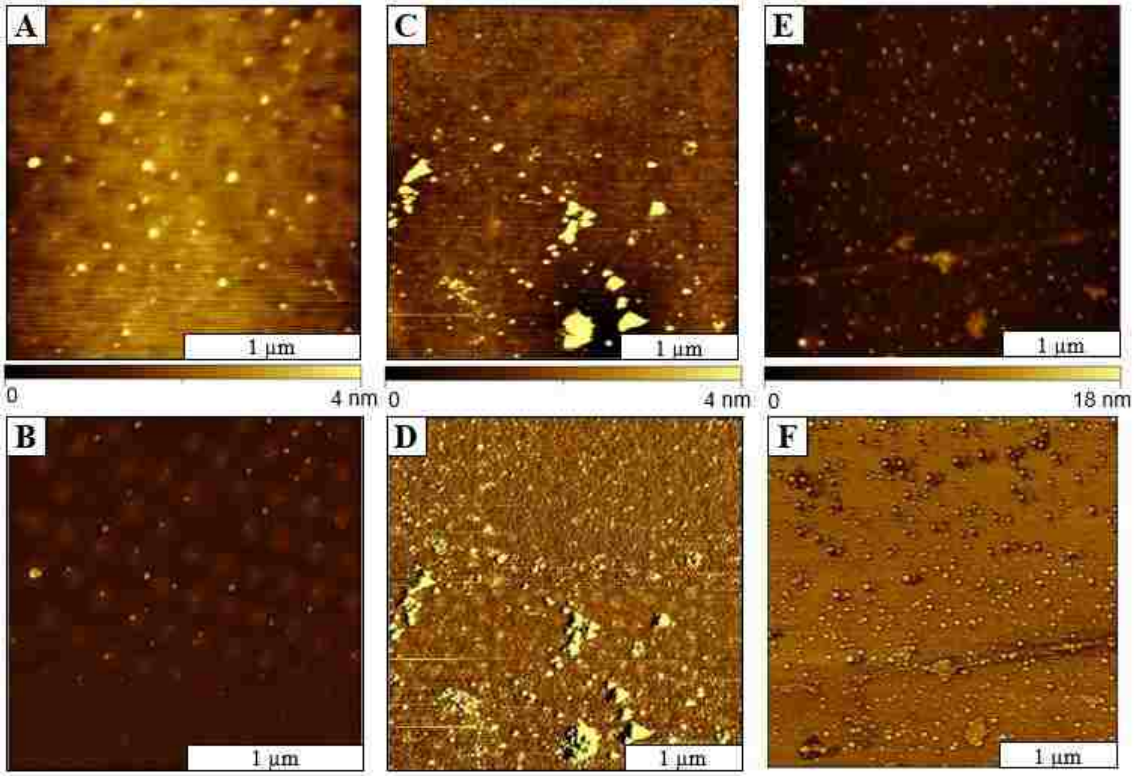

Figure 5.9 Immersion of patterned substrates in solutions of MPTMS-coated nanoparticles for time intervals ranging from 12 to 48 h. (A) Topography frame after 12 h immersion (2 × 2 μm^2); (B) simultaneously phase image; (C) Topography image after 24 h immersion (3 × 3 μm^2); (D) corresponding phase image; (E) Topography imaged after 48 h immersion (3 × 3 μm^2); (F) matching phase image.

5.4 Conclusions

The approaches for surface patterning provide new directions for studying surface chemistry at the molecular-level and have practical applications for emerging nanotechnology. Surfaces were designed for the selective deposition of gold nanoparticles to produce

multicomponent nanopatterns. Molecular-level investigations of the morphology, self-assembly processes, and properties of designed nanostructures of organosilanes were accomplished using AFM. Using particle lithography, well-defined surfaces with desired functionality and spatially defined areas can be achieved. Size-sorted, monodisperse latex or silica spheres were used as a particle mask for nanoscale lithography with designed dimensions and interparticle spacing. By changing the diameter of the spheres, the dimensions and size of nanopatterns can be tuned to define the surface density and arrangement of nanostructures. For future studies, samples will provide model test structures for further studies with AFM measurement modes such as with conductive probe AFM or magnetic imaging. Nanoparticles comprised of other metals and coatings can be evaluated in future experiments. The results presented in this dissertation demonstrate the combination of nanofabrication with detailed AFM characterizations to investigate structure and property relationships as well as measure size-dependent nanoscale properties.

CHAPTER 6. SUMMARY AND FUTURE PROSPECTUS

The research presented in this dissertation highlights results of fundamental AFM studies with metal nanoparticles, metalloporphyrins and zinc phthalocyanines using protocols developed with particle lithography. The investigations described the developments for generating nanostructures of resist layers to produce surface test platforms with complex, multicomponent architectures. Using AFM, characterizations were successfully accomplished for molecular-level investigations of morphology, self-assembly processes, and the properties of designed nanostructures. Characterization with AFM imaging modes such as conductive probe, magnetic sample modulation AFM, and phase imaging were demonstrated, showcasing the capabilities for obtaining structural and physical information with nanometer resolution.

With particle lithography, other possible directions for tailoring the deposition of nanomaterials are to alter the composition of nanoparticles, coatings and functional groups. The metal used for the nanoparticle as well as the surface material can be changed. For the porphyrins and phthalocyanines, the constituents can be functionalized to facilitate surface attachment and strategies for linker chemistry can be investigated. Preliminary results with AFM and particle lithography provide a solid foundation to build upon for further investigations with metal nanoparticles.

The steps of binding porphyrins to exposed sites inside nanoholes fabricated within dodecanethiol on Au(111) were characterized using atomic force microscopy (AFM). Patterned arrays of nanoholes were prepared using steps of particle lithography combined with immersion in thiol solutions. Methyl-terminated SAMs such as dodecanethiol were chosen as a resist layer to direct the adsorption of porphyrins. Spatial selectivity was accomplished for directing the attachment of porphyrins within exposed sites and on the resist. To facilitate binding within the

dodecanethiol nanoholes, a porphyrin with reactive functional groups would increase the binding affinity. For potential applications in miniaturized electronics and photovoltaics, porphyrins have become a focus in engineering functionalized nanostructures on surfaces. Porphyrins can be synthesized with substituents and metal ions to tune electrical and photoelectronic properties.

In collaboration with Professor Graca Vicente's research group, zinc phthalocyanine compounds with designed functional groups were synthesized for studies using protocols for nanopatterning using particle lithography. Spatial selectivity was accomplished for directing the attachment of zinc phthalocyanines to the surface using amine linker chemistry with an amine terminated organosilane, 3-aminopropyltriethoxysilane (APTES). Scanning probe microscopy can probe morphological and physical properties of nanomaterials deposited on surfaces. Phthalocyanines can be chelated with magnetic metals which will offer materials for SPM studies with advanced measurements and imaging modes such as CP-AFM, FMM and MSM. Fluorescence studies were also investigated with samples, however the signals were far too weak for molecularly thin films and nanostructures. Studies with NSOM would be sufficiently sensitive for studying fluorescent properties of the nanostructures. The nanopatterned surfaces exhibit millions of reproducible test structures arranged in a periodic array according to the dimensions and spacing of the surface masks.

Phthalocyanines are antimicrobial which is important for decontaminating body fluids such as blood for patients needing transfusions. The antimicrobial property is dependent on the bacteria used because certain functional groups diminish several strands of bacteria. Inactivation of *Escherichia coli* bacteria using phthalocyanines together with conjugates with silver nanoparticles was reported by Rapulenyane et al.[231] Bacterial death can be investigated by incubating the substrates containing phthalocyanines to known concentrations of bacteria.

Periodic arrays of organosilane nanostructures were prepared with particle lithography to provide a foundation to spatially define sites for adsorption of nanoparticles. Using octadecyltrimethoxysilane (OTMS) and 2-[methoxy(polyethyleneoxy)propyl] trichlorosilane (PEG-silane) as a resist, nanopatterns were prepared on a glass surface using particle lithography combined with vapor deposition and solution immersion. Thickness measurements from AFM cursor profiles were used to evaluate the orientation and density of the OTMS and PEG-silane nanostructures. Future planned directions for this research will apply particle lithography with organosilanes to develop spatially selective surfaces for patterning nanoparticles. Arrays of nanoparticles will provide useful structures for applications. To ensure that only the properties of the nanoparticles can be studied, crystalline surfaces must be used for accurate photonic measurements. Aside from using crystalline quartz as a surface, surfaces with CaF_2 and MgF_2 may also be studied.

There are advanced modes of AFM that can be used to measure surface properties of nanomaterials. Future studies that are planned will include using Kelvin probe force microscopy (KPFM) which is a noncontact mode. Kelvin probe force microscopy was invented in 1991 by Nonnenmacher.[232] The work function of surfaces can be observed at molecular scales which is relevant for samples of ceria and gold. The work functions measured by KPFM provide fundamental information about the electronic states and composition of the nanoparticles. Using KPFM, the work functions of gold and ceria will be studied on a single surface to understand composition and electronic state. The samples will be prepared using two particle lithography. Depending on the concentration and ratios of smaller particles, the patterns generated on surfaces will be nanoholes within a film of nanoparticles or arrays of nanoring surface structures. The arrays should exhibit uniform geometries and periodicity, spanning micrometer-sized areas. The density

and periodicity of the arrays can be controlled by choosing the diameters of the spheres and ratios of nanoparticles. The nanoparticles will be approximately the same size but a difference in conductivity should be apparent due to the difference in work functions.

REFERENCES

1. Haes, A. J.; Van Duynes, R. P., A Nanoscale Optical Biosensor: Sensitivity and Selectivity of an Approach Based on the Localized Surface Plasmon Resonance Spectroscopy of Triangular Silver Nanoparticles. *J. Am. Chem. Soc.* **2002,** *124*, 10596-10604.

2. McFarland, A. D.; Van Duyne, R. P., Single Silver Nanoparticles as Real-Time Optical Sensors with Zeptomole Sensitivity. *Nano Lett.* **2003,** *3*, 1057-1062.

3. Kempa, K.; Kimball, B.; Rybczynski, J.; Huang, Z. P.; Wu, P. F.; Steeves, D.; Sennett, M.; Giersig, M.; Rao, D. V. G. L. N.; Carnhan, D. L.; Wang, D. Z.; Lao, J. Y.; Li, W. Z.; Ren, Z. F., Photonic Crystals Based on Periodic Arrays of Aligned Carbon Nanotubes. *Nano Lett.* **2003,** *3*, 13-18.

4. Han, J.; Craighead, H. G., Separation of Long DNA Molecules in a Microfabricated Entropic Trap Array. *Science* **2000,** *288*, 1026-1029.

5. Landskron, K.; Hatton, B. D.; Perovic, D. D.; Ozin, G. A., Periodic Mesoporous Organosilicas Containing Interconnected [Si(CH2)](3) Rings. *Science* **2003,** *302*, 266-269.

6. Craighead, H. G.; Mankiewich, P. M., Ultra-small Metal Particle Arrays Produced by High Resolution Electron-beam Lithography. *J. Appl. Phys.* **1982,** *53*, 7186-7188.

7. Bayati, M.; Pakota, P.; Giersig, M.; Savinova, E. R., An Approach to Fabrication of Metal Nanoring Arrays. *Langmuir* **2010,** *26*, 3549-3554.

8. Chen, J. X.; Liao, W. S.; Chen, X.; Yang, T. L.; Wark, S. E.; Son, D. H.; Batteas, J. D.; Cremer, P. S., Evaporation-Induced Assembly of Quantum Dots into Nanorings. *ACS Nano* **2009,** *3*, 173-180.

9. Garno, J. C.; Amro, N. A.; Wadu-Mesthrige, K.; Liu, G.-Y., Production of Periodic Arrays of Protein Nanostructures Using Particle Lithography. *Langmuir* **2002,** *18*, 8186-8192.

10. Lusker, K. L.; Yu, J.-J.; Garno, J. C., Particle lithography with vapor deposition of organosilanes: A molecular toolkit for studying confined surface reactions in nanoscale liquid volumes. *Thin Solid Films* **2011,** *519*, 5223-5229.

11. Jiang, P.; McFarland, M. J., Large-scale fabrication of wafer-size colloidal crystals, macroporous polymers and nanocomposites by spin-coating. *J. Am. Chem. Soc.* **2004,** *126*, 13778-13786.

12. Tessier, P. M.; Velev, O. D.; Kalambur, A. T.; Lenhoff, A. M.; Rabolt, J. F.; Kaler, E. W., Structured metallic films for optical and spectroscopic applications via colloidal crystal templating. *Adv. Mater.* **2001,** *13*, 396-400.

13. Hulteen, J. C.; Treichel, D. A.; Smith, M. T.; Duval, M. L.; Jensen, T. R.; Van Duyne, R. P., Nanosphere lithography: size-tunable silver nanoparticle and surface cluster arrays. *J. Phys. Chem. B* **1999,** *103,* 3854-3863.

14. Lewandowski, B. R.; Kelley, A. T.; Singleton, R.; Li, J.-R.; Lowry, M.; Warner, I. M.; Garno, J. C., Nanostructures of cysteine-coated CdS nanoparticles produced with "two-particle" lithography. *J. Phys. Chem. C* **2009,** *113,* 5933-5940.

15. Zrimsek, A. B.; Boman, F.; Van Duyne, R. P. In *Plasmonic properties of Au nanoparticles fabricated by hole-mask colloidal lithography*, Abstr. Pap. Am. Chem. Soc. , AMER CHEMICAL SOC 1155 16TH ST, NW, WASHINGTON, DC 20036 USA: 2011.

16. Nonckreman, C. J.; Fleith, S.; Rouxhet, P. G.; Dupont-Gillain, C. C., Competitive adsorption of fibrinogen and albumin and blood platelet adhesion on surfaces modified with nanoparticles and/or PEO. *Colloid Surf. B-Biointerfaces* **2010,** *77,* 139-149.

17. Singh, G.; Griesser, H. J.; Bremmell, K.; Kingshott, P., Highly Ordered Nanometer-Scale Chemical and Protein Patterns by Binary Colloidal Crystal Lithography Combined with Plasma Polymerization. *Adv. Funct. Mater.* **2011,** *21,* 540-546.

18. Singh, G.; Gohri, V.; Pillai, S.; Arpanaei, A.; Foss, M.; Kingshott, P., Large-area protein patterns generated by ordered binary colloidal assemblies as templates. *ACS Nano* **2011,** *5,* 3542-3551.

19. Briseno, A. L.; Han, S.; Rauda, I. E.; Zhou, F.; Toh, C.-S.; Nemanick, E. J.; Lewis, N. S., Electrochemical polymerization of aniline monomers infiltrated into well-ordered truncated eggshell structures of polyelectrolyte multilayers. *Langmuir* **2004,** *20,* 219-226.

20. Ellinas, K.; Tserepi, A.; Gogolides, E., From superamphiphobic to amphiphilic polymeric surfaces with ordered hierarchical roughness fabricated with colloidal lithography and plasma nanotexturing. *Langmuir* **2011,** *27,* 3960-3969.

21. Jiang, P.; Hwang, K.; Mittleman, D.; Bertone, J.; Colvin, V., Template-directed preparation of macroporous polymers with oriented and crystalline arrays of voids. *J. Am. Chem. Soc.* **1999,** *121,* 11630-11637.

22. Singh, A.; Kulkarni, S. K.; Khan-Malek, C., Patterning of SiO 2 nanoparticle–PMMA polymer composite microstructures based on soft lithographic techniques. *Microelectron. Eng.* **2011,** *88,* 939-944.

23. Bae, C.; Kim, H.; Shin, H., Contact area lithography and pattern transfer of self-assembled organic monolayers on SiO 2/Si substrates. *Chem. Commun* **2011,** *47,* 5145-5147.

24. Bae, C.; Shin, H.; Moon, J.; Sung, M. M., Contact area lithography (CAL): A new approach to direct formation of nanometric chemical patterns. *Chem. Mat.* **2006,** *18,* 1085-1088.

25. Geissler, M.; McLellan, J. M.; Chen, J.; Xia, Y., Side-by-Side Patterning of Multiple Alkanethiolate Monolayers on Gold by Edge-Spreading Lithography. *Angew. Chem.-Int. Edit.* **2005,** *44*, 3596-3600.

26. Li, J.-R.; Garno, J. C., Elucidating the role of surface hydrolysis in preparing organosilane nanostructures via particle lithography. *Nano Lett.* **2008,** *8*, 1916-1922.

27. McLellan, J. M.; Geissler, M.; Xia, Y., Edge spreading lithography and its application to the fabrication of mesoscopic gold and silver rings. *J. Am. Chem. Soc.* **2004,** *126*, 10830-10831.

28. Ulman, A., Formation and structure of self-assembled monolayers. *Chem. Rev.* **1996,** *96*, 1533-1554.

29. Ulman, A., Self-assembled monolayers of alkyltrichiorosilanes: Building blocks for future organic materials. *Adv. Mater.* **1990,** *2*, 573-582.

30. Xie, X. N.; Chung, H. J.; Sow, C. H.; Wee, A. T. S., Nanoscale Materials Patterning and Engineering by Atomic Force Microscopy Nanolithography. *Mater. Sci. Eng. R-Rep.* **2006,** *54*.
31. Li, D. B.; Bonell, D. A., Controlled Patterning of Ferroelectric Domains: Fundamental Concepts and Applications. *Annu. Rev. Mater. Res.* **2008,** *38*, 351-368.

32. Zotti, G.; Vercelli, B.; Berlin, A., Monolayers and Multilayers of Conjugated Polymers as Nanosized Electronic Components. *Accounts Chem. Res.* **2008,** *41*, 1098-1109.

33. McCreery, R. L., Molecular Electronic Junctions. *Chem. Mater.* **2004,** *16*, 4477-4496.

34. Taylor, A. M.; Okoth, E. J. A.; Kuruppu Arachchige; KuruppuArachchige, N. M. K.; Vicente, M. G. H.; Garno, J. C., Nanopatterns of zinc phthalocyanines prepared using particle lithography: Characterization of patterning steps with scanning probe microscopy. *Surf. Interface Anal.* **2017,** *submitted*.

35. Spikes, J. D., Phthalocyanines as photosensitizers in biological systems and for the photodynamic therapy of tumors. *Photochem. Photobiol.* **1986,** *43*, 691-699.

36. Eichhorn, H., Mesomorphic phthalocyanines, tetraazaporphyrins, porphyrins and triphenylenes as charge-transporting materials. *J. Porphyrins Phthalocyanines* **2000,** *4*, 88-102.

37. Zagal, J. H.; Griveau, S.; Francisco Silva, J.; Nyokong, T.; Bedioui, F., Metallophthalocyanine-based molecular materials as catalysts for electrochemical reactions. *Coord. Chem. Rev.* **2010,** *254*, 2755-2791.

38. Yourre, T. A.; Rudaya, L. I.; Klimova, N. V.; Shamanin, V., Organic materials for photovoltaic and light-emitting devices. *Semiconductors* **2003,** *37*, 807-815.

39. Allen, C. M.; Sharman, W. M.; Van Lier, J. E., Current status of phthalocyanines in the photodynamic therapy of cancer. *J. Porphyrins Phthalocyanines* **2001,** *5*, 161-169.

40. Wen, K.; Maoz, R.; Cohen, H.; Sagiv, J.; Gibaud, A.; Desert, A.; Ocko, B. M., Postassembly chemical modification of a highly ordered organosilane multilayer: New insights into the structure, bonding, and dynamics of self-assembling silane monolayers. *ACS Nano* **2008,** *2* (3), 579-599.

41. Mornet, S.; Bre´tagnol, F.; Ilaria, M.; Valsesia, A.; Sirghi, L.; Colpo, P.; Rossi, F., Large-Scale Fabrication of Bi-Functional Nanostructured Polymer Surfaces for Selective Biomolecular Adhesion. *Small* **2008,** *4*, 1919-1924.

42. Trujillo, N. J.; Baxamusa, S. H.; Gleason, K. K., Grafted Functional Polymer Nanostructures Patterned Bottom-Up by Colloidal Lithography and Initiated Chemical Vapor Deposition (iCVD). *Chem. Mater.* **2009,** *21*, 742-750.

43. Kosiorek, A.; Kandulski, W.; Glaczynska, H.; Giersig, M., Fabrication of Nanoscale Rings, Dots, and Rods by Combining Shadow Nanosphere Lithography and Annealed Polystyrene Nanosphere Masks. *Small* **2005,** *1*, 439-444.

44. Jeong, J.-R.; Kim, S.; Kim, S.-H.; Bland, J. A. C.; Shin, S.-C.; Yang, S.-M., Fabrication of Hexagonal Lattice Co/Pd Multilayer Nanodot Arrays Using Colloidal Lithography. *Small* **2007,** *3*, 1529-1533.

45. Zhou, C. M.; Gall, D., Surface Patterning by Nanosphere Lithography for Layer Growth with Ordered Pores. *Thin Solid Films* **2007,** *516*, 433-437.

46. Abdelsalam, M. E.; Bartlett, P. N.; Baumberg, J. J.; Coyle, S., Preparation of Arrays of Isolated Spherical Cavities by Self-Assembly of Polystyrene Spheres on Self-Assembled Pre-Patterned Macroporous Films. *Adv. Mater.* **2004,** *16*, 90-93.

47. Sun, Z.; Li, Y.; Zhang, J.; Li, Y.; Zhao, Z.; Zhang, K.; Zhang, G.; Guo, J.; Yang, B., A Universal Approach to Fabricate Various Nanoring Arrays Based on a Colloidal-Crystal-Assisted-Lithography Strategy. *Adv. Funct. Mater.* **2008,** *18*, 4036-4042.

48. Chen, X.; Chen, Z.; Fu, N.; Lu, G.; Yang, B., Versatile Nanopatterned Surfaces Generated via Three-Dimensional Colloidal Crystals. *Adv. Mater.* **2003,** *15*, 1413-1417.

49. Li, J. R.; Lusker, K. L.; Yu, J. J.; Garno, J. C., Engineering the Spatial Selectivity of Surfaces at the Nanoscale Using Particle Lithography Combined with Vapor Deposition of Organosilanes. *ACS Nano* **2009,** *3*, 2023-2035.

50. Li, J.-R.; Garno, J. C., Nanostructures of Octadecyltrisiloxane Self-Assembled Monolayers Produced on Au(111) Using Particle Lithography. *ACS Appl. Mater. Interfaces* **2009,** *1*, 969-976.

51. Rybczynski, J.; Ebels, U.; Giersig, M., Large-scale, 2D Arrays of Magnetic Nanoparticles. *Colloids Surf. A* **2003,** *219*, 1-6.

52. Li, J. R.; Henry, G. C.; Garno, J. C., Fabrication of nanopatterned films of bovine serum albumin and staphylococcal protein A using latex particle lithography. *Analyst* **2006,** *131*, 244-250.

53. Cai, Y.; Ocko, B. M., Large-Scale Fabrication of Protein Nanoarrays Based on Nanosphere Lithography. *Langmuir* **2005,** *21*, 9274-9279.

54. Binnig, G.; Quate, C. F.; Gerber, C., Atomic Force Microscope. *Phys. Rev. Lett.* **1986,** *56*, 930-933.

55. Hansma, P. K.; Elings, V. B.; Marti, O.; Bracker, C. E., Scanning Tunneling Microscopy and Atomic Force Microscopy - Application to Biology and Technology. *Science* **1988,** *242*, 209-216.

56. Sagiv, J., Organized Monolayers by Adsorption. 1. Formation and Structure of Oleophobic Mixed Monolayers on Solid Surfaces. *J. Am. Chem. Soc.* **1980,** *02*, 92-98.

57. Deckman, H.; Dunsmuir, J., Natural lithography. *Appl. Phys. Lett.* **1982,** *41* (4), 377-379.

58. Hulteen, J. C.; Van Duyne, R. P., Nanosphere Lithography: A Materials General Fabrication Process for Periodic Particle Array Surfaces. *J. Vac. Sci. Technol. A* **1995,** *13*, 1553-1558.

59. Denis, F. A.; Hanarp, P.; Sutherland, D. S.; Gold, J.; Mustin, C.; Rouxhet, P. G.; Dufrene, Y. F., Protein Adsorption on Model Surfaces with Controlled Nanotopography and Chemistry. *Langmuir* **2002,** *18*, 819-828.

60. Lipson, A. L.; Comstock, D. J.; Hersam, M. C., Nanoporous Templates and Membranes Formed by Nanosphere Lithography and Aluminum Anodization. *Small* **2009,** *5*.

61. Jiang, P.; Prasad, T.; McFarland, M. J.; Colvin, V. L., Two-dimensional Nonclose-packed Colloidal Crystals Formed by Spincoating. *Appl. Phys. Lett.* **2006,** *89*, 011908.

62. Weiler, M.; Pacholski, C., Soft colloidal lithography. *RSC Adv.* **2017,** *7*, 10688-10691.

63. Hiroshige, S.; Kureha, T.; Aoki, D.; Sawada, J.; Aoki, D.; Takata, T.; Suzuki, D., Formation of Tough Films by Evaporation of Water from Dispersions of Elastomer Microspheres Crosslinked with Rotaxane Supramolecules. *Chem. Eur. J.* **2017,** *23*, 8405-8408.

64. Hayward, R. C.; Saville, D. A.; Aksay, I. A., Electrophoretic Assembly of Colloidal Crystals with Optically Tunable Micropatterns. *Nature* **2000,** *404* (56-59).

65. Trau, M.; Saville, D. A.; Aksay, I. A., Field-induced Layering of Colloidal Crystals. *Science* **1996,** *272*, 706-709.

66. Mate, C. M.; McClelland, G. M.; Erlandsson, R.; Chiang, S., Atomic-scale Friction of a Tungsten Tip on a Graphite Surface. *Phys. Rev. Lett.* **1987,** *59*, 1942-1945.

67. Markiewicz, P.; Goh, M. C., Atomic-Force Microscopy Probe Tip Visualization and Improvement of Images using a Simple Deconvolution Procedure. *Langmuir* **1994,** *10*, 5-7.

68. Villarrubia, J. S., Algorithms for Scanned Probe Microscope Image Simulation, Surface Reconstruction, and Tip Estimation. *J. Res. Natl. Inst. Stand.* **1997,** *102*, 425-454.

69. Williams, P. M.; Shakesheff, K. M.; Davies, M. C.; Jackson, D. E.; Roberts, C. J.; Tendler, S. J. B., Blind Reconstruction of Scanning Probe Image Data. *J. Vac. Sci. Technol. B* **1996,** *14*, 1557-1562.

70. Fritz, M.; Radmacher, M.; Cleveland, J. P.; Allersma, M. W.; Stewart, R. J.; Gieselmann, R.; Janmey, P.; Schmidt, C. F.; Hansma, P. K., Imaging Globular and Filamentous Proteins in Physiological Buffer Solutions with Tapping Mode Atomic-force Microscopy. *Langmuir* **1995,** *11*, 3529-3535.

71. Wilson, D. L.; Kump, K. S.; Eppell, S. J.; Marchant, R. E., Morphological Restoration of Atomic-force Microscopy Images. *Langmuir* **1995,** *11*, 265-272.

72. Moller, C.; Allen, M.; Elings, V.; Engel, A.; Muller, D. J., Tapping-mode Atomic Force Microscopy Produces Faithful High-resolution Images of Protein Surfaces. *Biophys. J.* **1997,** *77*, 1150-1158.

73. Thomann, Y.; Cantow, H. J.; Bar, G.; Whangbo, M. H., Investigation of Morphologies and Nanostructures of Polymer Blends by Tapping Mode Phase Imaging. *Appl. Phys. A: Mater. Sci. Process* **1998,** *66*, S1233-S1236.

74. Raghavan, D.; Gu, X.; Nguyen, T.; VanLandingham, M.; Karim, A., Mapping Polymer Heterogeneity using Atomic Force Microscopy Phase Imaging and Nanoscale Indentation. *Macromolecules* **2000,** *33*, 2573-2583.

75. Tesfai, A.; El-Zahab, B.; Kelley, A. T.; Li, M.; Garno, J. C.; Baker, G. A.; Warner, I. M., Magnetic and Nonmagnetic Nanoparticles from a Group of Uniform Materials Based on Organic Salts. *ACS Nano* **2003,** *3*, 3244-3250.

76. Terrill, R. H.; Postlethwaite, T. A.; Chen, C. H.; Poon, C. D.; Terzis, A.; Chen, A. D.; Hutchison, J. E.; Clark, M. R.; Wignall, G.; Londono, J. D.; Superfine, R.; Falvo, M.; Johnson, C. S.; Samulski, E. T.; Murray, R. W., Monolayers in Three Dimensions: NMR, SAXS, Thermal, and Electron Hopping Studies of Alkanethiol Stabilized Gold Clusters. *J. Am. Chem. Soc.* **1995,** *117*, 12537-12548.

77. Ibanez, F. J.; Gowrishetty, U.; Crain, M. M.; Walsh, K. M.; Zamborini, F. P., Chemiresistive Vapor Sensing with Microscale Films of Gold Monolayer Protected Clusters. *Anal. Chem.* **2006,** *78*, 753-761.

78. Sagiv, J., Organized monolayers by adsorption. 1. Formation and structure of oleophobic mixed monolayers on solid surfaces. *J. Am. Chem. Soc.* **1980,** *102* (1), 92-98.

79. Onclin, S.; Ravoo, B. J.; Reinhoudt, D. N., Engineering silicon oxide surfaces using selfassembled monolayers. *Angew. Chem. Int. Ed.* **2005,** *44*, 6282-6304.

80. Love, J. C.; Estroff, L. A.; Kriebel, J. K.; Nuzzo, R. G.; Whitesides, G. M., Self-assembled monolayers of thiolates on metals as a form of nanotechnology. *Chem. Rev.* **2005,** *105*, 1103-1170.

81. Shaporenko, A.; Ulman, A.; Terfort, A.; Zharnikov, A., Self-assembled monolayers of alkaneselenolates on (111) gold and silver. *J. Phys. Chem. B* **2005,** *109*, 3898-3906.

82. Dubois, L. H.; Nuzzo, R. G., Synthesis, structure and properties of model organic-surfaces. *Annu. Rev. Mater. Sci.* **1992,** *43*, 437-463.

83. Poirier, G. E., Characterization of organosulfur molecular monolayers on Au(111) using scanning tunneling microscopy. *Chem. Rev.* **1997,** *97*, 1117-1128.

84. Schreiber, F., Structure and growth of self-assembling monolayers. *Prog. Surf. Sci.* **2000,** *65*, 151-257.

85. Zhai, X.; Lee, H. J.; Tian, T.; Lee, T. R.; Garno, J. C., Nanoscale lithography mediated by surface self-assembly of 16-[3,5-bis(mercaptomethyl)phenoxy]hexadecanoic acid on Au(111) investigated by scanning probe microscopy. *Molecules* **2014,** *19*, 13010-13026.

86. Shumaker-Parry, J. S.; Zareie, M. H.; Aebersold, R.; Campbell, C. T., Microspotting streptavidin and double-stranded DNA Arrays on gold for high-throughput studies of protein-DNA interactions by surface plasmon resonance microscopy. *Anal. Chem.* **2004,** *76*, 918-929.

87. Fendler, J. H., Chemical self-assembly for electronic applications. *Chem. Mater.* **2001,** *13*, 3196-3210.

88. Willey, T.; Vance, A.; Fadley, C. S., Rapid degradation of alkanethiol-based self-assembled monolayers on gold in ambient laboratory conditions. *Surf. Sci.* **2005,** *567*, 188-196.

89. Liu, G.-Y.; Xu, S.; Qian, Y., Nanofabrication of self-assembled monolayers using scanning probe lithography. *Acc. Chem. Res.* **2000,** *33*, 457-466.

90. Lavrich, D.; Wetterer, S.; Bernasek, S.; Scoles, G., Physisorption and chemisorption of alkanethiols and alkylsulfides on Au (111). *J. Phys. Chem. B.* **1998,** *102*, 3456-3465.

91. Tian, T.; Singhana, B.; Englade-Franklin, L. E.; Zhai, X.; Lee, T. R.; Garno, J. C., Surface assembly and nanofabrication of 1,1,1-tris(mercaptomethyl)heptadecane on Au(111) studied with time-lapse atomic force microscopy. *Beilstein J Nanotechnol* **2014,** *5*, 26-35.

92. Xu, S.; Cruchon-Dupeyrat, S.; Garno, J. C.; Liu, G.-Y., In situ studies of thiol self-assembly on gold from solution using atomic force microscopy. *J. Chem. Phys.* **1998,** *108*, 5002.

93. Nuzzo, R. G.; Korenic, E. M.; Dubois, L. H., Studies of the temperature-dependent phase-behavior of long-chain normal-alkyl thiol monolayers on gold. *J. Chem. Phys.* **1990,** *93*, 767.

94. Himmelhaus, M.; Gauss, I.; Buck, M.; Eisert, F.; Woll, C.; Grunze, M., Adsorption of docosanethiol from solution on polycrystalline silver surfaces: an XPS and NEXAFS study. *J. Electron. Spectrosc. Relat. Phenom.* **1998,** *92*, 139.

95. Tillman, N.; Ulman, A.; Schildkraut, J. S.; Penner, T. L., Incorporation of phenoxy groups in self-assembled monolayers of trichlorosilane derivatives - effects on film thickness, wettability and molecular-orientation. *J. Am. Chem. Soc.* **1988,** *110*, 6136-6144.

96. Peanasky, J.; Schneider, H. M.; Granick, S.; Kessel, C. R., Self-assembled monolayers on mica for experiments utilizing the surface forces apparatus. *Langmuir* **1995,** *11*, 953-962.

97. Schwartz, D. K.; Steinberg, S.; Israelachvili, J.; Zasadzinski, J. A. N., Growth of a self-assembled monolayer by fractal aggregation. *Phys. Rev. Lett.* **1992,** *69*, 3354.

98. Ulman, A., An introduction to ultrathin organic films from Langmuir-Blodgett to self-assembly. *Academic Press, New York* **1991**.

99. Schreiber, F., Self-assembled monolayers: from "simple" model systems to biofunctionalized interfaces. *J. Phys.: Condens. Matter* **2004,** *16*, R881.

100. Porter, M. D.; Bright, T. B.; Allara, D. L.; Chidsey, C. E. D., Spontaneously organized molecular assemblies .4. Structural characterization of normal-alkyl thiol monolayers on gold by optical ellipsometry, infrared-spectroscopy and electrochemistry. *J. Am. Chem. Soc.* **1987,** *109*, 3559-3568.

101. Fenter, P.; Eberhardt, A.; Liang, K. S.; Eisenberger, P., Epitaxy and chainlength dependent strain in self-assembled monolayers. *J. Chem. Phys.* **1996,** *106*, 1600.

102. Vieu, C.; Carcenac, F.; Pépin, A.; Chen, Y.; Mejias, M.; Lebib, A.; Manin-Ferlazzo, L.; Couraud, L.; Launois, H., Electron beam lithography: resolution limits and applications. *Appl. Surf. Sci.* **2000,** *164*, 111-117.

103. Gölzhäuser, A.; Eck, W.; Geyer, W.; Stadler, V.; Weimann, T.; Hinze, P.; Grunze, M., Chemical nanolithography with electron beams. *Adv. Mater.* **2001,** *11*, 806-809.

104. Mendes, P. M.; Preece, J. A., Precision chemical engineering: integrating nanolithography and nanoassembly. *Curr. Opin. Colloid Interface Sci.* **2004,** *9*, 236-248.

105. Zharnikov, M.; Grunze, M., Modification of thiol-derived self-assembling monolayers by electron and x-ray irradiation: Scientific and lithographic aspects. *J. Vac. Sci. Technol. B* **2002,** *20*, 1793-1807.

106. Smith, H. I.; Schattenburg, M. L.; Hector, S. D.; Ferrera, J.; Moon, E. E.; Yang, I. Y.; Burkhardt, M., X-ray nanolithography: Extension to the limits of the lithographic process. *Microelectron. Eng.* **1996,** *32*, 143-158.

107. Smith, H. I.; Schattenburg, M. L., X-Ray Lithography, from 500 to 30 nm - X-ray Nanolithography. *IBM J. Res. Development* **1993,** *37*, 319-329.

108. Moczala, M.; Kwoka, K.; Piasecki, T.; Kunicki, P.; Sierakowski, A.; Gotszalk, T., Fabrication and characterization of micromechanical bridges with strain sensors deposited using focused electron beam induced technology. *Microelectron Eng* **2017,** *176*, 111-115.

109. Zhao, X.; Wen, J.; Zhang, M.; Wang, D.; Wang, Y.; Chen, L.; Zhang, Y.; Yang, J.; Du, Y., Design of Hybrid Nanostructural Arrays to Manipulate SERS-Active Substrates by Nanosphere Lithography. *ACS Appl. Mater. Interfaces* **2017,** *9*, 7710-7716.

110. Oddone, V.; Giersig, M., Nanosphere lithography with variable deposition angle for the production of one-directional transparent conductors. *Phys. Status Solidi RRL* **2017,** *11*, 1700005.

111. Ngunjiri, J. N.; Daniels, S. L.; Li, J. R.; Serem, W. K.; Garno, J. C., Controlling the surface coverage and arrangement of proteins using particle lithography. *Nanomedicine* **2008,** *3*, 529-541.

112. Lenk, S.; Kaestner, M.; Lenk, C.; Rangelow, I. W., Simulation of field emission from volcano-gated tips for scanning probe lithography. *Microelectron Eng* **2017,** *177*, 19-24.

113. Durrani, Z.; Jones, M.; Kaestner, M.; Hofer, M.; Gulivev, E., Scanning probe lithography approach for beyond CMOS devices *Alternative Lithographic Technologies V* **2013,** *8680*, 868017.

114. Quate, C. F., Scanning probes as a lithography tool for nanostructures. *Surf. Sci.* **1997,** *386*, 259-264.

115. Zhou, P.; Yu, H.; Yang, W.; Wen, Y.; Wang, Z.; Li, W. J.; Liu, L., Spatial Manipulation and Assembly of Nanoparticles by Atomic Force Microscopy Tip-Induced Dielectrophoresis. *ACS Appl. Mater. Interfaces* **2017,** *9*, 16715-16724.

116. Jaschke, M.; Butt, H. J., Deposition of Organic Material by the Tip of a Scanning Force Microscope. *Langmuir* **1995,** *11*, 1061-1064.

117. Ahn, Y.; Son, J. Y., Size effect on polarization switching kinetics of P(VDF-TrFE) copolymer nanodots. *Organic Electronics* **2017,** *41*, 205-208.

118. Piner, R. D.; Zhu, J.; Xu, F.; Hong, S. H.; Mirkin, C. A., Dip-Pen Nanolithography. *Science* **1999,** *283*, 661.

119. Salaita, K.; Wang, Y. H.; Mirkin, C. A., Applications of dip-pen nanolithography. *Nature Nanotechnol.* **2007,** *2*, 145-155.

120. Hu, K.; Wang, Q., Effect of the electric-field distribution on the morphology of dot-array gratings fabricated by AFM-based nanolithography *Int. J. of Nanomanufacturing* **2017,** *13*, 23-32.

121. Calleja, M.; Garcia, R., Nano-oxidation of silicon surfaces by noncontact atomic-force microscopy: Size dependence on voltage and pulse duration. *Appl. Phys. Lett.* **2000,** *76*, 3427-3429.

122. Held, R.; Vancura, T.; Heinzel, T.; Ensslin, K.; Holland, M.; Wegscheider, W., In-plane gates and nanostructures fabricated by direct oxidation of semiconductor heterostructures with an atomic force microscope. *App. Phys. Letts.* **1998,** *73*, 262-264.

123. Garcia, R.; Martinez, R. V.; Martinez, J., Nano-chemistry and scanning probe nanolithographies. *Chem. Soc. Rev.* **2005,** *35*, 29-38.

124. Ryu, Y. K.; Garcia, R., Advanced oxidation scanning probe lithography. *Nanotechnology* **2017,** *28*, 1-17.

125. Zhang, L.; Zhang, J.; Yuan, D.; Han, L.; Zhou, J. Z.; Tian, Z. W.; Tian, Z. Q.; Zhan, D., Electrochemical nanoimprint lithography directly on n-type crystalline silicon (111) wafer. *Electrochem. Commun.* **2017,** *75*, 1-4.

126. Blackledge, C.; Engebretson, D. A.; McDonald, J. D., Nanoscale site-selective catalysis of surface assemblies by palladium-coated atomic force microscopy tips: Chemical lithography without electrical current. *Langmuir* **2000,** *16*, 8317-8323.

127. Wan, L.; Zhu, N.; Zhang, R., All-polymeric planar waveguide devices based on a gas-assisted thermal imprinting technique. *Microsyst. Technol* **2017,** *17*, 3297-3299.

128. Hua, Y.; King, W. P.; Henderson, C. L., Nanopatterning materials using area selective atomic layer deposition in conjunction with thermochemical surface modification via heated AFM cantilever probe lithography. *Microelectron Eng* **2008,** *85*, 934-936.

129. Yang, M.; Sheehan, P. E.; King, W. P.; Whitman, L. J., Direct writing of a conducting polymer with molecular-level control of physical dimensions and orientation. *J. Am. Chem. Soc.* **2006,** *128*, 6774-6775.

130. Zhou, D.; Bruckbauer, A.; Ying, L.; Abell, C.; Klenerman, D., Building Threedimensional surface biological assemblies on the nanometer scale. *Nano Lett.* **2003,** *3*, 1517-1520.

131. Shi, J.; Chen, J.; Cremer, P. S., Sub-100 nm patterning of supported bilayers by nanoshaving lithography. *J. Am. Chem. Soc.* **2008,** *130*, 2718-2719.

132. Cosert, K. M.; Steidl, R. J.; Castro-Forero, A.; Worden, R. M.; Reguera, G., Electronic characterization of Geobacter sulfurreducenspilins in self-assembled monolayers unmasks tunnelling and hopping conduction pathways. *Phys. Chem. Chem. Phys.* **2017,** *19*, 11163-11172.

133. Liang, J.; Rosa, L. G.; Scoles, G., Nanostructuring, imaging and molecular manipulation of dithiol monolayers on Au(111) Surfaces by atomic force microscopy. *J. Phys. Chem. C* **2007,** *111*, 17275-17284.

134. Rotella, C.; Doni, G.; Bosco, A.; Castronovo, M.; De Vita, A.; Casalis, L.; Pavan, G. M.; Parisse, P., Site accessibility tailors DNA cleavage by restriction enzymes in DNA confined monolayers. *Nanoscale* **2017,** *9*, 6399-6405.

135. Liu, M.; Amro, N. A.; Liu, G.-Y., Nanografting for surface physical chemistry. *Annu. Rev. Phys. Chem.* **2008,** *59*, 367-386.

136. Bonnell, D. A., Scanning Probe Microscopy and Spectroscopy: Theory, Techniques, and Applications. *Wiley-VCH* **2001**.

137. Takano, H.; Kenseth, J. R.; Wong, S. S.; O'Brien, J. C.; Porter, M. D., Chemical and Biochemical Analysis using Scanning Force Microscopy. *Chem. Rev.* **1999,** *99*, 2845-2890.

138. Capella, B.; Dietler, G., Force-Distance Curve by Atomic Force Micrscopy. *Surf. Sci. Rep.* **1999,** *34*, 1-104.

139. Aoki, T.; Hiroshima, M.; Kitamura, K.; Tokunaga, M.; Yanagida, T., Non-contact scanning probe microscopy with sub-piconewton force sensitivity. *Ultramicroscopy* **1997,** *70*, 45-55.

140. Weisenhorn, A. L.; Maivald, P.; Butt, H. J.; Hansma, P. K., Measuring adhesions, attraction, and repulsion between surfaces in liquids with an atomic-force microscope. *Phys. Rev. B* **1992,** *45*, 11226-11232.

141. Gotsmann, B.; Seidel, C.; Anczykowski, B.; Fuchs, H., Conservative and Dissipative Tipsample Interaction Forces Probed with Dynamic AFM. *Phys. Rev. B* **1999,** *60*, 11051-11061.

142. Tamayo, J.; Garcia, R., Deformation, Contact Time, and Phase Contrast in Tapping Mode Scanning Force Microscopy. *Langmuir* **1996,** *12*, 4430-4435.

143. Sulchek, T.; Yaralioglu, G. G.; Quate, C. F.; Minne, S. C., Characterization and Optimization of Scan Speed for Tapping-mode Atomic Force Microscopy. *Rev. Sci. Instrum.* **2002,** *73*, 2928-2936.

144. Ogoshi, T.; Fujiwara, T.; Bertolucci, M.; Galli, G.; Chiellini, E.; Chujo, Y.; Wynne, K. J., Tapping Mode AFM Evidence for an Amorphous Reticular Phase in a Condensationcured

Hybrid Elastomer:
Alpha,Omegadihydroxypoly(dimethylsiloxane)/poly(diethonysiloxane)/fumed Silica Nanoparticles. *J. Am. Chem. Soc.* **2004,** *126*, 12284-12285.

145. Dong, R.; Yu, L. Y. E., Investigation of Surface Changes of Nanoparticles using TMAFM Phase Imaging. *Environ. Sci. Technol.* **2003,** *37*, 2813-2819.

146. Aytun, T.; Mutaf, O. F.; El-Atwani, O. J.; Ow-Yang, C. W., Nanoscale Composition Mapping of Segregation in Micelles with Tapping-Mode Atomic Force Microscopy. *Langmuir* **2008,** *24*, 14183-14187.

147. Kelley, T. W.; Granstrom, E. L.; Frisbie, C. D., Conducting probe atomic force microscopy: A characterization tool for molecular electronics. *Adv. Mater.* **1999,** *11* (261-264).

148. de Pablo, P. J.; Gomez-Navarro, C.; Martinez, M. T.; Benito, A. M.; Maser, W. K.; Colchero, J.; Gomez-Herrero, J.; Baro, A. M., Performing current versus voltage measurements of single-walled carbon nanotubes using scanning force microscopy. *Appl. Phys. Lett.* **2002,** *80*, 1462-1464.

149. Yang, G. H.; Tan, L.; Yang, Y. Y.; Chen, S. W.; Liu, G. Y., Single electron tunneling and manipulation of nanoparticles on surfaces at room temperature. *Surf. Sci.* **2005,** *589*, 129-138.
150. Gosvami, N.; Lau, K. H. A.; Sinha, S. K.; O'Shea, S. J., Effect of end groups on contact resistance of alkanethiol based metal-molecule-metal junctions using current sensing AFM. *Appl. Surf. Sci.* **2006,** *252*, 3956-3960.

151. Daniels, S. L.; Ngunjiri, J. N.; Garno, J. C., Investigation of the magnetic properties of ferritin by AFM imaging with magnetic sample modulation. *Anal. Bioanal. Chem.* **2009,** *394*, 215-223.

152. Li, J. R.; Lewandowski, B. R.; Xu, S.; Garno, J. C., Detecting the magnetic response of iron oxide capped organosilane nanostructures using magnetic sample modulation and atomic force microscopy. *Anal. Chem.* **2009,** *81*, 4792-4802.

153. Smith, R. A., The Colours of Life: An Introduction to the Chemistry of Porphyrins and Related Compounds (Milgrom, Lionel R.). *J. Chem. Educ.* **1998,** *75*, 420.
154. Zhang, A.; Li, C.; Yang, F.; Zhang, J.; Wang, Z.; Wei, Z.; Li, W., An Electron Acceptor with Porphyrin and Perylene Bisimides for Efficient Non-Fullerene Solar Cells. *Angew. Chem.-Int. Edit.* **2017,** *56*, 2694-2698.

155. Zatsikha, Y. V.; Holstrom, C. D.; Chanawanno, K.; Osinski, A. J.; Ziegler, C. J.; Nemykin, V. N., Observation of the Strong Electronic Coupling in Near-Infrared-Absorbing Tetraferrocene aza-Dipyrromethene and aza-BODIPY with Direct Ferrocene−α- and Ferrocene−β-Pyrrole Bonds: Toward Molecular Machinery with Four-Bit Information Storage Capacity. *Inorg. Chem.* **2017,** *56*, 991-1000.

156. Erickson, N. R.; Holstrom, C. D.; Rhoda, H. M.; Rohde, G. T.; Zatsikha, Y. V.; Galloni, P.; Nemykin, V. N., Tuning Electron-Transfer Properties in 5,10,15,20-Tetra(1′-hexanoylferrocenyl)porphyrins as Prospective Systems for Quantum Cellular Automata and Platforms for Four-Bit Information Storage. *Inorg. Chem.* **2017,** *56*, 4716-4727.

157. Jiao, J.; Anariba, F.; Tiznado, H.; Schmidt, I.; Lindsey, J. S.; Zaera, F.; Bocian, D. F., Stepwise formation and characterization of covalently linked multiporphyrin-imide architectures on Si(100). *J. Am. Chem. Soc.* **2006,** *128*, 6965-6974.

158. Liu, C. Y.; Pan, H. L.; Fox, M. A.; Bard, A. J., Reversible charge trapping/detrapping in a photoconductive insulator of liquid crystal zinc porphyrin. *Chem. Mater.* **1997,** *9*, 1422-1429.

159. Murata, K.; Ito, S.; Takahashi, K.; Hoffman, B. M., Photocurrent from photocorrosion of aluminum electrode in porphyrin/Al Schottky-barrier cells. *Appl. Phys. Letts.* **1997,** *71*, 674.

160. Obraztsov, I.; Kutner, W.; D'Souza, F., Evolution of Molecular Design of Porphyrin Chromophores for Photovoltaic Materials of Superior Light-to-Electricity Conversion Efficiency. *Solar RRL* **2017,** *1*, 1600002.

161. Cheng, H.-L.; Huang, Z.-S.; Wang, L.; Meier, H.; Cao, D., Synthesis and photovoltaic performance of the porphyrin based sensitizers with 2H-[1,2,3]triazolo[4,5-c]pyridine and benzotriazole as auxiliary acceptors. *Dyes Pigm.* **2017,** *137*, 143-151.

162. Zampetti, A.; Minotto, A.; Squeo, B. M.; Gregoriou, V. G.; Allard, S.; Scherf, U.; Chochos, C. L.; Cacialli, F., Highly Efficient Solid-State Near-infrared Organic Light-Emitting Diodes incorporating A-D-A Dyes based on α,β-unsubstituted "BODIPY" Moieties. *Sci. Rep.* **2017,** *7*, 1611.

163. Janghouri, M.; Adineh, M., Color optimization of red organic light emitting diodes (OLEDs) through dihydroxyphenyl-substituted zinc porphyrins emitters. *J. Photochem. Photobiol. A* **2017,** *341*, 31-38.

164. Drain, C. M.; Varotto, A.; Radivojevic, I., Self-Organized Porphyrinic Materials. *Chem. Rev.* **2009,** *109*, 1630-1658.

165. Auwärter, W.; Écija, D.; Klappenberger, F.; Barth, J. V., Porphyrins at interfaces. *Nature* **2015,** *7*, 105-120.

166. Auwärter, W.; Weber-Bargioni, A.; A., R.; A., S., Self-assembly and conformation of tetrapyridyl-porphyrin molecules on Ag(111). *J. Chem. Phys.* **2006,** *124*, 194708.

167. Joshi, S.; Bischoff, F.; Koitz, R.; Ecija, K.; Seufert, K.; Seitsonen, A. P.; Hutter, J.; Diller, K.; Urgel, J. I.; Sachdev, H.; Barth, J. V.; Auwarter, W., Control of Molecular Organization and Energy Level Alignment by an Electronically Nanopatterned Boron Nitride Template. *ACS Nano* **2014,** *8*, 430-442.

168. Vijayaraghavan, S.; Ecija, D.; Auwarter, W.; Joshi, S.; Seufert, K.; Seitsonen, A. P.; Tashiro, K.; Barth, J. V., Selective Supramolecular Fullerene-Porphyrin Interactions and Switching in Surface-Confined C-60-Ce(TPP)(2) Dyads. *Nano Lett.* **2012,** *12*, 4077-4083.

169. Zhai, X.; Alexander, D.; Derosa, P.; Garno, J. C., Distance-dependent Measurements of the Conductance of Porphyrin Nanorods Studied with Conductive-Probe Atomic Force Microscopy. *Langmuir* **2017,** *33*, 1132-1138.

170. Zhai, X.; Arachchige, N. M.; Derosa, P.; Garno, J. C., Conductive-probe measurements with nanodots of free-base and metallated porphyrins. *J. Colloid Interface Sci.* **2016,** *486*, 38-45.

171. Siles, P. F.; Bufon, C. C. B.; Grimm, D.; Jalil, A. R.; Mende, C.; Lungwitz, F.; Salvan, G.; Zahn, D. R. T.; Lang, H.; Schmidt, O. G., Morphology and local transport characteristics of metalloporphyrin thin films. *Org. Electron.* **2014,** *15*, 1432-1439.

172. Wang, X. Y.; Wang, G. C.; Lewis, K. M., High rectification ratios of Fe-porphyrin molecules on Au facets. *Mater. Chem. Phys.* **2012,** *136*, 190-195.

173. Hegner, M.; Wagner, P.; Semenza, G., Ultralarge atomically flat template-stripped Au surfaces for scanning probe microscopy. *Surf. Sci.* **1993,** *291*, 39-46.

174. Necas, D.; Klapetek, P., Gwyddion: an open-source software for SPM data analysis. *Cent. Eur. J. Phys.* **2012,** *10*, 181-188.

175. Jennings, G. K.; Munro, J. C.; Yong, T. H.; Laibinis, P. E., Effect of Chain Length on the Protection of Copper by n-Alkanethiols. *Langmuir* **1998,** *14*, 6130-6139.

176. Haag, R.; Rampi, M. A.; Holmlin, R. E.; Whitesides, G. M., Electrical Breakdown of Aliphatic and Aromatic Self-Assembled Monolayers Used as Nanometer-Thick Organic Dielectrics. *J. Am. Chem. Soc.* **1999,** *121*, 7895-7906.

177. Laibinis, P. E.; Whitesides, G. M., Self-assembled monolayers of n-alkanethiolates on copper are barrier films that protect the metal against oxidation by air. *J. Am. Chem. Soc.* **1992,** *114*, 9022-9028.

178. Chinwangso, P.; Jamison, A. C.; Lee, T. R., Multidentate Adsorbates for Self-Assembled Monolayer Films. *Acc. Chem. Res.* **2011,** *44*, 511-519.

179. Duwez, A. S., Exploiting electron spectroscopies to probe the structure and organization of self-assembled monolayers: a review. *J. Electron. Spectrosc.* **2004,** *134*, 97-138.

180. Bain, C. D.; Troughton, E. B.; Tao, Y. T.; Evall, J.; Whitesides, G. M.; Nuzzo, R. G., Formation of Monolayer Films by the Spontaneous Assembly of Organic Thiols from Solution onto Gold. *J. Am. Chem. Soc.* **1989,** *111*, 321-335.

181. Biener, M. M.; Biener, J.; Friend, C. M., Revisiting the S-Au(111) interaction: Static or dynamic? *Langmuir* **2005,** *21*, 1668-1671.

182. Zhang, Y.; Lovell, J. F., Recent applications ofphthalocyanines andnaphthalocyanines for imagingand therapy. *WIREs Nanomed. Nanobiotechnol.* **2017,** *9*, 1-15.

183. de la Torre, G.; Claessens, C. G.; Torres, T., Phthalocyanines: old dyes, new materials. Putting color in nanotechnology. *Chem. Commun.* **2007,** *20*, 2000-2015.

184. Bai, M.; Lo, P.-C.; Ye, J.; Wu, C.; Fong, W.-P.; Ng, D. K., Facile synthesis of pegylated zinc (II) phthalocyanines via transesterification and their in vitro photodynamic activities. *Org. Biomol. Chem.* **2011,** *9*, 7028-7032.

185. Hoppe, H.; Sariciftci, N. S., Organic solar cells: An overview. *J. Mater. Res* **2004,** *19*, 1924-1945.

186. Loutfy, R.; Sharp, J.; Hsiao, C.; Ho, R., Phthalocyanine organic solar cells: Indium/x-metal free phthalocyanine Schottky barriers. *J. Appl. Phys.* **1981,** *52*, 5218-5230.

187. Stojiljkovic, I.; Evavold, B. D.; Kumar, V., Antimicrobial properties of porphyrins. *Expert Opin. Invest. Drugs* **2001,** *10*, 309-320.

188. Yu, K. G.; Li, D. H.; Zhou, C. H.; Diao, J. L., Study on the synthesis and antimicrobial activity of novel cationic porphyrins. *Chin. Chem. Lett.* **2009,** *20*, 411-414.

189. Banfi, S.; Caruso, E.; Buccafurni, L.; Battini, V.; Zazzaron, S.; Barbieri, P.; Orlandi, V., Antibacterial activity of tetraaryl-porphyrin photosensitizers: an in vitro study on Gram negative and Gram positive bacteria. *J. Photochem. Photobiol. B* **2006,** *85*, 28-38.

190. Malik, Z.; Hanania, J.; Nitzan, Y., New trends in photobiology bactericidal effects of photoactivated porphyrins—An alternative approach to antimicrobial drugs. *J. Photochem. Photobiol. B* **1990,** *5*, 281-293.

191. Dhananjoy, M.; Smritilekha, B., Porphyrins and phthalocyanines: promising molecules for light-triggered antibacterial nanoparticles. *Adv. Nat. Sci: Nanosci. Nanotechnol.* **2014,** *5* (3), 033002.

192. Perevalov, V. P.; Vinokurov, E. G.; Zuev, K. V.; Vasilenko, E. A.; Tsivadze, A. Y., Modification and Application of Metal Phthalocyanines in Heterogeneous Systems. *Prot. Met. Phys. Chem. Surf.* **2017,** *53*, 199-214.

193. Cook, M. J., Phthalocyanine thin films. *Pure and Appl. Chem.* **1999,** *71* (11), 2145-2151.

194. Kriegisch, V.; Lambert, C., Self-assembled monolayers of chromophores on gold surfaces. In *Supermolecular Dye Chemistry*, Springer: 2005; pp 257-313.

195. Chernonosov, A. A.; Ermilov, E. A.; Röder, B.; Solovyova, L. I.; Fedorova, O. S., Effect of Some Substituents Increasing the Solubility of Zn(II) and Al(III) Phthalocyanines on Their Photophysical Properties. *Bioinorg. Chem. Appl.* **2014,** *2014*, 1-8.

196. Ozoemena, K. I.; Nyokong, T., Electrochemical behaviour of thiol-derivatised zinc (II) phthalocyanine complexes and their self-immobilised films at gold electrodes. *Microchemical journal* **2003,** *75* (3), 241-247.

197. Ozoemena, K.; Westbroek, P.; Nyokong, T., Long-term stability of a gold electrode modified with a self-assembled monolayer of octabutylthiophthalocyaninato-cobalt (II) towards l-cysteine detection. *Electrochem. Commun.* **2001,** *3*, 529-534.

198. Li, Z.; Lieberman, M.; Hill, W., XPS and SERS Study of Silicon Phthalocyanine Monolayers: Umbrella vs Octopus Design Strategies for Formation of Oriented SAMs. *Langmuir* **2001,** *17* (16), 4887-4894.

199. Chen, X.; Thomas, J.; Gangopadhyay, P.; Norwood, R. A.; Peyghambarian, N.; McGrath, D. V., Modification of Symmetrically Substituted Phthalocyanines Using Click Chemistry: Phthalocyanine Nanostructures by Nanoimprint Lithography. *J. Am. Chem. Soc.* **2009,** *131*, 13840-13843.

200. Sariola, E.; Kotiaho, A.; Tkachenko, N. V.; Lemmetyinen, H.; Efimov, A., Mono-, bis- and tetrahydroxy phthalocyanines as building blocks for monomolecular layer assemblies. *J. Porphyrins Phthalocyanines* **2010,** *14* (05), 397-411.

201. Cid, J. J.; García-Iglesias, M.; Yum, J. H.; Forneli, A.; Albero, J.; Martínez-Ferrero, E.; Vazquez, P.; Grätzel, M.; Nazeeruddin, M. K.; Palomares, E., Structure–Function Relationships in Unsymmetrical Zinc Phthalocyanines for Dye-Sensitized Solar Cells. *Chem. Eur. J.* **2009,** *15*, 5130-5137.

202. Kment, S.; Kluson, P.; Drobek, M.; Kuzel, R.; Gregora, I.; Kohout, M.; Hubicka, Z., Preparation of thin phthalocyanine layers and their structural and absorption properties. *Thin Solid Films* **2009,** *517*, 5274-5279.

203. Schünemann, C.; Elschner, C.; Levin, A. A.; Levichkova, M.; Leo, K.; Riede, M., Zinc phthalocyanine — Influence of substrate temperature, film thickness, and kind of substrate on the morphology. *Thin Solid Films* **2011,** *519*, 3939-3945.

204. Chowdhury, A.; Biswas, B.; Majumder, M.; Sanyal, M. K.; Mallik, B., Studies on phase transformation and molecular orientation in nanostructured zinc phthalocyanine thin films annealed at different temperatures. *Thin Solid Films* **2012,** *520*, 6695-6704.

205. Vergnat, C.; Uttiya, S.; Pratontep, S.; Kerdcharoen, T.; Legrand, J.-F.; Brinkmann, M., Oriented growth of zinc(II) phthalocyanines on polycarbonate alignment substrates: Effect of substrate temperature on in-plane orientation. *Synth. Met.* **2011,** *161*, 251-258.

206. Senthilarasu, X.; Hahn, Y. B.; Lee, S.-H., Nano structure formation in vacuum evaporated zinc phthalocyanine (ZnPc) thin films. *J. Mater. Electron.* **2008,** *19*, 482-486.

207. Gaffo, L.; Cordeiro, M. R.; Freitas, A. R.; Moreira, W. C.; Girotto, E. M.; Zucolotto, V., The effects of temperature on the molecular orientation of zinc phthalocyanine films. *J. Mater. Sci.* **2010,** *45*, 1366-1370.

208. Wen, K.; Maoz, R.; Cohen, H.; Sagiv, J.; Gibaud, A.; Desert, A.; Ocko, B. M., Postassembly chemical modification of a highly ordered organosilane multilayer: New insights into the structure, bonding, and dynamics of self-assembling silane monolayers. *ACS Nano* **2008,** *2*, 579-599.

209. Lusker, K. L.; Yu, J.-J.; Garno, J. C., Particle lithography with vapor deposition of organosilanes: A molecular toolkit for studying confined surface reactions in nanoscale liquid volumes. *Thin Solid Films* **2011,** *519*, 5223-5229.

210. Bae, C.; Kim, H.; Shin, H., Contact area lithography and pattern transfer of self-assembled organic monolayers on SiO 2/Si substrates. *Chem. Commun* **2011,** *47*, 5145-5147.

211. Bae, C.; Shin, H.; Moon, J.; Sung, M. M., Contact area lithography (CAL): A new approach to direct formation of nanometric chemical patterns. *Chem. Mat.* **2006,** *18*, 1085-1088.

212. Geissler, M.; McLellan, J. M.; Chen, J.; Xia, Y., Side-by-Side Patterning of Multiple Alkanethiolate Monolayers on Gold by Edge-Spreading Lithography. *Angew. Chem.-Int. Edit.* **2005,** *44*, 3596-3600.

213. Li, J.-R.; Garno, J. C., Elucidating the role of surface hydrolysis in preparing organosilane nanostructures via particle lithography. *Nano Lett.* **2008,** *8*, 1916-1922.

214. McLellan, J. M.; Geissler, M.; Xia, Y., Edge spreading lithography and its application to the fabrication of mesoscopic gold and silver rings. *J. Am. Chem. Soc.* **2004,** *126*, 10830-10831.

215. Jiang, P.; McFarland, M. J., Large-scale fabrication of wafer-size colloidal crystals, macroporous polymers and nanocomposites by spin-coating. *J. Am. Chem. Soc.* **2004,** *126*, 13778-13786.

216. Tessier, P. M.; Velev, O. D.; Kalambur, A. T.; Lenhoff, A. M.; Rabolt, J. F.; Kaler, E. W., Structured metallic films for optical and spectroscopic applications via colloidal crystal templating. *Adv. Mater.* **2001,** *13*, 396-400.

217. Lin, B. C.; Ku, C. S.; Lee, H. Y.; Wu, A. T., Epitaxial growth of ZnO nanorod arrays via a self-assembled microspheres lithography. *Appl. Surf Sci.* **2017,** *31*, 212-217.

218. Chen, J.; Liao, W.-S.; Chen, X.; Yang, T.; Wark, S. E.; Son, D. H.; Batteas, J. D.; Cremer, P. S., Evaporation-induced assembly of quantum dots into nanorings. *ACS Nano* **2008,** *3*, 173-180.

219. Hulteen, J. C.; Treichel, D. A.; Smith, M. T.; Duval, M. L.; Jensen, T. R.; Van Duyne, R. P., Nanosphere lithography: size-tunable silver nanoparticle and surface cluster arrays. *J. Phys. Chem. B* **1999,** *103*, 3854-3863.

220. Lewandowski, B. R.; Kelley, A. T.; Singleton, R.; Li, J.-R.; Lowry, M.; Warner, I. M.; Garno, J. C., Nanostructures of cysteine-coated CdS nanoparticles produced with "two-particle" lithography. *J. Phys. Chem. C* **2009,** *113*, 5933-5940.

221. Singh, G.; Griesser, H. J.; Bremmell, K.; Kingshott, P., Highly Ordered Nanometer-Scale Chemical and Protein Patterns by Binary Colloidal Crystal Lithography Combined with Plasma Polymerization. *Adv. Funct. Mater.* **2011,** *21*, 540-546.

222. Singh, G.; Gohri, V.; Pillai, S.; Arpanaei, A.; Foss, M.; Kingshott, P., Large-area protein patterns generated by ordered binary colloidal assemblies as templates. *ACS Nano* **2011,** *5*, 3542-3551.

223. Sipos, A.; Szalai, A.; Csete, M., Integrated lithography to prepare periodic arrays of nano-objects. *Appl. Surf. Sci.* **2013,** *278*, 330-335.

224. Ongarora, B. G.; Zhou, Z.; Okoth, E. A.; Kolesnichenko, I.; Smith, K. M.; Vicente, M. G. H., Synthesis, spectroscopic, and cellular properties of a-pegylated cis-A2B2- and A3B-types ZnPcs. *J. Porphyrins Phthalocyanines* **2014,** *18*, 1021-1033.

225. Okoth, E. Ph.D. dissertation. Louisiana State University, Baton Rouge, Louisiana, 2017.

226. Li, H.; Jensen, T. J.; Fronczek, F. R.; Vicente, M. G. H., Syntheses and Properties of a Series of Cationic Water-Soluble Phthalocyanines. *J.Med.Chem.* **2005,** *51*, 502-511.

227. Brownfield, A. L.; Causey, C. P.; Mullen, T. J., Effects of surface water on organosilane nanostructure fabrication using particle lithography. *Thin Solid Films* **2015,** *594*, 184-191.

228. Bierbaum, K.; Grunze, M.; Baski, A.; Chi, L.; Schrepp, W.; Fuchs, H., Growth of self-assembled n-alkyltrichlorosilane films on Si (100) investigated by atomic force microscopy. *Langmuir* **1995,** *11*, 2143-2150.

229. Englade-Franklin, L. E.; Saner, C. K.; Garno, J. C., Spatially selective surface platforms for binding fibrinogen prepared by particle lithography with organsilane. *Interface Focus* **2013,** *3*, 1-9.

230. Lusker, K. L.; Li, J. R.; Garno, J. C., Nanostructures of Functionalized Gold Nanoparticles Prepared by Particle Lithography with Organosilanes. *Langmuir* **2011,** *27*, 13269-13275.

231. Rapulenyane, N.; Antunes, E.; Nyokong, T., A study of the photophysicochemical and antimicrobial properties of two zinc phthalocyanine–silver nanoparticle conjugates. *New J. Chem.* **2013,** *37*, 1216-1226.

232. Nonnenmacher, M.; O'Boyle, M. P.; Wickramasinghe, H. K., Kelvin probe force microscopy. *App. Phys. Letts.* **1991,** *58*, 2921-2923.

APPENDIX A: SUPPORTING INFORMATION FOR CHAPTER 4

Control Studies of ZnPc 1 in the Absence of APTES

To ensure that a linker is needed to successfully control deposition and the aggregation of the Zn-Pc onto glass surfaces, a control experiment was designed without backfilling the nanoholes with APTES. Nanoholes within a film of OTS were prepared and immersed in the diluted ZnPc 1 solution for 3 h. It is evident in Figure A.1 that without a linker, ZnPc 1 formed aggregates on the surface and did not fill in the nanoholes with exposed substrate. There is no affinity for binding between the functional group on the ZnPc 1 or on surrounding areas of the methyl-terminated OTS resist.

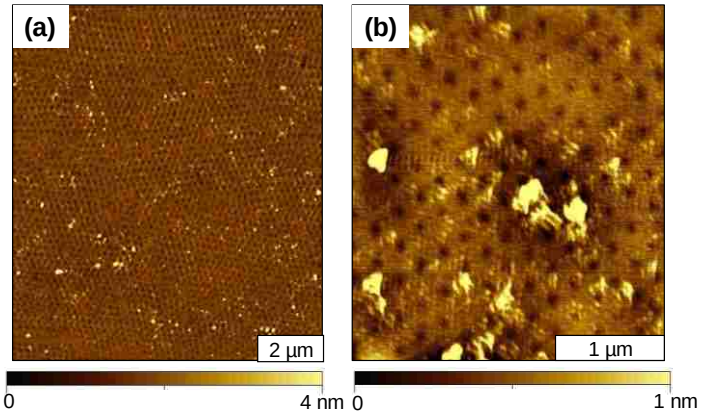

Figure A.1 Control sample of ZnPc **1** in the absence of APTES. (A) Tapping-mode topography image (10 × 10 μm^2); (B) magnified view (3 × 3 μm^2).

Control Studies of ZnPc 2 in the Absence of APTES

The procedure was repeated for ZnPc **2**, shown with example results in Figure A.2. Within the broader area of Figure A.2A there are a few aggregates that were deposition, and adsorption did not occur within the nanoholes of exposed glass substrate. A zoom-in view reveals further that the deposition of ZnPc 1 is random, and clusters are scatter throughout the surface on the matrix and areas of nanoholes in a random arrangement.

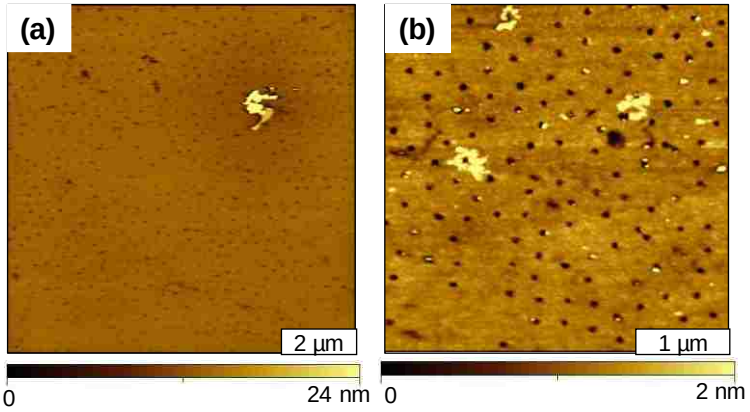

Figure A.2 Control sample of ZnPc **2** prepared without the APTES linker. (A) Topography frame for a broad areas of the sample (10 × 10 µm^2); topography image (B) magnified view (4 × 4 µm^2).

Histogram Analysis of the Dimensions of Nanostructures Prepared with Particle Lithography

Histograms were made to evaluate the heights of the nanostructures after each key step of sample preparation with particle lithography. The first experiment is shown in Figure A.3 reveals the depth of the nanoholes ranged from 1.0 to 2.2 nm, with an average value of 1.9 ± 0.3 nm.

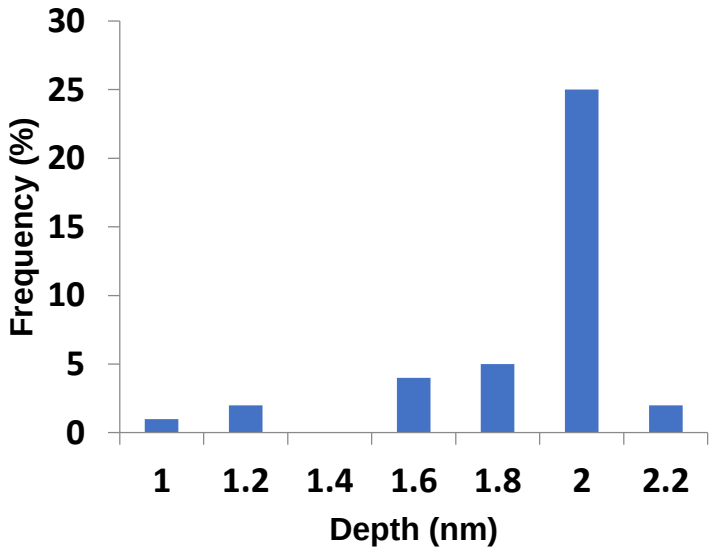

Figure A.3 Histogram of the depth measurements of nanoholes within OTMS (*n*=50).

The size distribution of the thickness of nanorings within a matrix film of PEG-silane is presented in the histogram of Figure A.4. The mean value measured 3.0 ± 0.3 nm, with heights ranging from 3 to 4.6 nm referencing the inside areas of the nanopatterns as a baseline for measurements.

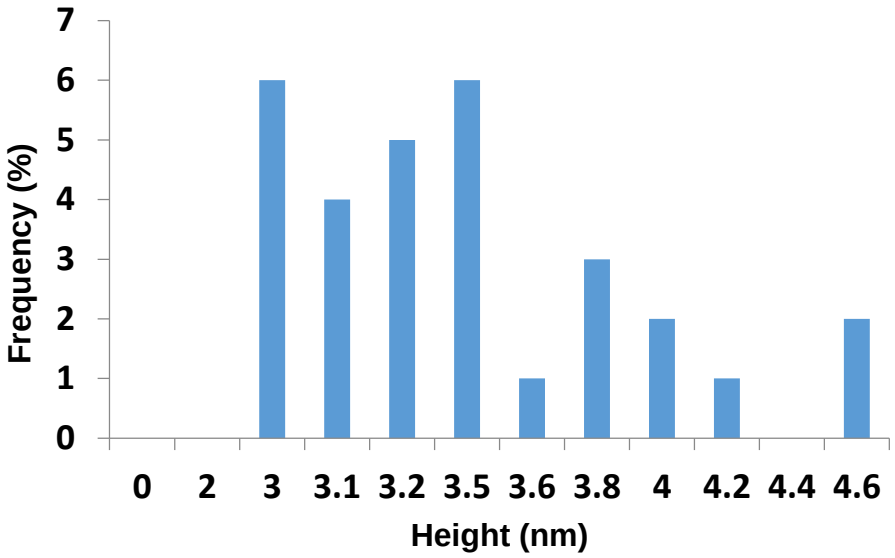

Figure A.4 Histogram of the height measurements of PEG-silane nanorings (*n*=50).

After the sample of nanoholes within OTMS was prepared, the samples was immersed in a solution of APTES for 3 h at RT. The nanopatterns formed selectively within the areas of uncovered substrate inside the nanoholes to form nanodots. The size distribution of cursor height measurements is shown in Figure A.5, revealing heights ranging from 1 to 5 nm, and an average value of 2.0 ± 0.8 nm.

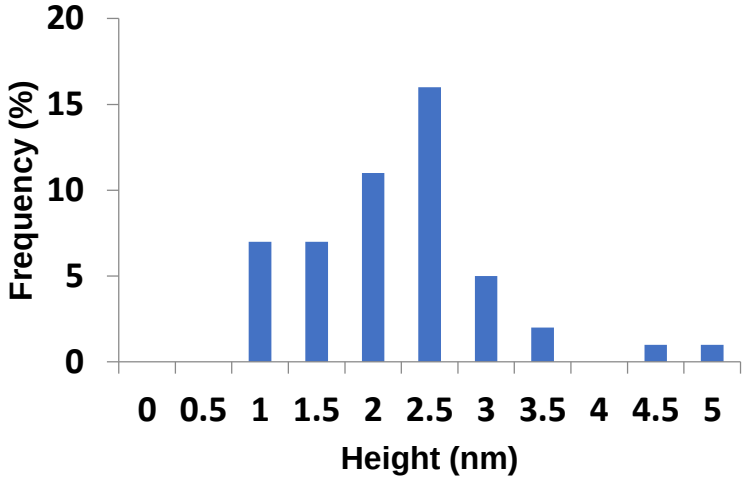

Figure A.5 Size distribution showing the growth of APTES within nanoholes surrounded by a matrix of OTMS. The heights indicate the height of the nanostructures above the matrix (*n*=50).

The sample with nanoholes surrounded by PEG-silane were immersed in APTES solution for 3 h at RT. The increase in height above the PEG-silane film was measured for multiple nanopatterns using AFM cursor profiles. The height distribution is shown in Figure A.6, indicating a range of values from 2.5 to 4 nm, and an average thickness of 3.2 ± 0.4 nm.

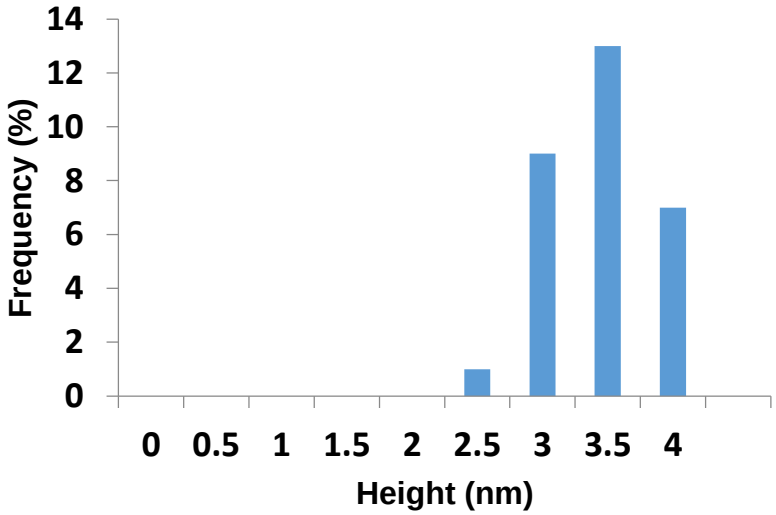

Figure A.6 Growth of APTES nanostructures within a PEG-silane matrix (*n*=50).

The sample with APTES nanodots on the OTMS matrix were immersed in a dilute solution of ZnPc 1. The increase in height was measured for multiple nanopatterns using AFM cursor profiles. The height distribution is shown in Figure A.7, indicating a range of values from 2.2 to 5.2 nm, and an average thickness of 3.3 ± 0.7 nm.

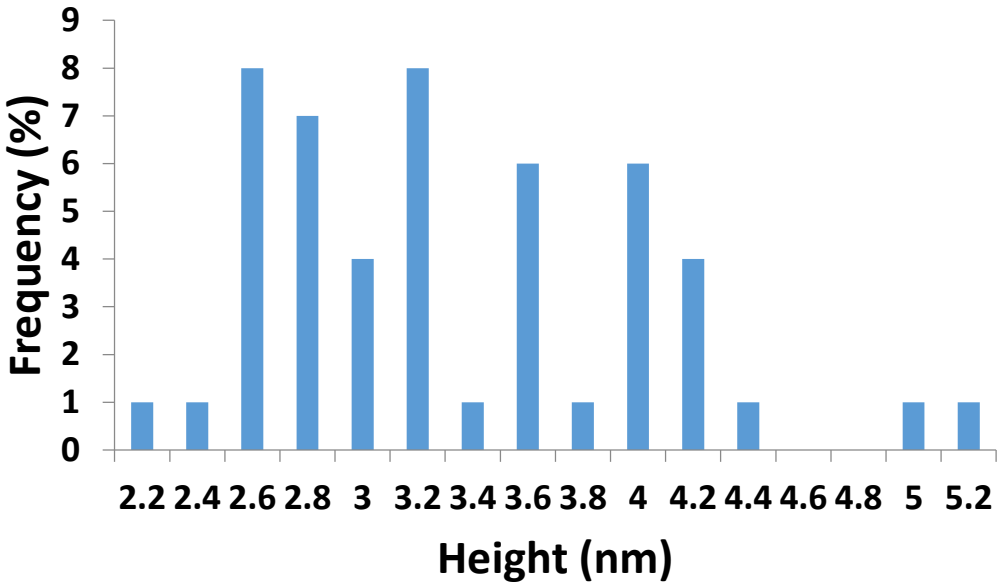

Figure A.7 Histogram of the growth of ZnPc **1** on APTES nanopatterns surrounded by a matrix film of OTMS (*n*=50).

The sample with APTES nanodots on the PEG-silane matrix were also immersed in a dilute solution of ZnPc 1. The increase in height was measured for multiple nanopatterns using AFM cursor profiles. The height distribution is shown in Figure A.8, indicating a range of values from 3.5 to 5.0 nm, and an average thickness of 4.3 ± 0.5 nm.

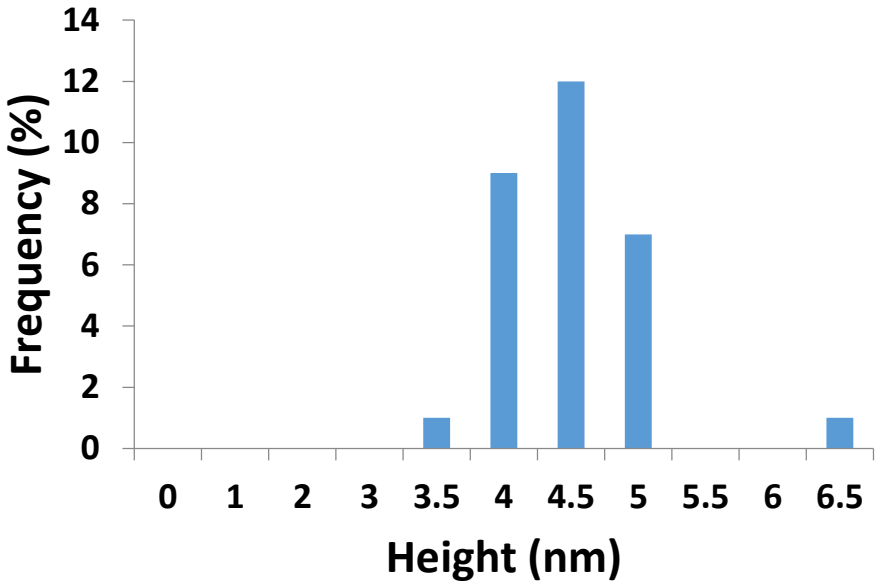

Figure A.8 Histogram showing the height of nanostructures after growth of ZnPc 1 on APTES/PEG-silane matrix (*n*=30).

The sample with APTES nanodots on the OTMS matrix were also immersed in a dilute solution of ZnPc 2. The increase in height was measured for multiple nanopatterns using AFM cursor profiles. The height distribution is shown in Figure A.9, indicating a range of values from 5 to 17.5 nm, and an average thickness of 6.3 ± 4 nm.

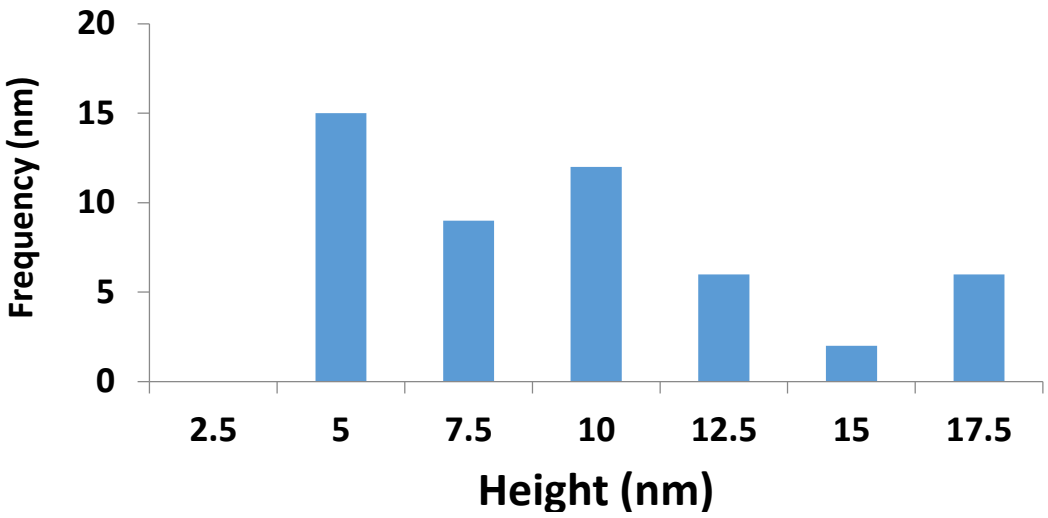

Figure A.9 Histogram showing the heights of nanostructures after growth of ZnPc 2 on APTES/OTMS matrix (*n*=50)

APPENDIX B: LABORATORY PROCEDURE FOR PARTICLE LITHOGRAPHY COMBINED WITH PDMS STAMPS

1. Blank CD-ROMS were immersed in a dilute solution of nitric acid and stripped of the polymer and aluminum coating. After rinsing with deionized water and drying with nitrogen gas, the bare CD-ROM was cut into 2×2 cm^2 squares and placed into a petri dish.
2. A portion of 50 g of prepolymer and 5 g of curing agent of PDMS was added to a plastic cup with vigorous mixing before adding it to the glass petri dish containing the CD-ROM pieces. The mixture remained undisturbed at room temperature for 2 h to enable the removal of air bubbles. The petri dish was placed in the oven for 1 h at 70ºC. After the sample cooled to room temperature, the PDMS stamp was cut into 2×2 cm^2 pieces and rinsed with ethanol. The pieces were stored in ethanol for future use.
3. A solutions of Fe(III) (0.1 M was made by dissolving 0.675 g of $FeCl_3 \cdot 6H_2O$ in a 25 mL volumetric flask containing degassed water. A 0.1 M Fe(II) solution was made by dissolving 0.497 g of $FeCl_2 \cdot 4H_2O$ in a 25 mL volumetric flask containing degassed water. Ammonium hydroxide was diluted by adding 22.3 mL of NH_4OH into a 25 mL volumetric flask of degassed water (14.8 M).
4. Iron oxide nanoparticles were synthesized in a highly basic solution of Fe(II) and Fe(III) salt ions prepared with a 1:2 ratio. In a double neck round bottom flask, 10 mL of the 0.1 M Fe(II) was added to 20 mL of 0.1 M Fe(III) and stirred at 60°C under a nitrogen environment. The 14.8 M ammonium solution was added drop wise to the solution until pH 12 was reached. The solution was stirred for an hour to produce black nanoparticles. Aliquots of the nanoparticle solution was centrifuged in degassed water to remove any contaminants before use.

5. Glass and Si(111) substrates were cleaned using piranha solution. An aliquot of the Fe_3O_4 nanoparticles (20 µL) was diluted in a 10 mL volumetric flask to prevent aggregation. A 40 µL solution was diluted into a 10 mL volumetric flask. The PDMS stamps were placed onto the glass and silica substrates and secured with clamps. The Fe_3O_4 nanoparticles (30 µL) were injected into the corners of the substrates to spread across the substrate through capillary forces. The samples were dried in ambient conditions for 24 h.

Results

Magnetic sample modulation-AFM imaging is selective for detecting nanomaterials that vibrate in response to an applied current. Contact mode AFM images without the influence of a magnetic field were acquired to obtain topography frames of the Fe_3O_4 nanoparticles patterned by the PDMS stamp (Figures 3.5A and 3.5D). The magnetic field was applied to produce a signal from the vibrations of the nanoparticles. For Figures 3.5A-3.5C a frequency of 211.2 kHz was used. The MSM amplitude (Figure 3.5B) and phase (Figure 3.5C) images show signals from the vibrations of the Fe_3O_4 nanoparticles. For Figures 3.5D-3.5F a frequency of 217.4 kHz was used to produce the signal that is present within the amplitude and phase images.

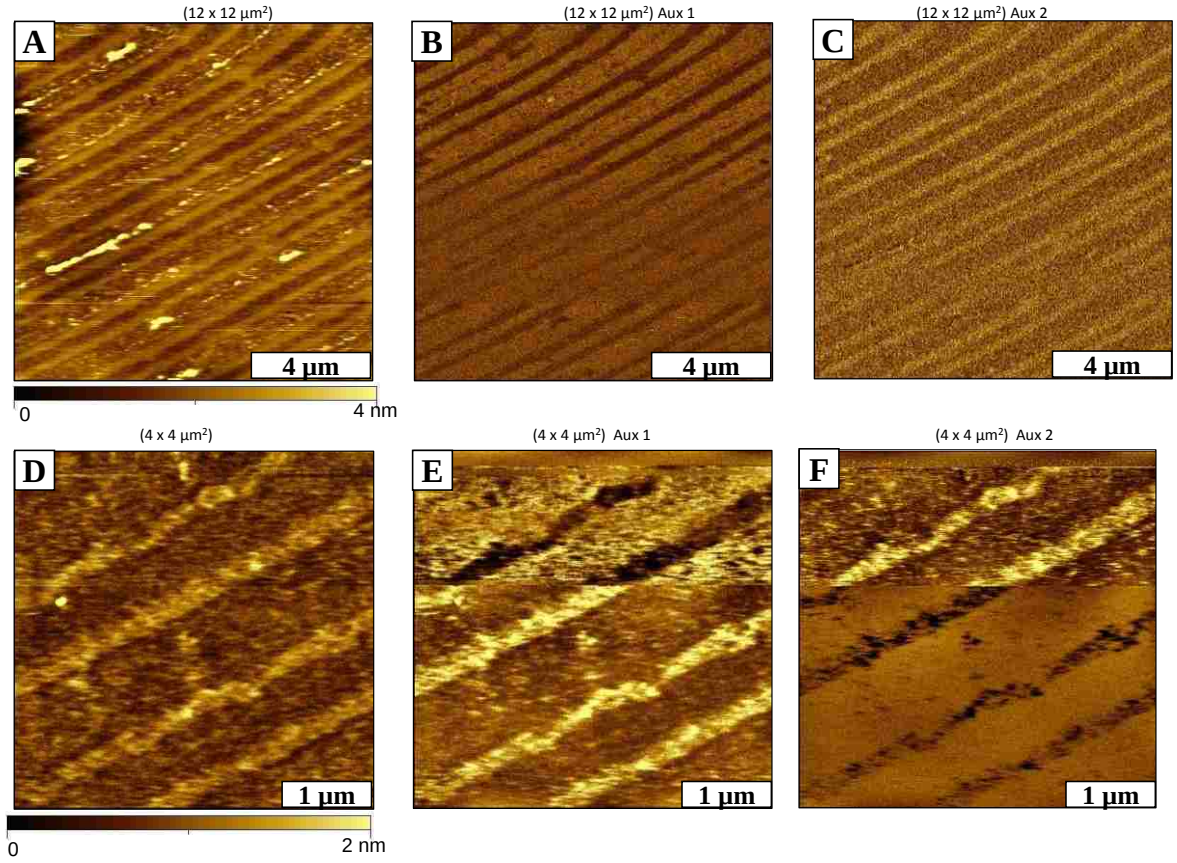

Figure B.1 Vibrational response of Fe_3O4 nanoparticles mapped with MSM-AFM. (A) Topography (12×12 μm^2); (B) MSM-amplitude image; (C) Corresponding MSM-phase frame; (D) Magnified view (4×4 μm^2) (E) MSM-amplitude (4×4 μm^2) (F) Corresponding phase channel.

VITA

Ashley Marie Taylor was born in Manhattan, New York, to her parents Natalie Diaz-Taylor and Maxwell Anthony Taylor. She has one sibling, Maxwell Cory Taylor. She was raised in Queens, NY and Piscataway, NJ where she graduated from Piscataway Township High School in 2008. She moved to Winston-Salem, NC to attend Winston-Salem State University and graduated with a Bachelor's degree in chemistry in 2012.

In fall of 2012, Ashley joined the Department of Chemistry as a Doctoral student at Louisiana State University and A&M College as a fellow of the NSF-Louis Stokes Alliance Bridge to Doctoral Fellowship. She joined Professor Donghui Zhang's group in the macromolecular division for two years before joining Professor Jayne Garno's research group in analytical. In between the transition, Ashley defended and completed her Master's degree in chemistry at LSU in 2015. Her research included nanoscale measurements of metallic nanomaterials using atomic force microscopy.

As a graduate student, Ashley has traveled to conferences held by the National Organization for the Professional Advancement of Black Chemists and Chemical Engineers (NOBCChE) and the American Chemical Society (ACS) a presenter. She has also won travel awards for all of her conference appearances and was the ACS Student Exchange Award recipient. Her professional affiliations include ACS, NOBCChE, Iota Sigma Pi (ISP), the Black Graduate and Professional Student Association (BGPSA) and Alpha Kappa Alpha Sorority, Incorporated. Ashley will be awarded the degree of Doctor of Philosophy in chemistry from LSU this coming school year.